



저작자표시-비영리-변경금지 2.0 대한민국

이용자는 아래의 조건을 따르는 경우에 한하여 자유롭게

- 이 저작물을 복제, 배포, 전송, 전시, 공연 및 방송할 수 있습니다.

다음과 같은 조건을 따라야 합니다:



저작자표시. 귀하는 원저작자를 표시하여야 합니다.



비영리. 귀하는 이 저작물을 영리 목적으로 이용할 수 없습니다.



변경금지. 귀하는 이 저작물을 개작, 변형 또는 가공할 수 없습니다.

- 귀하는, 이 저작물의 재이용이나 배포의 경우, 이 저작물에 적용된 이용허락조건을 명확하게 나타내어야 합니다.
- 저작권자로부터 별도의 허가를 받으면 이러한 조건들은 적용되지 않습니다.

저작권법에 따른 이용자의 권리는 위의 내용에 의하여 영향을 받지 않습니다.

이것은 [이용허락규약\(Legal Code\)](#)을 이해하기 쉽게 요약한 것입니다.

[Disclaimer](#)

공학석사 학위 논문

RF 이온 추력기 설계

**DESIGN OF AN RF ION THRUSTER**

울산대학교 대학원

기계공학과 항공우주공학전공

PHAM TRAN DANG QUANG

# **DESIGN OF AN RF ION THRUSTER**

A thesis submitted in partial fulfillment of the requirement for the Degree of  
Master of Science to the Department of Aerospace Engineering, University of Ulsan, Korea

By

**PHAM TRAN DANG QUANG**

**NOVEMBER 2018**

RF 이온 추력기 설계

**DESIGN OF AN RF ION THRUSTER**

지도교수 신지철

이논문을 공학석사 학위 논문으로 제출함

2018 년 11 월

울산대학교 대학원

기계공학과 항공우주공학전공

# **DESIGN OF AN RF ION THRUSTER**

**This certifies that the dissertation of  
PHAM TRAN DANG QUANG is approved by**

---

**Committee Chairman: Prof. Kim BoHung**

---

**Committee Member: Prof. Achiri Celestine Tange**

---

**Committee Member: Prof. Shin Jichul**

---

**Department of Aerospace Engineering**

**University of Ulsan, Korea**

**November 2018**

# PHAM TRAN DANG QUANG 의

## 공학석사학위논문을인준함

---

심사위원장	김보흥	(인)
-------	-----	-----

---

심사위원	아치리 탄제	(인)
------	--------	-----

---

심사위원	신지철	(인)
------	-----	-----

---

울산대학교대학원

기계공학과 항공우주공학전공

2018년 5월

## **Acknowledgements**

I would like to express my appreciation to my advisor, Prof. SHIN, JICHUL, for his guidance, advice and support during my study in University of Ulsan. All of my works in this dissertation cannot be accomplished without his support.

I would also like to thank to Prof. Kim, BoHung and Prof. Achiri Celestine Tange for serving on my graduate committee and providing suggestions and comments throughout this thesis.

I would like to thank my friends, my colleagues, all members of AARL Lab., for their help, guidance, and co-working during the time I study in University of Ulsan. I also would like to thank to Prof. Dan M.Goebel, Prof. Dr. Peter J. Klar and Dr. Kristof Holste for their help during the time I study on RF ion thruster.

Above all, I would like to express my love to my parents, my wife, my sister. Thank you for everything!

Ulsan, Nov 2018

**Pham Tran Dang Quang**

# Contents

Acknowledgements .....	i
Contents .....	ii
List of figures .....	v
List of tables.....	viii
Abbreviations .....	ix
Abstract.....	x
Chapter 1. State of the art .....	1
1.1 Introduction to space propulsion.....	1
1.2 Introduction to electric thruster .....	4
1.3 Scope of dissertation .....	5
1.4 Limitation of dissertation .....	6
1.5 Dissertation outline .....	7
Chapter 2. Theory and Background .....	8
2.1 Fundamental of thruster .....	8
2.2 Plasma propulsion.....	9
2.2.1 Concept of Radio-frequency.....	9
2.2.2 Description of Radio-frequency ion thruster .....	11
2.2.3 Advantages .....	13
2.2.4 Inconvenience .....	13
2.3 Summary .....	14
Chapter 3. 0-D Analytical model for discharge chamber .....	15
3.1 Introduction .....	15
3.2 Description of the model .....	17
3.3 Plasma sheaths .....	19
3.4 Grid consideration.....	21

3.5 Ion optics model.....	24
3.6 Neutral gas model .....	26
3.7 Plasma discharge model.....	29
3.7.1 Particle and power balance .....	30
3.7.2 Electromagnetic model.....	35
3.7.3 Energy consumption by plasma discharge chamber .....	40
3.8 Results and comparison with experiments .....	41
3.9 Chapter summary .....	49
Chapter 4. iU-50 Ion Thruster Design.....	50
4.1 Introduction .....	50
4.2 Radio frequency technology thruster design .....	51
4.3 iU-50 Thruster design and components .....	53
4.3.1 Main ionization chamber .....	54
4.3.2 Gas inlet.....	56
4.3.3 RF coil .....	57
4.3.4 Grids system .....	57
4.3.5 Grid mounting ring.....	60
4.3.6 iU-50 Ion Thruster case.....	61
4.3.7 NU-50 Neutralizer.....	62
4.4 Performance prediction of iU-50 ion thruster.....	64
4.4.1 Power absorbed.....	64
4.5 Preliminary iU-50 thruster operation .....	67
4.6 Chapter summary.....	69
Chapter 5. RF matching network and coil configuration .....	70
5.1 Introduction .....	70
5.2 Inductively circuit model (ICP).....	71
5.3 Impedance matching .....	75

5.4 Extended-field electromagnetic model .....	77
5.5 Thermal plasma model .....	82
5.6 Chapter summary .....	86
Chapter 6. Measurement System Development .....	87
6.1 Micro-Newton resolution thrust stand development.....	87
6.1.1 Torsion balance dynamics .....	87
6.1.2 Calibration .....	90
6.2 Development of AARL electrostatic comb system for AARL thrust stand.....	91
6.2.1 Fundamental of the electrostatic comb.....	91
6.2.2 Experiment setup.....	95
6.3 Development of AARL electromagnetic system for AARL thrust stand .....	98
6.4 A power supply of the retarding potential analyzer (RPA).....	101
6.5 Chapter summary .....	107
Chapter 7. Conclusion and Future Work .....	108
7.1 Conclusions .....	108
7.2 Future works.....	109

## List of figures

<b>Fig. 1.1</b> Description of Telstar 401 .....	2
<b>Fig. 1.2</b> Number of EP-based GEO satellites launched from 1993 to 2016.....	3
<b>Fig. 1.3</b> Common electric propulsion thruster .....	4
<b>Fig. 1.4</b> Outline of chapters.....	7
<b>Fig. 2.1</b> Electromagnetic properties in the different frequency ranges .....	9
<b>Fig. 2.2</b> Electromagnetic properties in the different frequency ranges .....	10
<b>Fig. 2.3</b> Schematic of an RIT ion thruster with a conical shape modeled.....	12
<b>Fig. 3.1</b> Schematic of an RIT 10 (10 cm diameter) ion thruster .....	16
<b>Fig. 3.2</b> Flow chart of the analytical discharge model .....	17
<b>Fig. 3.3</b> Child-Langmuir sheath length versus various propellant .....	20
<b>Fig. 3.4</b> Effect of screen grid on charged particles in a plasma .....	21
<b>Fig. 3.5</b> Plasma sheath layout and potential on-axis .....	22
<b>Fig. 3.6</b> Comparison of Impingement-Limited Current Levels .....	23
<b>Fig. 3.7</b> 2-D axisymmetric well-focused ion beams and parallel trajectory .....	24
<b>Fig. 3.8</b> Representative ion trajectories from a I-gun calculation .....	25
<b>Fig. 3.9</b> 2-D axisymmetric neutral gas density distribution normalized .....	27
<b>Fig. 3.10</b> Pressure effect on plasma density .....	28
<b>Fig. 3.11</b> ESA-XX general view .....	30
<b>Fig. 3.12</b> Basic thruster performance at different ion current levels.....	30
<b>Fig. 3.13</b> Expression for collisional skin depth.....	36
<b>Fig. 3.14</b> Effect of the discharge chamber configuration on the magnetic field (FEMM).....	37
<b>Fig. 3.15</b> Discharge loss versus mass utilization efficiency.....	40
<b>Fig. 3.16</b> Comparison of the calculations obtained from the models.....	42
<b>Fig. 3.17</b> The ion production cost channels map of the ESA-XX RF ion thruster .....	42
<b>Fig. 3.18</b> Miniaturized RIT-4 ion engine from Giessen University .....	44
<b>Fig. 3.19</b> Experimentally and analytical obtained discharge power. ....	45

<b>Fig. 3.20</b> Comparisons of the our simulation and experimental data.....	46
<b>Fig. 3.21</b> Comparisons of the our simulation and experimental data.....	47
<b>Fig. 3.22</b> Discharge loss calculated for RIM-4 RF ion thruster. ....	48
<b>Fig. 3.23</b> Performance map of a RIT ion thruster family.....	49
<b>Fig. 4.1</b> Experimental discharge parameters of a 10-cm rf-ion source. ....	52
<b>Fig. 4.2</b> The first version iU-50 Ion Thruster (Ulsan – 2017).....	53
<b>Fig. 4.3</b> The optimized version iU-50 Ion Thruster (Ulsan – 2017) .....	53
<b>Fig. 4.4</b> Discharge loss for the reference RF ion thruster .....	54
<b>Fig. 4.5</b> The grids system for the first version iU-50 thruster.....	58
<b>Fig. 4.6</b> The grids system for the second version iU-50 thruster .....	58
<b>Fig. 4.7</b> The grids system for the second version iU-50 thruster .....	60
<b>Fig. 4.8</b> The grids system for the second version iU-50 thruster .....	61
<b>Fig. 4.9</b> The grids system for the second version iU-50 thruster .....	61
<b>Fig. 4.10</b> Schematic of hollow cathode.....	62
<b>Fig. 4.11</b> Prototype hollow cathode .....	63
<b>Fig. 4.12</b> Hollow cathode circuit at AARL lab .....	64
<b>Fig. 4.13</b> Size effect in power consumption.....	65
<b>Fig. 4.14</b> Power absorbed for iU-50 thruster for different ion beam current .....	66
<b>Fig. 4.15</b> Thrust and Isp of iU-50 thruster .....	67
<b>Fig. 4.16</b> iU-50 ion thruster was mounted inside AARL vaccuum chamber .....	68
<b>Fig. 5.1</b> Thruster-plasma system main parameter .....	70
<b>Fig. 5.2</b> Simulation circuit model at 13.56 MHz.....	73
<b>Fig. 5.3</b> Simulated result in LT-spice for RF antenna voltage and current.....	73
<b>Fig. 5.4</b> Simulated result in LT-spice.....	74
<b>Fig. 5.5</b> Simulated result in LT-spice for source voltage and current, for LCL.....	74
<b>Fig. 5.6</b> L-match including blocking and inductance of plasma. ....	75
<b>Fig. 5.7</b> Plot of the power transfer coefficient and efficiency over power.....	77
<b>Fig. 5.8</b> Plot of the power transfer coefficient and efficiency over frequency.....	77

<b>Fig. 5.9</b> Schematic of the iU-50 thruster discharge chamber .....	78
<b>Fig. 5.10</b> Mesh generated of the iU-50 thruster discharge chamber .....	79
<b>Fig. 5.11</b> Surface plot of the LTE plasma temperature inside the discharge chamber.....	80
<b>Fig. 5.12</b> Plot of the velocity magnitude .....	80
<b>Fig. 5.13</b> Plot of the plasma electrical conductivity.....	81
<b>Fig. 5.14</b> Norm of the magnetic flux.....	81
<b>Fig. 5.15</b> Coil current as a function of time for a fixed excitation power .....	82
<b>Fig. 5.16</b> Mesh generated for plasma thermal model.....	84
<b>Fig. 5.17</b> a) Plot of the electron density distribution; b) Plot of the electron.....	85
<b>Fig. 5.18</b> Plot of the magnetic flux density norm (T) at steady state .....	85
<b>Fig. 6.1</b> Details of the AARL thrust stand .....	87
<b>Fig. 6.2</b> Comparisom between weight and thery .....	90
<b>Fig. 6.3</b> Geometry of side view of the PCB electrostatic comb .....	92
<b>Fig. 6.4</b> Geometry of side view of the PCB electrostatic comb .....	92
<b>Fig. 6.5</b> Plot of the electric field and electric potential distribution.....	93
<b>Fig. 6.6</b> Simple AARL fin comb circuit.....	95
<b>Fig. 6.7</b> Fins comb fabrication with different W at AARL lab .....	96
<b>Fig. 6.8</b> Experiment PCB comb calibration seting up at AARL lab .....	97
<b>Fig. 6.9</b> The magnetic structure at AARL lab .....	99
<b>Fig. 6.10</b> Experiment set up for electromagnetic calibration system at AARL lab .....	100
<b>Fig. 6.11</b> Force as a function of coil current for engaged distance from 1 to 10 mm .....	101
<b>Fig. 6.12</b> A schematic of the popular RPA .....	102
<b>Fig. 6.13</b> A schematic of 3 <sup>rd</sup> grid power supply.....	102
<b>Fig. 6.14</b> The schematic of the PCB .....	103
<b>Fig. 6.15</b> The schematic of the PCB .....	104
<b>Fig. 6.16</b> The experiment set up for 3 <sup>rd</sup> grid power supply inhouse .....	105
<b>Fig. 6.17</b> Experiment result from Oscilloscope (Fluke 196C 100MHz).....	106

## List of tables

<b>Table 1.1</b> Operating parameters for thrusters with flight heritage .....	4
<b>Table 3.1</b> Fitting parameters for secondary electron yield data .....	18
<b>Table 3.2</b> Preliminary grid parameters for iU-50 thruster .....	24
<b>Table 3.3</b> Xe propellant energy properties.....	33
<b>Table 4.1</b> Geometrical discharge chamber.....	56
<b>Table 4.2</b> Geometrical ion optic system .....	59
<b>Table 4.3</b> Scheduled data of iU-50 thruster .....	68
<b>Table 6.1</b> Details of the results measurement .....	90

## Abbreviations

AARL	Aerospace Applied Research Lab
iU-50	Ulsan ion thruster 50W class
Isp	Specific impulse
RIT	Radio frequency thruster
EP	Electric propulsion
TRL	Technological Readiness Level
PPT	Pulsed plasma thruster
SERT	Space electric rocket test
LES	Lincoln experimental satellite
GEO	Geosynchronous satellite
NSSK	North south station keeping
PIC	Particle in cell
DSMC	Direct simulation Monte Carlo
ICP	Inductively coupled plasma

## **Abstract**

Today, it is quite common for many space propulsion applications of satellites and spacecrafts to practice the electric propulsion techniques, where both ion thruster and Hall thrusters have been successful. The trend is not restricted to an alternative thruster design with higher specific impulse (Isp), efficiency and long operation time that leads to increment in payload mass and available electric power. One of the promising electric thrusters is Radio Frequency Ion Thruster (RIT) that utilizes electro-magnetic field for plasma production and was first presented by Hittorf in 1884. Later on, there were various Radio Frequency plasma devices built from his ideal. These include RF ion sources for neutral beam injection systems of fusion devices, plasma processing for microelectronics, plasma etching, plasma deposition and plasma propulsion. Ideally, the work at Applied Aerodynamics Research Laboratory in University of Ulsan is focused on the development of RF ion thruster, which is called iU-50 ion thruster. The 50 W-class RF Ion Engine is an experimental ion thruster and will be tested in the vacuum chamber at Applied Aerodynamics Research Laboratory in University of Ulsan. The iU-50 has a conical discharge chamber having an inner and outer diameter of 50 mm and 61 mm respectively, with 61 mm length. A double grid system with 211 holes is implemented. iU-50 Ion Thruster is expected to produce a thrust and Isp of about 5 mN and 2600s at 2 sccm and 50 w of power consumption.

# Chapter 1. State of the art

## 1.1 Introduction to space propulsion

In the hundred years since electric propulsion (EP) was originally conceived, it has been developed by an increasing number of research and industrial entities worldwide [1]. To date a myriad of technological subclasses of EP exist [2, 3], each at a different Technological Readiness Level (TRL), from basic notions of particle acceleration techniques to space-proven application. During the first decades, following the first operation in space of an EP system in 1964, the most development efforts have been invested in maturing five main types of EP technologies – ion engines, pulsed plasma thrusters (PPT), resistojets, arcjets, and Hall thrusters.

The principal drivers supporting the research, development, and ultimately qualification of each of the five technologies were government entities, either space agencies or different branches of the military. Most of the early missions were technology demonstrators and served purely scientific or technological purposes such as the Vela, Space Electric Rocket Test (SERT), Zond, Lincoln Experimental Satellite (LES) or ‘Meteor’ missions [1,4]. With time, as EP technologies matured, new and improved propulsion systems were implemented to enable new satellite maneuverability and execute a variety of missions. The combination of mission requirements and commercial incentives resulted in EP technology being used principally in GEO communication and in Earth observation satellites. The lead players capable of developing and implementing EP technologies were the large geopolitical entities, namely the United States, Soviet Union, Japan, Europe, and China.

The first truly operational uses of electric propulsion were for spacecraft attitude control on the Russian Zond-2 in 1964 [5], which used pulsed plasma thrusters, and by the U.S. Vela satellites, which in 1965 used resistojets [6]. The first U.S. use of PPTs was on the U.S. LES and NOVA satellites [7,8], which in 1968 started using pulsed plasma thrusters for fine ephemeris control to

achieve a “drag-free” orbit. The first commercial use of electric propulsion was in 1981 with the launch of the Intelsat V series of GEO satellites, which used high power resistojets for North-South Station-Keeping (NSSK), followed rapidly by their use on RCA’s Satcom1 [9]. Unfortunately, while the use of high power resistojets continues successfully to this day on the original Iridium constellation (77 spacecraft) and many geosynchronous satellites (over 20 to date) [6], neither the use of PPTs nor resistojets precipitated a world-wide adoption of electric propulsion, likely due to the incremental nature of the performance improvement they provide.

In 1993, 24 years ago, Martin Marietta’s communications satellite Telstar 401 was launched and successfully operated using arcjet thrusters for GEO orbit north-south station-keeping [10] (Figure 1). While not the first communications satellite to use EP for station-keeping, it marks the point in time when EP technology changed the commercial satellite marketplace and drove the broad, worldwide adoption of EP technology. The use of arcjets for NSSK also demonstrated the crucial link between the selection of in-space propulsion technology and launcher requirements: the mass reduction enabled by arcjets resulted in a significant reduction in launcher costs. The commercial success of the Telstar 401 mission removed major barriers preventing private and commercial satellite operators from harnessing EP technology.



**Fig. 1.1** *Description of Telstar 401 – the first commercial satellite to use electric propulsion*

Following Telstar 401, there was a rapid increase in the number of satellite integrators implementing EP-based propulsion systems on their satellite platforms. Figure 2 presents the number of EP-based GEO satellites launched in the years 1993-2016. To compete with the strong advantages of arcjet technology, the additional primes adopted other forms of electric propulsion, such as gridded ion and Hall-effect thrusters. Over time, EP technology has made great technological and commercial progress. The main driver for the impressive advancement is the slow and steady commercialization of the space industry led by a constant demand for an increasing number of communication satellites. In parallel, EP technology demonstrated the capability to perform a variety of functions and is increasingly used in almost all space applications, from tiny CubeSats, through Earth observation satellites in LEO, to remote interplanetary missions [11]. At the beginning of the 1960s, the first RIT Ion Thruster with ionizer diameters from 4 to 35 cm has been studied, developed and tested at Physikalisches Institut in Justus-Liebig-Universität Gießen under the leadership of Professor H.Loeb. Based on his work, the RIT Ion Thruster was utilized by Eureka and Artemis in 2001.

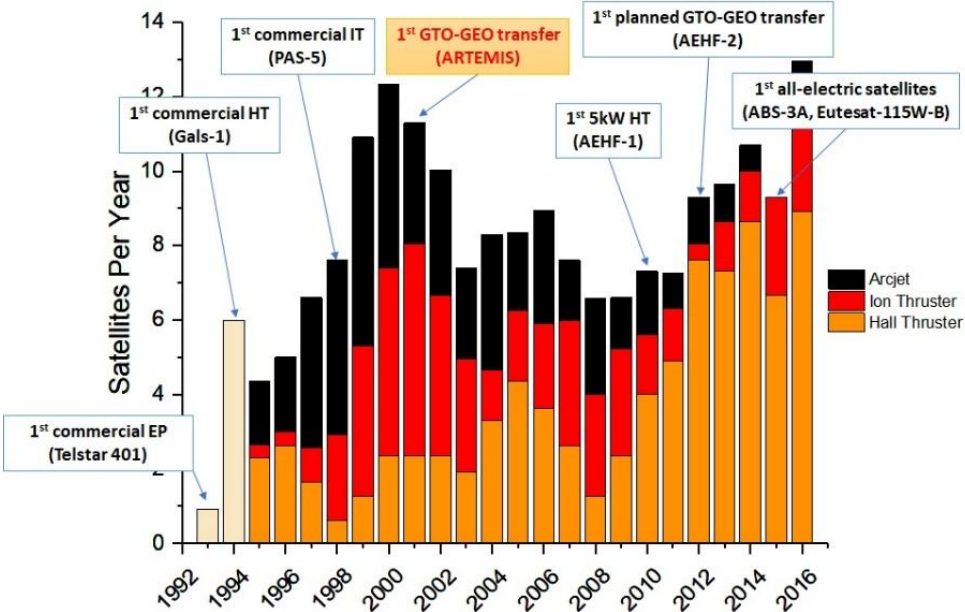
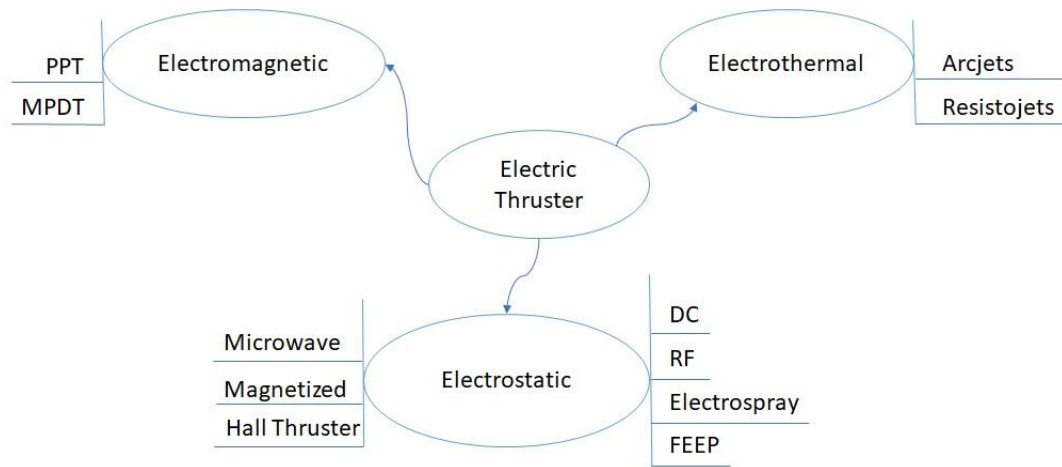


Fig. 1.2 Number of EP-based GEO satellites launched from 1993 to 2016

## 1.2 Introduction to electric thruster

Electric propulsion techniques [12] may be separated into three categories:



**Fig. 1.3** Common electric propulsion thruster

Some of the operating parameters of thrusters with flight heritage (resistojet, arcjet, ion, hall and pulsed plasma thruster (PPT)) are summarized in Table 1.1 [13].

**Table 1.1** Operating parameters for thrusters with flight heritage

Thruster	Specific Impulse (s)	Input Power (kW)	Efficiency Range (%)	Propellant
Arcjet	500 – 600	0.9 – 2.2	25 – 45	N <sub>2</sub> H <sub>4</sub> monoprop
Resistojet	300	0.5 – 1	65 – 90	N <sub>2</sub> H <sub>4</sub> monoprop
Ion thruster	2500 – 3600	0.4 – 4.3	40 – 80	Xenon
Hall thruster	1500 – 2000	1.5 – 45	35 – 60	Xenon
PPT	850 – 1200	< 0.2	7 – 13	Teflon

Thruster design with a higher specific impulse (Isp), efficiency and long operation time that leads to increment in payload mass and available electric power. One of the most promising facts of the electric thruster is the Radio Frequency Ion Thruster (RIT) designed to utilize electromagnetic field for plasma production. Furthermore, the advantage of RF ion thruster over

DC ion thruster is the absence of a thermionic electron emitter which can limit a lifetime of the satellite. Grid erosion by electrons impinging from the cathode can be eliminated and scaling-down is easier. Therefore, our project focused on studying a radio frequency ion thruster with extraction and acceleration grids.

### **1.3 Scope of dissertation**

This thesis was focused on the following motivations: development of an RF micro thruster, a 0-D analytical model for RF discharge chamber, 2D Ion extraction code incorporated into a numerical model of an RF ion thruster and development of the plasma plume diagnostic instruments. For 2D Ion extraction code development, enhanced Particle-in-Cell (PIC) and Monte Carlo collision (MCC) modeling with charge exchange and fast neutral particle treatment are considered. The specific subjects in this dissertation are as follows:

Firstly, a 0-D analytical model of the plasma discharge was previously developed without magnetic ring-cusp ion engine based on energy and particles balance equations for predicting RIT thruster discharge chamber performance and thruster efficiency improvement which are affected by the design process including the geometry of the discharge chamber, Ion optic, RF coil, and Gas inlet. The improved analytical model plays a critical role in estimating the performance of iU-50 RF Ion Thruster. Comparison with the previously reported analytic solution and experiment data showed the better prediction of the thruster performance. The most obvious advantage lies in the fact that it gives the possibility to reduce the amount of hour of the experimental work and cost.

Secondly, to improve the performance of the radio-frequency ion thruster, a grid system is designed for stability thrust control of iU-50 thruster. Herein, an ion optic simulator is developed for ion optics, plasma extraction and space charge dominated ion beam transport using Vlasov iteration. The code has several capabilities for solving electric fields in a defined geometry and tracking particles in electric and magnetic fields.

Thirdly, high efficiency and high performance radio-frequency (RF) power supply and rf coil placed around the discharge chamber is the crucial part of the iU-50 thruster development. For this purpose, the supply needs to guarantee highly efficient RF signal generation and transfer to the thruster coil and furthermore, an optimal power coupling between coil and plasma is required. In this thesis, we propose a high efficiency, high performance approach of matching RF by using a variable transistor design and RF coil configuration.

Finally, the plume diagnostic instruments were developed in order to understand the mechanism of generating thrust. The instruments include a retarding potential analyzer (RPA) design that is capable of measuring high level energy and high-density plasma beams. To overcome the limitations of existing RPAs measurement systems, a high voltage power supply with scan voltage from 0 V to 450 V was developed at our AARL lab. The RPA design parameters were determined by analyzing the electron density and temperature, the sheath thickness, and the ion density in the beam based on the Faraday probe and Langmuir probe measurements.

#### **1.4 Limitation of dissertation**

This study presented the design and manufacturing methods of RF iU-50 thruster. To design the small-scale thruster, a 0-D analytical model of the plasma discharge was developed without magnetic ring-cusp ion engine based on energy and particles balance equations for predicting iU-50 thruster discharge chamber performance and thruster efficiency improvement. These are affected by the design process including geometry of the discharge chamber, ion optic, RF coil and Gas inlet. However, this thesis has some limitation as follows:

- Synchronization and verifying between the analytical model and experimental data of iU-50 thruster are not performed to improve the iU-50 thruster configuration. However, this model was verified by experiment data from reference. Therefore, it can easily be applied to optimize iU-50 thruster.

- The synchronization PRA and Faraday probe do not experiment in the vacuum chamber.

## 1.5 Dissertation outline

This thesis presents the study, design and builds of an iU-50 ion thruster at AARL lab, University of Ulsan. The structure of this thesis is illustrated by the following:

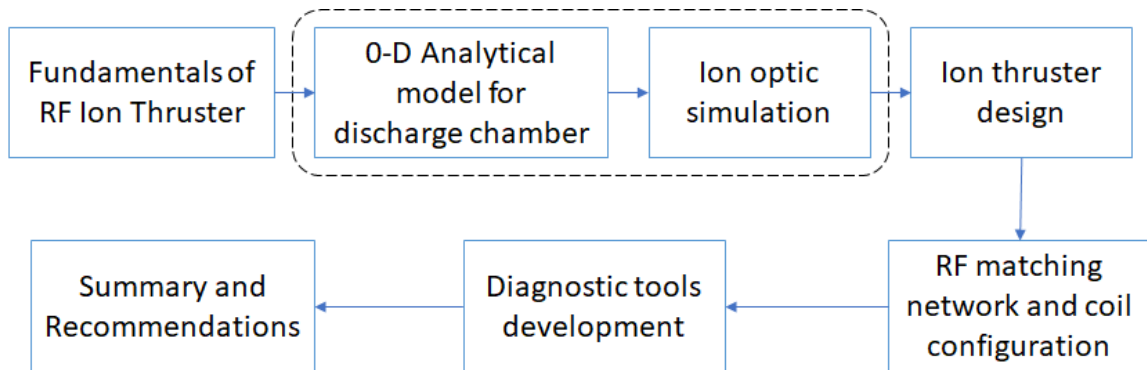


**Fig. 1.4** *Outline of chapters*

The structure of the dissertation begins with an overview introduction in Chapter 1. The fundamental of RF ion thruster is presented in Chapter 2. Chapter 3 presents the 0-D analytical model for discharge chamber and the 2D ion extraction model code incorporates into a numerical model of iU-50 thruster by using a particle in cell (PIC) method and direct simulation Monte Carlo (DSMC). In Chapter 4, the ion thruster design is developed under the results of the simulation. To ensure the successful operation of a thruster using inductively-coupled plasmas, the rf coil and matching network are presented in Chapter 5. For the investigation of the performance of the iU-50 thruster, thrust stand plasma plume diagnostics were presented in Chapter 6. Finally, conclusion and future works are performed in Chapter 7.

## Chapter 2. Theory and Background

This chapter provides the theoretical basic. As the research develops, a better understanding of the detail physics of the electric propulsion system is provided. Following the basic principles, the process of ionizing the propellant is discussed to determine the feasibility of electromagnetic ionization. Thereafter, the different methods of accelerating the ions are studied in order to determine the optimal method for high performance.

### 2.1 Fundamental of thruster

A rocket-propelled spacecraft in free flight receives its acceleration from expelling mass (the propellant). Its equation of motion is derived from a force equation that balances the rates of change of momentum of the spacecraft and the ejected matter:

$$m\dot{v} = -\dot{m}v_g \quad (2.1)$$

Where  $m$  is the total mass of the spacecraft (including unspent fuel). At a given time,  $\dot{v}$  is the magnitude of its acceleration,  $v_g$  is the magnitude of the exhaust velocity of the propellant and  $\dot{m}$  is the rate of change of the spacecraft of total mass due to mass expulsion ( $\dot{m} < 0$ ). The challenge for space propulsion is to achieve the highest possible exhaust velocities and to fully ionize the propellant in order to make best use of it. This can clearly be seen after integration of (2.1) between any initial mass  $m_o$  and some final mass  $m_f$ . For constant exhaust speed, this gives

$$\Delta v = v_g \ln \frac{m_o}{m_f} \quad (2.2)$$

Showing that for a given reduction in mass, the change in the spacecraft speed during a given period of acceleration is proportional to  $v_g$ . The propulsion community usually uses two quantities to characterize thruster: thrust and specific impulse, respectively.

$$T = \dot{m}v_g \quad (2.3)$$

$$I_s = \frac{v_g}{g} \quad (2.4)$$

Where  $g$  is the acceleration due to the Earth of the gravity at sea level.

## 2.2 Plasma propulsion

Electric propulsion achieves high specific impulse by the acceleration of charged particles to high velocity. The charged particles are produced by ionization of the propellant gas, which creates both ions and electrons forms what is called a plasma.

### 2.2.1 Concept of Radio-frequency

Plasma reactors used for electric propulsion are often driven at frequencies lying between 1MHz and 200MHz, that is with the radio-frequency (RF) domain as shown in Figure 2.1.

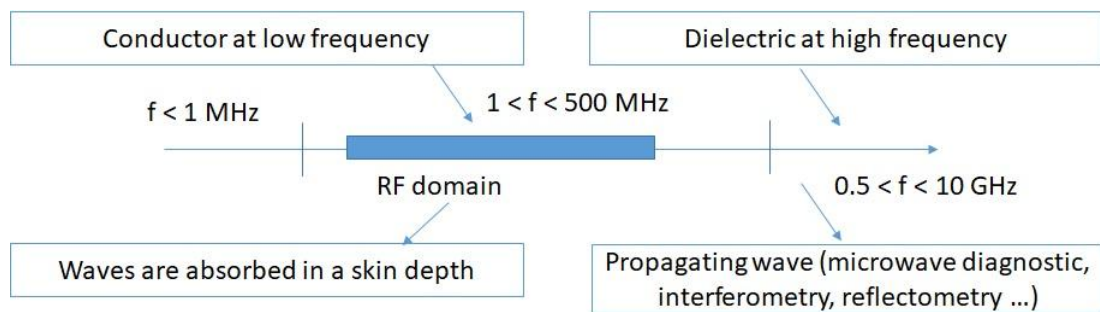


**Fig. 2.1** *Electromagnetic properties in the different frequency ranges*

In particular, the helicon sources used for space plasma propulsion are also driven in the RF domain, usually at 13.56MHz. The RF range is of particular interest as at the lower end all except the most massive ions in the gas discharge plasmas are able to follow the instantaneous RF fields and at the higher end, all ions are inertially constrained, responding only to the time-averaged fields. Throughout the RF range, electrons are able to respond instantaneously to fields.

RF electromagnetic fields can be generated in many ways, for instance by applying an RF voltage across two parallel electrodes or by circulating RF currents in coils or antennas, either

immersed in the plasma or separated from by a dielectric window. The electromagnetic fields will couple to the electrons in the plasma and transfer energy to them to sustain the plasma. The efficiency with which power is coupled from the power supply into the charged particles and the plasma uniformity both strongly depending on the design of the RF excitation. The two classical RF reactor used in industry is the capacitively coupled plasmas (CCP) reactor, a schematic of which is shown Figure 2.2 (a), and the inductively (or transformer) coupled plasma (ICP, TCP) reactor shown in Figure 2.2 (b).

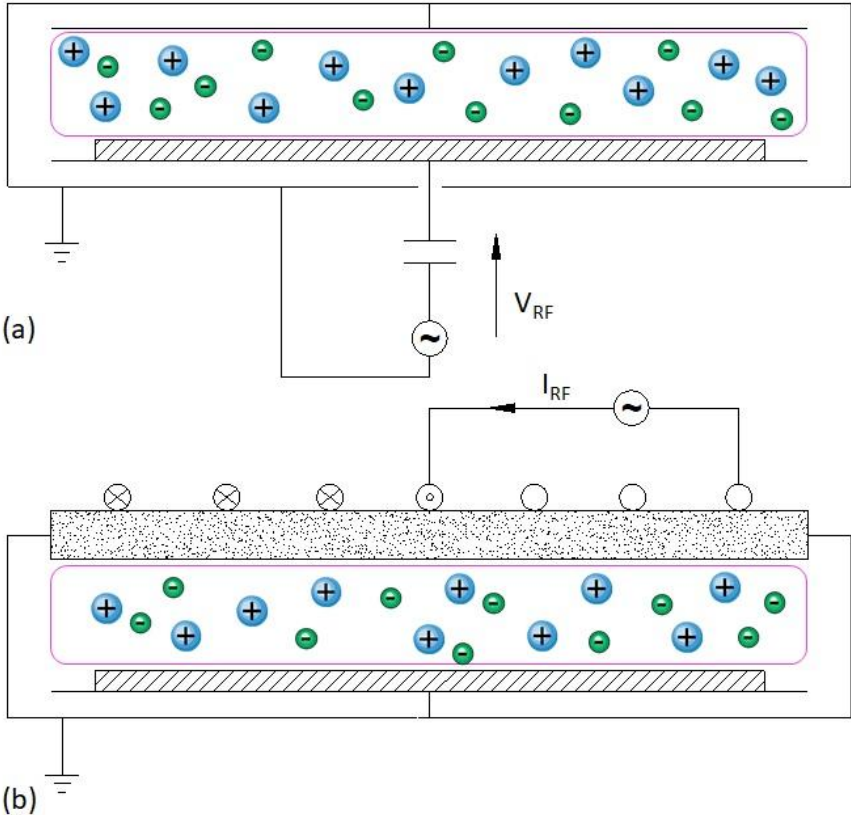


**Fig. 2.2** Electromagnetic properties in the different frequency ranges

Capacitively coupled plasma reactors have some natural limitations. Although very high-frequency CCPs achieve high plasma density (typically  $n_e \approx 10^{17} \text{ m}^{-3}$ ), this is accompanied by major uniformity problems. Moreover, the ion flux and the ion energy cannot be varied totally independently, even when multiple-frequency excitation is employed. Inductively coupled discharges overcome these limitations to some extent. In this thesis, iU-50 thruster was developed

based on the inductively coupled plasma theory. ICPs are usually associated with two regimes, the so-called E (electrostatic) mode for capacitive coupling and the so-called H (electromagnetic) mode for inductive coupling. Inductive reactors with an external coil generally start in the E-mode and undergo an E–H transition when the plasma density reaches a critical level as power to the coil is increased [14]. The energy of ions incident on a substrate electrode immersed in an inductively coupled plasma can be adjusted independently of the ion flux using a separate power supply for biasing. The amount of power transferred to the plasma electrons by the bias supply is usually such that the RF power from the substrate-holder contributes only marginally to the plasma density (and thus to the ion flux). It is the power supplied to the ICP coil that controls ion flux. Inductively coupled plasma (ICP) reactors for plasma processing can be divided into two main geometric designs: cylindrical source tube with an expanding chamber and planar coil geometry.

### **2.2.2 Description of Radio-frequency ion thruster**

The previous ion thrusters utilize a thermionic hollow cathode and DC power supply to inject a hot electron into the discharge chamber to ionize the propellant gas. To eliminate any potential life or power supply issues with the hollow cathode and DC-electron discharge, an alternative thruster design utilizes electromagnetic fields to heat the plasma electrons that, in turn, ionize the injected gas. One method to achieve this goal is to use an inductive plasma generator, that is described in the previous sections. The ICP generator is normally called a radio frequency ion thruster.

According to Figure 2.3, the RIT Ion Thruster basically consists of the neutral propellant (xenon gas or iodine-fueled [15]) which is injected into the discharge chamber and Plasma is generated by a coil that surrounds the cylindrical, conical or even hemispherical dielectric wall (Alumina, quartz...) and system of electrodes grids accelerated ions inside the discharge vessel.



screen grid but also possibly controls the neutral density to pressure since unionized neutral propellant leaks through the grids.

### **2.2.3 Advantages**

Gridded ion engines have a long history of operation and their reliability has been proven. Though high efficiency is achievable, thrust density is intermediate at best since extractable ion beam is limited by the space-charge current between the grids. They do, however, possess significant Isp advantage over chemical rockets as well as other EP thrusters because of its purely electrostatic acceleration mechanism. Among various ion engine designs, the RF type is the simplest as it does not require any magnetic structure. The absence of an applied magnetic field also means that the thruster can be operated away from a specific discharge condition, resulting in a wider thrust and power range.

Durability is another favorable trait of RF ion engine. Service life can be greatly extended by eliminating the need for an internal cathode, which is highly susceptible to erosion problems. Long service life makes RF ion engines perfect for long-term missions such as interplanetary travel and station-keeping/drag make-up at high-altitude orbit. Eliminating the internal cathode can also translate to a reduction of ion production cost as high-energy (30-40 eV) primary electrons no longer exist, so energy is less likely spent in creating double ions. The combining effect of no magnetic structure and no internal cathode helps reduce the required volume of the thruster and saves mass, making miniaturization of the thruster much simpler.

### **2.2.4 Inconvenience**

Despite their numerous advantages, RF ion engines have not been fully accepted by the U.S. space industry. One barrier involves the development of a highly efficient RF amplifier. Although good efficiency is not difficult to achieve because of the low operating frequency (order of MHz rather than GHz), problems still exist regarding scaling down the amplifier components.

Developing high-efficiency RF power electronics at smaller scales is an active field of research but is not within the scope of this thesis.

Despite their numerous advantages, RF ion engines have not been fully accepted by the U.S. space industry. One barrier involves the development of a highly efficient RF amplifier. Although good efficiency is not difficult to achieve because of the low operating frequency (order of MHz rather than GHz), problems still exist regarding scaling down the amplifier components. Developing high-efficiency RF power electronics at smaller scales is an active field of research but is not within the scope of this thesis. Other issues of RF ion engines mainly concern the complex design methodology. The RF circuit needs to be designed for high power coupling efficiency so the source does not dissipate power within the transmission circuit. This is referred to as impedance matching and requires the knowledge of the plasma's electrical properties, which are not known a priori. The selected operating frequency needs to produce the proper skin depth for RF power deposition. Such a mechanism is related to the plasma conductivity, gas pressure, chamber geometry, and coil geometry. All these parameters intertwine together and form a very complex design problem. On top of that, parasitic power loss such as ohmic heating of the coil adds extra design constraints as its electrical resistance could vary with temperature as well as driving frequency.

### **2.3 Summary**

In this chapter, the fundamental theory of electric thruster was studied in order to determine the feasibility of electromagnetic thruster for propulsion. The fundamental of the thruster is discussed. Thereafter, the pros and cons of the RF ion thruster are discussed. As the research develops, the better understanding of the detailed physics of the RF ion thruster is discussed in chapter 3.

## Chapter 3. 0-D Analytical model for discharge chamber

### 3.1 Introduction

The main purpose of 0-D Analytical model for discharge chamber is to understand in detail the processes which occur during RIT operation. Creation of simple models based on power and particle balance and more complicated models which include magnetohydrodynamic equations, leads to better understanding of the modeling object, and shows the extent of the influence of the thruster construction on thruster performance. Also, as a consequence, there is reduction in experimental work. Hence this leads to reduction in cost of the thruster and more importantly, the computational models let us to create the generator with high performance which satisfies high requirements for contemporary space industry. Computational modeling of radio frequency discharge is widely used. There are a number of works which describe simulation of plasma for RIT, for example Goebel [16], that suggested a zero-dimensional analytical discharge model that can be used to understand the performance of RF ion thruster. Even though it does not consider the effect of one-dimensional field distribution, that can be obtained from numerical simulation [17], it can provide a reasonable estimation of the performance of RF ion thruster. Chabert et al. [18] reported that the analytical modeling can improve the result by considering power transfer efficiency. However, it still lacks in considering some important effects such as induced magnetic field in RF ion thruster. Kanev et al. [19] applied the analytical model to cylindrical and semi-spherical discharge vessels. Due to the fact that the model still did not consider some important physical phenomena in RF discharge, the result was still not good to predict the performance of RF ion thruster in some operational regime.

Two-dimensional models [20-22] for RIT have been developed for decades and are still being developed. These models are based on magnetohydrodynamic equations for the plasma

calculation and Maxwell equations for simulations of the electromagnetic field. Nowadays, models of PIC simulation of plasma inside RIT are being developed. This is future work for my Ph. D.

Unfortunately, there is no ready software for modeling low-temperature plasma [23]. Thank for the fruitful research and development of RIT and RF ion sources at JLU, University of Giessen. An example of this arrangement applied to a RIT-XT thruster [24] from JLU is shown in Figure 3.1. In this case, the body of the thruster consists of a conical (or hemispherical) alumina insulator, and a high-conductivity material (typically copper) antenna coiled around the insulator. As long as the alumina body is not significantly coated by conductive layers and remains insulator, the RF fields will couple through the system and generator plasma. In this thesis, we would like to present our 0-Analytical discharge model for RF ion thrusters, which allows for a short time optimized geometry of the discharge chamber.

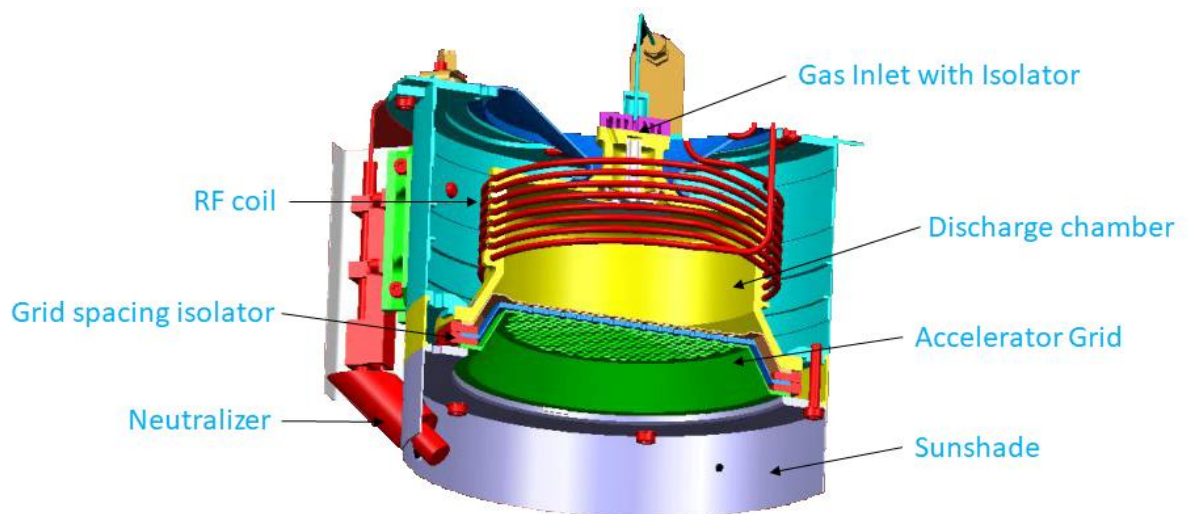


**Fig. 3.1** Schematic of an RIT 10 (10 cm diameter) ion thruster with a conical shape modeled

### 3.2 Description of the model

This section shows the implementation of the analytical model focusing on the input and the output parameters. For the sake of simplicity, consider first plasma chamber geometry including volume  $V_{\text{conical}} = \frac{1}{3}\pi(r_1^2 + r_2^2 + r_1r_2)h$  and the wall area  $A_w = \pi(r_1 + r_2)l + \pi r_2^2$ . The geometrical optics output parameters (Clausing factor [25], effective transparency of the screen grid and the grid optical transparency [26]) needs to be determined to calculate the neutral gas density and ion beam current  $I_b$ . A flow chart is given in Figure 3.1

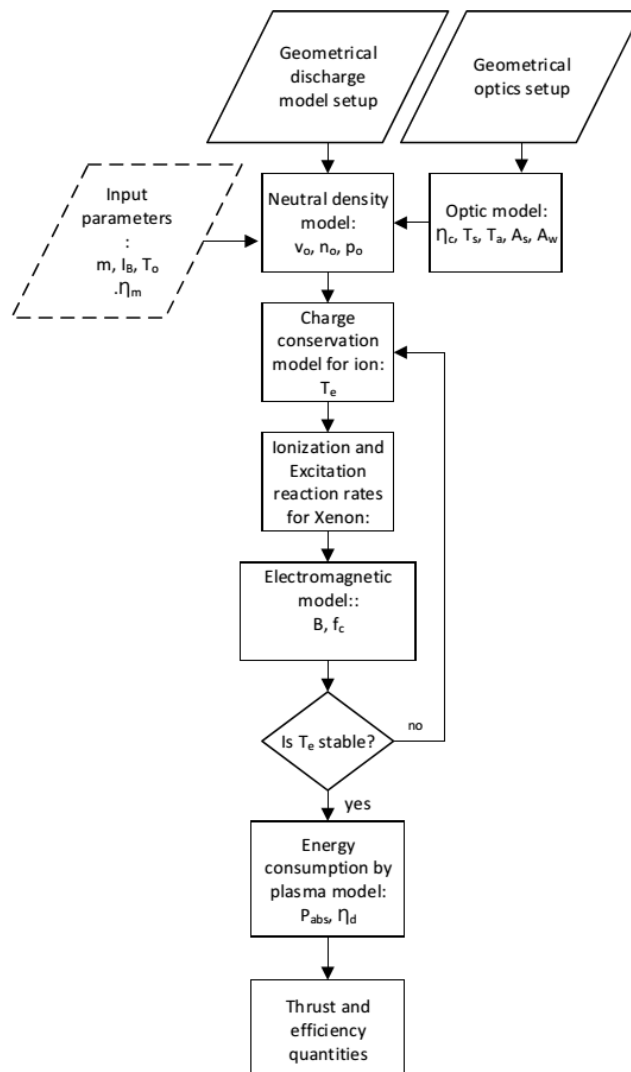


**Fig. 3.2** Flow chart of the analytical discharge model

RF plasma is quite uniform inside the discharge chamber but there is weak dimensional dependence except for near wall. The plasma in this discharge vessel is assumed quasi-neutral that is  $n_i \approx n_e$ . In view of the fact that the plasma remains quasi-neutral, any rapid spatial change in potential occurs in the space charge sheath rather than in the plasma. Additionally, in the RF Ion Thruster with the dielectric wall, the power loss due to electron and ion entering toward the wall through the rf sheath represents the most significant power loss. The power loss to the wall can be estimated from the sheath potentials in the plasma edge. In the RF Ion Thruster, the wall is insulating, so the net ion and electron currents to the surface must be equal. Additionally, the energies characteristic of hall thrusters produces a significant number of secondary electrons [12] through insulator materials, such as alumina ( $Al_2O_3$ ), which reduces the sheath potential and increases the power loading in the plasma. Calculations of the electron temperate in the reference RF Ion Thruster ESA XX by equating the ion production and loss terms in the discharge chamber corresponding to the ion current from 0.78 – 2 Amps show electron temperature well in the range of 0-20 eV. Secondary electron yields reported in the literature [27,28,29] for several materials used for the walls of RF Ion Thruster are defined by the secondary electron yield as  $\gamma = \Gamma(2 + b)aT_{eV}^b$ , where the electron temperature is in electron volts, the gamma function is  $\Gamma(x)$  and the coefficients a, b is found in table 3.1.

**Table 3.1** *Fitting parameters for secondary electron yield data*

	a	b	$\Gamma(2 + b)$
Alumina ( $Al_2O_3$ )	0.145	0.650	1.49
Stainless steel	0.040	0.610	1.44

The transparency for neutral propellant that leaks through the grids is  $\beta_g$  with  $0 \leq \beta_g \leq 1$ . Therefore, the open area of the grid system is  $A_g = \beta_g \pi R^2$ , and then no gas leaking out the volume

( $\beta_g = 0$ ). At the uniform plasma inside the discharge chamber, the total ion loss area is  $A_t = A_g + f_c * A_w + A_{bw}$ , where  $f_c$  and  $A_{bw}$  are the Bohm current reduction factor to the wall due to an AC magnetic field is generated by the RF current flowing in the coil with a frequency at the RF oscillator frequency and back wall area.

### 3.3 Plasma sheaths

In order to understand the design of the grid system, the sheaths formed at the boundaries of the plasma needs to be studied. The boundaries of the plasma represent the sections through which charged particles enter and leave the plasma and the thruster. The plasma, that is created inside the chamber, will form density and potential variations at the boundaries, in order to satisfy particle balancing for a quasi-neutral plasma. These potential variations are due to the different mobilities and temperatures of electrons and ions and are called sheaths.

If the potential gradient is small in comparison to the electron temperature  $T_e$ , a Debye sheath is established. If the potential is much greater than  $T_e$ , a Child-Langmuir sheath is established [12]. A Child Langmuir sheath is obtained when the potential gradient across the sheath is sufficiently large, causing electrons to be repelled from the sheath's thickness. The electron density is essentially zero at the sheath's edge. The Child-Langmuir sheaths ensure that ions are accelerated through the multi-aperture grids with reasonable direction. In addition, it also ensures that the electrons are reflected. The extraction of electrons will increase the extracted current density, which will have a negative impact on the performance of the thruster. This is because there is a maximum current a gridded ion thruster can extract. Therefore, the current must be mostly due to the large ions that will produce a greater amount of thrust in comparison with the small electrons. The equation for Child-Langmuir can be written as

$$J_i = \frac{4\sqrt{2}}{9} \epsilon_0 \left( \frac{e}{m_i} \right)^{1/2} \frac{V_T^{3/2}}{l_g^2} \quad (3.1)$$

The equation was derived by Child [30] in 1911 and Langmuir [31] in 1913. The equation states that the current per unit area that can pass through a sheath is limited by the space charge effect, and is proportional to the voltage  $V_T^{3/2}$  divided by the sheath thickness  $l_e^2$ .

Figure 3.3 illustrates the Child-Langmuir length for two single charged ion current densities. As can be seen, a 2.5 mm diameter aperture has a maximum space charge current density for Xenon gas of approximately 5 mA/cm<sup>2</sup> at 1500 V. Thus, the total ion current per aperture is only 0.25 mA. The total estimation thrust can be determined by equation 3.2, as follows

$$T = F_{\text{screen}} + F_{\text{accel}} = \frac{1}{2} \epsilon_0 (E_{\text{screen}}^2 - E_{\text{accel}}^2) \quad (3.2)$$

The thrust per aperture for this current and voltage is only about 16  $\mu$ N. Although this amount of thrust is very low, if multiple apertures are used, then the amount of thrust will greatly increase  $\sim$  3 mN.

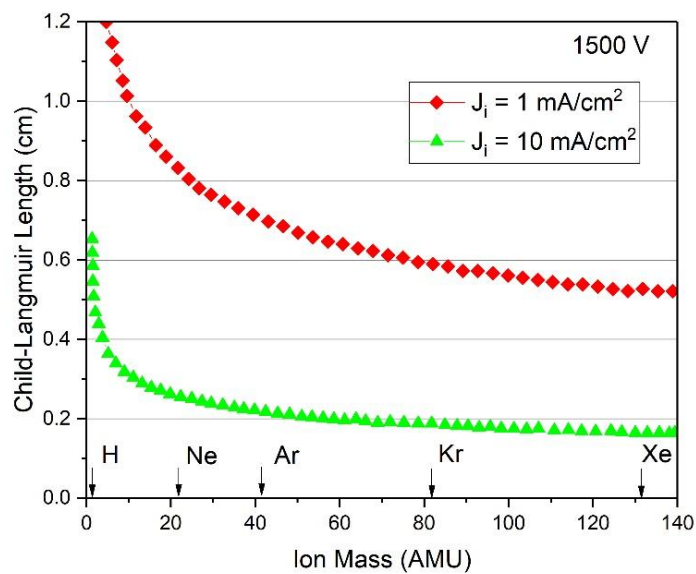


**Fig. 3.3** Child-Langmuir sheath length versus various propellant at 1500 V acceleration voltage for two ion current densities [12]

### 3.4 Grid consideration

The ideal grid design will extract and accelerate all the ions that approach the grid-system whilst blocking the electrons and neutral gas outflow. If the grid design only contains an acceleration grid, then the only ions that are accelerated through the aperture are those that arrive on axis with the apertures. The ions that are not aligned with the apertures are accelerated into the acceleration grid itself, which will cause rapid erosion. Therefore, a screen grid with apertures aligned to the acceleration grid is introduced. This will help prevent unwanted collision of ions, as shown by Figure 3.4. The screen grid typically has a positive potential that will help confine some of the electrons and ensure that the ions that collide with the grids have relatively low energy.

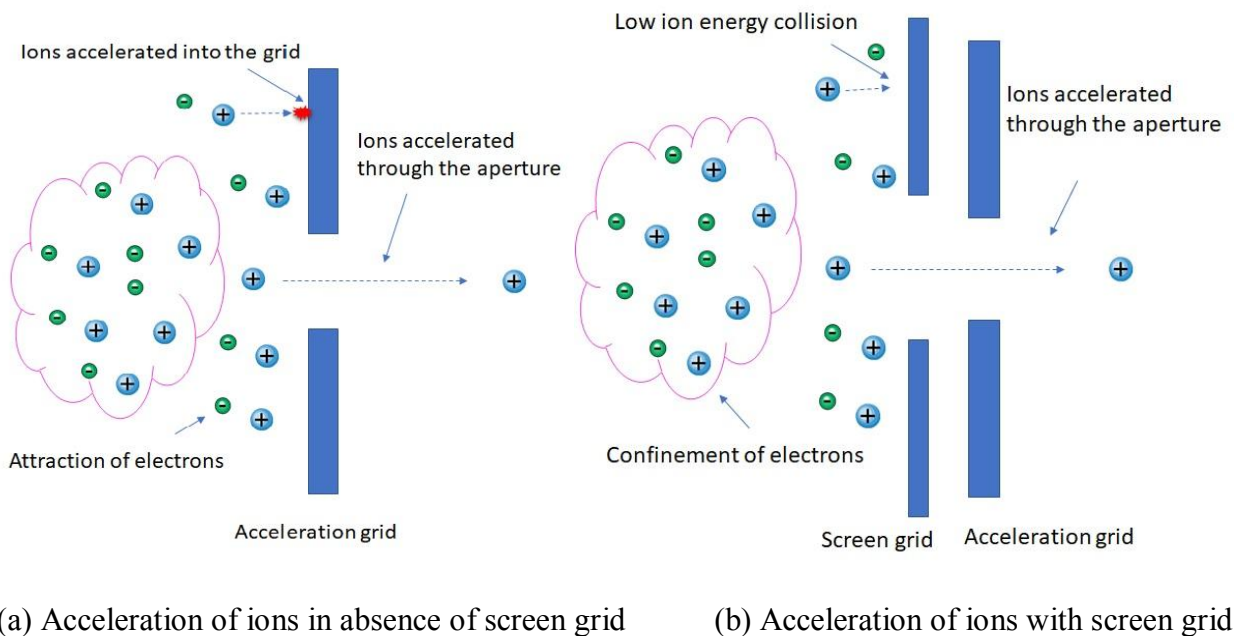


**Fig. 3.4** *Effect of screen grid on charged particles in a plasma*

The screen and acceleration grids, together, are known as the ion optics. Figure 3.5 shows the five degrees of freedom for the ion optics: screen grid thickness; acceleration grid thickness; screen grid aperture diameter; acceleration grid aperture diameter; and the distance between the two grids.

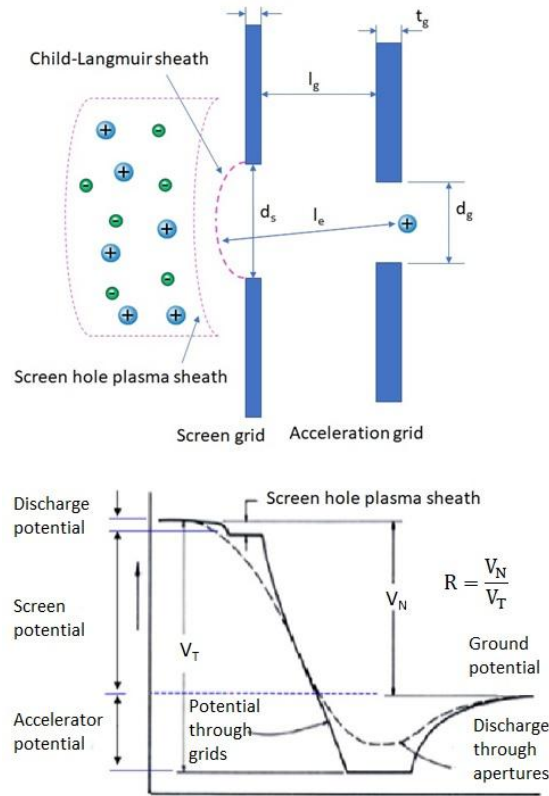


**Fig. 3.5** Plasma sheath layout and potential on-axis in an individual beamlet and between the beamlets intersecting the grids

From equation 3.2, the normalized Perveance per hole depends on the effective acceleration length,  $l_e^2$

$$\frac{J_B}{V_T^{3/2}} \left( \frac{l_e}{d_s} \right)^2 = \frac{4\sqrt{2}}{9} \epsilon_0 \left( \frac{q}{m_i} \right)^{1/2} \quad (3.3)$$

From the figure 3.5, we have:

$$l_e = \sqrt{l_g^2 + \left( \frac{d_s}{2} \right)^2} \quad (3.4)$$

$$V_N = V_D + V_S \quad (3.5)$$

$$V_T = V_N + |V_A| \quad (3.6)$$

Where  $V_N$  is the net acceleration voltage,  $V_D$  is discharge voltage,  $V_S$  is the screen potential,  $V_T$  is the total acceleration voltage. Furthermore, normalized Perveance per hole also depends on the voltage ratio,  $R$

$$R = \frac{V_N}{V_T} = \frac{V_N}{V_N + |V_A|} \quad (3.6)$$

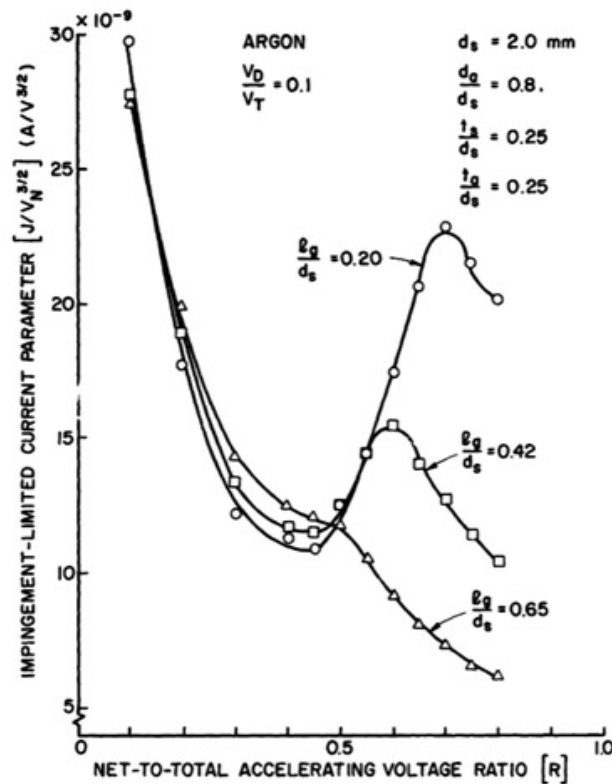


**Fig. 3.6** Comparison of Impingement-Limited Current Levels as Function of Grid Separation and Net-to-Total Accelerating Voltage Ratio

Figure 3.6 shows the Comparison of Impingement-Limited Current Levels as Function of Grid Separation and Net-to-Total Accelerating Voltage Ratio. As we can see in this figure, optimal Perveance occurs when  $l_g/d_s = 0.2$  and then maximum perveance for  $l_g/d_s = 0.2$  occurs when  $R$  is about 0.7. Then, choosing  $R = 0.75$  for lowering the accelerator potential. After that, the preliminary grids parameter design is shown in the following table 3.2.

**Table 3.2** Preliminary grid parameters for iU-50 thruster

Number of Apertures	211
$V_S$ is the screen potential [V]	1500
$V_A$ is the Accel. potential [V]	-150
Screen Grid hole Diam. [mm]	2
Screen Grid thickness [mm]	0.5
Accel Grid hole Diam. [mm]	1.25
Accel Grid thickness [mm]	1
Screen/ Accel Grid sep. [mm]	0.5 ÷ 1.5

### 3.5 Ion optics model

Numerical simulation of ion optics is performed with an open-source ion optics code simulation IBsimu developed by Kalvas [32]. The model solves electric fields in a 2-D axisymmetric for model integral domain as well as for quick analysis of the ion extraction and ion beam through accelerator grid. To accelerate ions at high speed, the grid potential needs to be reasonable. Figure 3.7. presents a photo image of the 2-D axisymmetric half-beamlet ion trajectories and potentials applied as boundary conditions for the UOU grid model with optimal perveance.

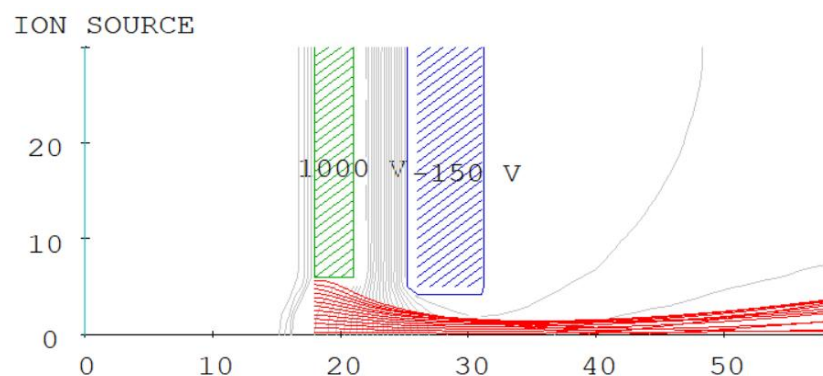


**Fig. 3.7** 2-D axisymmetric well-focused ion beams and parallel trajectory for the iU-50 thruster

The ion trajectories are generally more well-focused ions beam and parallel than with optimal perveance than that of over-perveance or under-perveance which are shown in Figure 3.8, that is, this depends on the Child-Langmuir sheath forms presenting in the I-gun code simulation.

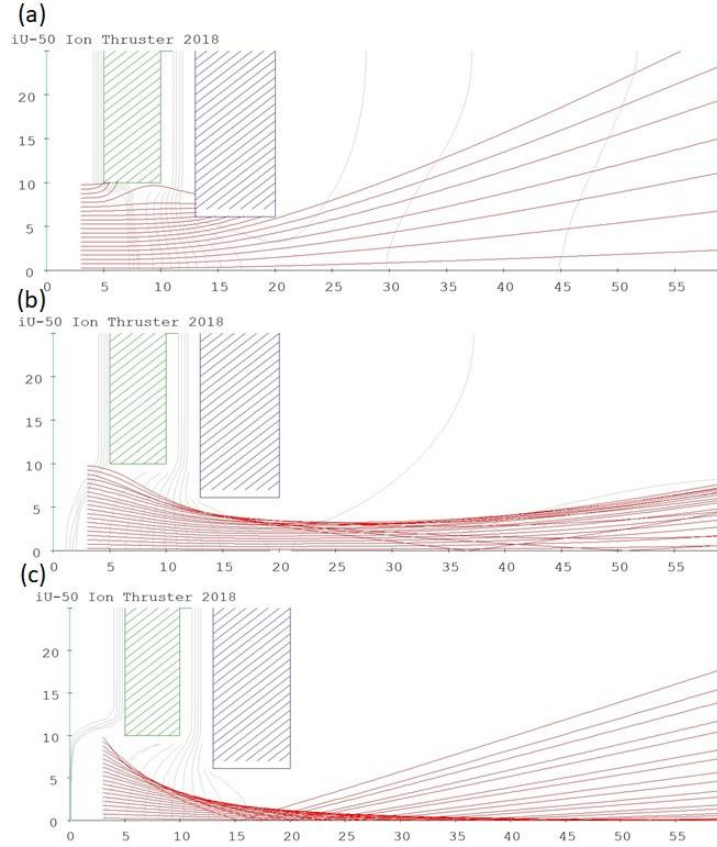


**Fig. 3.8** Representative ion trajectories from a I-gun calculation for three perveance conditions: (a) over-perveance with direct accel grid interception, (b) optimal perveance, and (c) under-perveance that can produce cross-over interception

The extracted beam has been also effected on the screen grid transparency, or more precisely, the effective transparency of the ion optics system  $T_{\text{eff}} = I_b/I_B$  [17]. As the boundary condition, the ion beam current  $I_b$  is given by the Bohm current that ions flow through the screen grid transparency as follows

$$I_b = \frac{1}{2} n_i e v_e A_s T_{\text{eff}} \quad (3.1)$$

Where  $n_i$  is an ion density inside the discharge chamber,  $v_e = (kT_e/M_{xe})^{1/2}$  is the Bohm velocity. In this work, IBSimu could estimate the beam divergence half-angle  $\theta_b$  as well. The first order estimation is utilized to determine the grid optical transparency  $T_a$  as follows

$$T_a = \frac{1}{(1/T_s) + (1/T_{\text{accel}}) - 1} \quad (3.2)$$

Where  $T_{\text{accel}}$  is the accelerator grid transparency. Farnell proposed the conventional relationship between the screen and the accelerator grid transparencies, that is,  $T_{\text{accel}}/T_s = 0.36$ .

### 3.6 Neutral gas model

It is essential that the neutral gas density  $n_0$  is accurately calculated in the discharge chamber. Because the singly ionized particle production rate and the excited neutral production rate is generated from the neutral density and it also defines the magnitude of electron temperature. When the plasma is switched on, the neutral gas is unionized that would escape the chamber is  $Q_{\text{out}} = Q_{\text{in}} - I_B/e$ , with the neutral gas leaks through the grid is  $Q_{\text{out}} = \frac{1}{4} n_0 v_0 A_g T_a \eta_c$ , with the neutral gas velocity is  $v_0 = (8k_B T / \pi M_{xe})^{1/2}$  and a resistance defined by the Clausing factor  $\eta_c$  [25], Which defines the reduced conductance of the grids with finite thickness. This factor determines the molecule transmission probability through the ion optics and is found by dividing the incident molecular flux  $G$  integrated over the downstream grid surface (grid 2) by the total incoming flux  $J$  integrated over the upstream grid surface (grid 1) as follows:

$$\eta_c = \frac{\int G dA_2}{\int J dA_1} \quad (3.3)$$

To calculate the Clausing factor, the Monte Carlo technique is used [12]. Besides, a single ion thruster aperture represented in a 2-D axisymmetric geometry is modeled using the molecular flow module in Vizglow by employing the angular coefficient method. The Clausing factor

depends solely on the geometry of the grid system since it is nondimensional, regardless of the upstream neutral gas density. Using the model, we find that the Clausing factor for the iU-50 Ion Thruster ion optics grids is about 0.17. Vizglow also allows the neutral gas density distribution inside the aperture to be determined for a better understanding of how the ion optics arrangement constricts the neutral gas flow as shown in Figure 3.9. As can be seen, the neutral gas density decreases only slightly through the grid 1 aperture but then drops dramatically over grid 2.

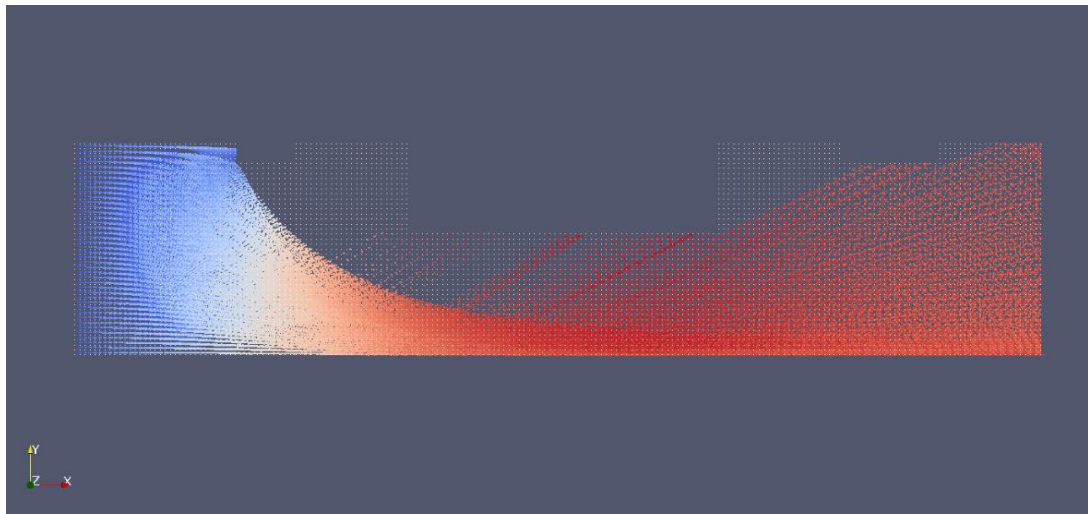


**Fig. 3.9** 2-D axisymmetric neutral gas density distribution normalized to the maximum value for iU-50 ion optics

The neutral gas density inside the discharge chamber is calculated from the given beam current and mass utilization efficiency as follows

$$n_0 = \frac{4I_B \alpha_m}{v_0 e A_g T_a \eta_c} \frac{\left(1 - \frac{\eta_m}{\alpha_m}\right)}{\eta_m} \quad (3.4)$$

It is assumed that singly charged ion and doubly charged ion exist together in the plasma. Using the equation of the thruster mass utilization efficiency, which is the ratio between the ionized and unionized propellant, for multiple species is  $\eta_m = \dot{m}_i / \dot{m}_p = \alpha_m (I_b M_{xe} / e \dot{m}_p)$  we obtain the mass flow input to discharge chamber

$$\dot{m}_p = \alpha_m \frac{I_b M_{xe}}{e \eta_m} \quad (3.5)$$

Where  $\alpha_m$  is coefficient for a doubly charged ion in the beam current,

$$\alpha_m = \frac{1 + \frac{1}{2} \frac{I^{++}}{I^+}}{1 + \frac{I^{++}}{I^+}} \quad (3.6)$$

Then, we set the neutral gas flow rate  $\dot{m}_p$  in standard cubic centimeter per minute units as a boundary condition on the discharge chamber gas inlet surface area.

The neutral pressure in the discharge chamber,  $P_0$ , during operation of the thruster, can be found using this expression and the conversion

$$P_0 = 1.04 \times 10^{-25} n_0 \times T_0 [K] \quad (3.7)$$

Where  $T_0$  is the neutral gas temperature in the discharge vessel. The pressure also affects plasma density with weak dependency on ICP frequency at low pressures, as shown in figure 3.10

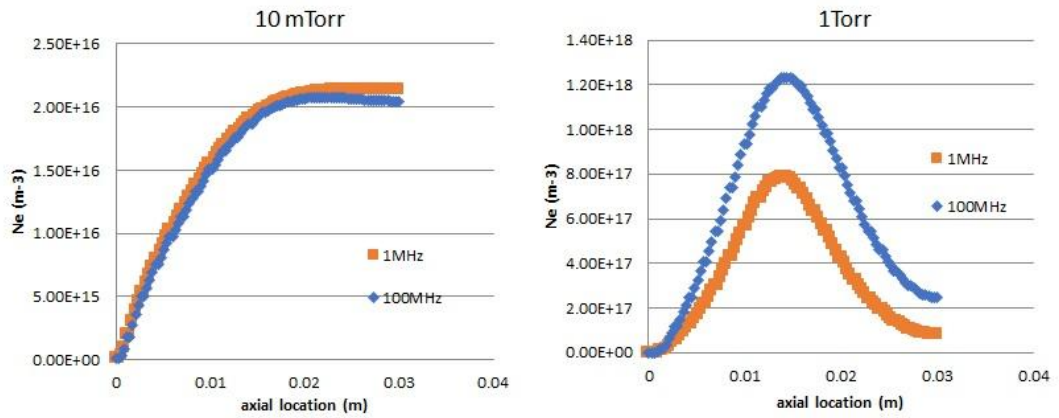


**Fig. 3.10** Pressure effect on plasma density

### 3.7 Plasma discharge model

The model follows the original work of Dan M. Goebel in development of Analytical discharge model that handle the discharge chamber configuration and the magnetic confinement physics found in the RF Ion Thruster. As RF ion thruster do not have localized electron sources such as hollow cathodes, and the inductive discharge operates in an E-mode it can experience transitions between E and H-modes. Therefore, the Maxwellian electron distribution is simply heated by the induced RF fields. This model is implemented in this work to optimize our RF Ion Thruster design. In this work, we consider a propellant in xenon gas and the plasma in this discharge vessel is assumed quasi-neutral that is  $n_i \approx n_e$ . The calculations are verified by the experimental data obtained from reference [33,34]. From this work, the parameters of the ion optics were referenced. Figure 3.11 shows a general view of the thruster. Figure 3.12 shows measured profiles of the power loss at different ion current levels. Thus, the calculations were able to be compared with experiment. The Mass efficiency coefficient has defined values from 0.3 to 0.9.

The model described here follows the terminology and method described for dc discharge ion thrusters in the reference paper [35,36]. It is first assumed that RF power absorbed by discharge plasma is simply given by  $P_{abs}$ . Assume that, the power out of plasma equals the  $P_{abs}$ .

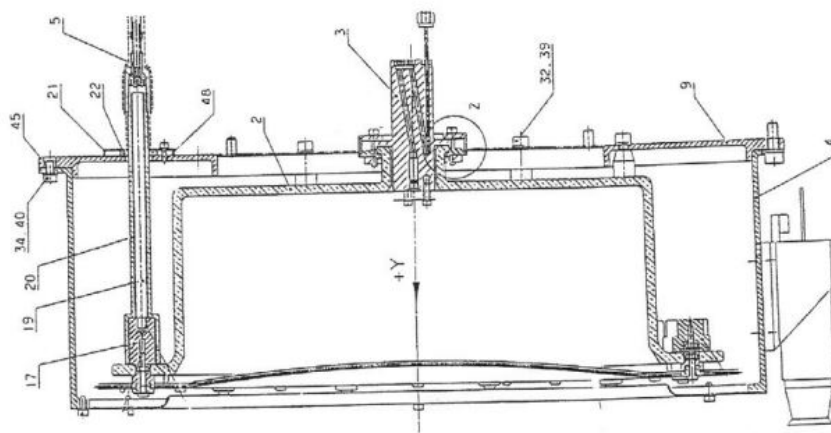


**Fig. 3.11** *ESA-XX general view*

**Table I** *ESA-XX Phase I performance characteristics at 200 mN thrust.*

Thrust	200 mN
Beam Voltage	2000 V
Total Power	6.2 kW
Beam Current	2.71 A
Total Efficiency	ca. 80%
Specific Impulse	4500 s
Beam Ion Production Cost	31 W/mN
Propellant Flow Rate	3.85 mg/s
Ion Production Cost	3.1 W/mN
I <sub>acc</sub> / I <sub>beam</sub> Ratio	1.5% - 3%

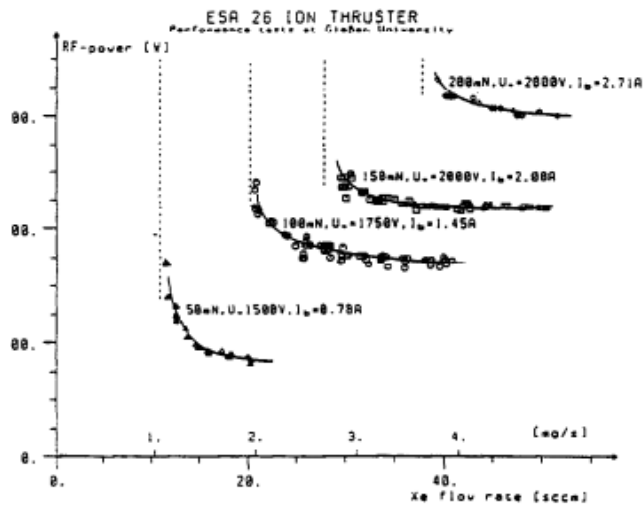


**Fig. 3.12** *Basic thruster performance at different ion current levels*

### 3.7.1 Particle and power balance

The total current produced  $I_{\text{Total}}$  is equal to the number of ionized particles that consists of singly ionized particle production rate  $I^+$  and double particle production rate  $I^{++}$ . This number is equal to the total loss of ions at wall, screen grid and ions current leaving plasma from the discharge chamber through the optical grid system which is given as

$$I_{\text{Total}} = I^+ + I^{++} = I_w + I_{\text{scr}} + I_b \quad (3.8)$$

This is due to the fact that there is no cathode emitting electrons in the discharge chamber. However, the discharge vessel is made by Alumina ( $\text{Al}_2\text{O}_3$ ) which should release the secondary electron from electron bombardment at high electron temperature. By particle balance for three species, the electron current leaving the discharge chamber  $I_e$  is same the total current produced  $I_{\text{Total}}$ , as follows

$$I_{\text{Total}} = I_e - \gamma I_e = (1 - \gamma)I_e \quad (3.9)$$

Where  $\gamma$  is the secondary electron yield from electron bombardment. The total ion current to the discharge chamber wall is

$$I_w = \frac{1}{2} n_i e \sqrt{\frac{kT_e}{M_{xe}}} A_w f_c \quad (3.10)$$

The very detailed explanation of the derivation of the confinement factor,  $f_c = v_i/v_{\text{Bohm}}$ , from the induced B-field which reduce ion loss to the wall, presented in the electromagnetic model. The ion current to the screen grid area  $A_{\text{scr}}$  trapping by the screen grid which is depended on the effective ion optics efficiency as

$$I_{\text{scr}} = \frac{(1 - T_{\text{eff}})}{2} n_i e \sqrt{\frac{kT_e}{M_{xe}}} A_s \quad (3.11)$$

The total ion current leaving the plasma can be found by substituting (3.1), (3.10), and (3.11) into (3.7), as follows

$$I_{\text{Total}} = \frac{n_i}{2} e v_a (A_w f_c + A_s) \quad (3.12)$$

The electron current leaving the plasma is the random electron flux times the Boltzmann factor as

$$I_e = \frac{n_e}{4} e \sqrt{\frac{8kT_e}{\pi m}} A \exp^{-e\phi/kT_e} \quad (3.13)$$

Where  $A = [A_w f_c + (1 - T_{\text{eff}})A_s]$  is the area which the electron flux reaching to it, the plasma potential  $\phi$  is obtained by equating the total ion and electron current leaving the plasma [ $I_{\text{Total}} = (1 - \gamma)I_e$ ], assuming quasi-neutrality in the plasma ( $n_i \approx n_e$ ), and solving for the potential gives

$$\phi = (1 - \gamma) \frac{kT_e}{e} \ln \left[ \frac{A_w f_c + (1 - T_{\text{eff}})A_s}{A_w f_c + A_s} \sqrt{\frac{2M}{\pi m}} \right] \quad (3.14)$$

The discharge loss is defined as the input power divided by the ion beam current as follows

$$\eta_{d\_loss} = \frac{P_{\text{abs}}}{I_b} \quad (3.15)$$

The global electron power balance can be obtained by equating the power absorbed  $P_{\text{abs}}$  by electrons to rate of power loss  $P_{\text{loss}}$ ,

$$\frac{d}{dt} \left[ \frac{3}{2} n_e kT_e \right] = P_{\text{abs}} - P_{\text{loss}} \quad (3.16)$$

The power out of the thruster:

$$P_d = P_{\text{ion}} + P_a + P_b + P_w \quad (3.17)$$

Where  $P_{\text{ion}}$  is the power to produce the ions that hit the walls and become the beam,  $P_a$  is the power to the anode due to electron collection,  $P_b$  is the beam power,  $P_w$  is the power to the channel

walls due to ion and electron loss,  $P_d$  is equal to the power absorbed. The power loss, which is equal to the power absorbed, is given to first order by

$$P_{\text{abs}} = I^+U^+ + I^{++}U^{++} + I^*U^* + (I_s + I_w + I_b)(0.5T_e + \phi) + I_a(2T_e + \phi) \quad (3.18)$$

The energy  $\varepsilon_i$  of the ions at the wall is given by

$$\varepsilon_i = \frac{T_e}{2} + \phi \quad (3.19)$$

Where the ions obtain  $\frac{T_e}{2}$  by falling through the presheath potential and then are accelerated by the sheath potential at the wall. The energy removed from the plasma by Maxwellian electrons for each electron that overcomes the negative going sheath at the wall is

$$\varepsilon_e = 2T_e + \phi \quad (3.20)$$

Where  $U^+$  is the ionization potential,  $U^{++}$  is the second ionization and  $U^*$  is the excitation potential. The value of these factors was shown in table 3.3.

**Table 3.3** *Xe propellant energy properties*

$U^+$ ionization potential [eV]	12.13
$U^{++}$ is the double ionization [eV]	21.2
$U^*$ is the excitation potential [eV]	10.1

$I^+$  is the singly ionized particle production rate,  $I^{++}$  is the double ionized particle production rate and  $I^*$  is the excited neutral production rate.

$$I^+ = n_o n_e e \langle \sigma_i^+ v_p \rangle V \quad (3.21)$$

$$I^{++} = n_e^2 e \langle \sigma_i^{++} v_p \rangle V \quad (3.22)$$

$$I^* = \sum_j n_o n_e e \langle \sigma_* v_e \rangle_j V \quad (3.23)$$

Where  $\sigma_i^+$ ,  $\sigma_i^{++}$ ,  $\sigma_i^*$  are the first ionization, second ionization and excitation cross section of Xenon, respectively [12].  $V$  is the plasma volume,  $f_c$  is the confinement factor defined as the ion current that reaches the wall divided by the Bohm current,  $v_e$  is the electron velocity,  $v_a$  is the ion acoustic velocity given by  $v_a = \sqrt{kT_e/M}$ .

The electron temperature in (3.18) is found by equating (3.7) as follows:

$$\frac{n_i}{2} e \sqrt{\frac{kT_e}{M}} (A_w f_c + A_s) = n_o n_e e \langle \sigma_i^+ v_e \rangle V + n_e^2 e \langle \sigma_i^{++} v_e \rangle V \quad (3.24)$$

The solution to (3.24) for the electron temperature is then found by iteration of this equation in the form of

$$\frac{2n_o V}{(A_w f_c + A_s)} = \frac{\sqrt{\frac{kT_e}{M}}}{\langle \sigma_i^+ v_e \rangle + \frac{n_e}{n_o} \langle \sigma_i^{++} v_e \rangle} \quad (3.25)$$

The Bohm current [35] is simply

$$I_{Bohm} = \frac{1}{2} n_i v_a e A \quad (3.26)$$

Where  $A$  denotes the loss area,  $A_s$  and  $A_w$  denotes the loss at the grid area and wall area, respectively. Since plasma in these thrusters is usually less than 10% ionized,  $\frac{n_e}{n_o}$  is small, and the reaction rate for double ionization is less than that for single ionization, the electron temperature is primarily determined by the single ion production rate. The denominator of the right-hand side

has terms that depend on  $T_e$ , and the left-hand side depends only on the geometry and neutral gas pressure in the discharge chamber.

### 3.7.2 Electromagnetic model

The plasma is represented by a uniform, complex permittivity  $\epsilon_p$ , generated and contained in a dielectric tube of inner radius  $r_0$ , outer radius  $r_c$  and length  $l \gg r_0$ , which is shown in Figure 2.3. The tube is surrounded by a coil having  $N$  turns uniformly distributed, in which an RF sinusoidal current flows. In typical RF thrusters, this frequency is on order of 1 MHz. The ions can be considered stationary on the magnetic field cycle time due to the ion acoustic speed at  $T_e = 5 \text{ eV}$  is 1.9 km/s, thus, in a  $1 \mu\text{s}$  cycle, these ions can only move less than 2 mm. On the other hand, the electrons are certainly not stationary in the RF period, but the ion space charge will hold the electrons in place during a cycle time. Therefore, the ac magnetic field from the RF coil can provide confinement of the plasma leads to reduce the ion flux to the discharge chamber walls. Since the walls are floating, this also reduces the ambipolar electron flow to the wall and further reduces the power loss. The induced electric field is azimuthal, while the induced magnetic field is axial. At high plasma density, both fields decay with the skin depth  $\delta$ . Figure 3.13 shows how the skin depth depends on frequency.

$$\delta = \frac{1}{k_i} = \frac{\sqrt{2}c}{\omega} \left( \left[ \left( 1 - \frac{\omega_{pe}^2}{\omega^2 + R_m^2} \right)^2 + \left( \frac{\omega_{pe}^2 R_m}{\omega^2 + R_m^2} \right)^2 \right]^{0.5} - \left( 1 - \frac{\omega_{pe}^2}{\omega^2 + R_m^2} \right) \right)^{-0.5} \quad (3.27)$$

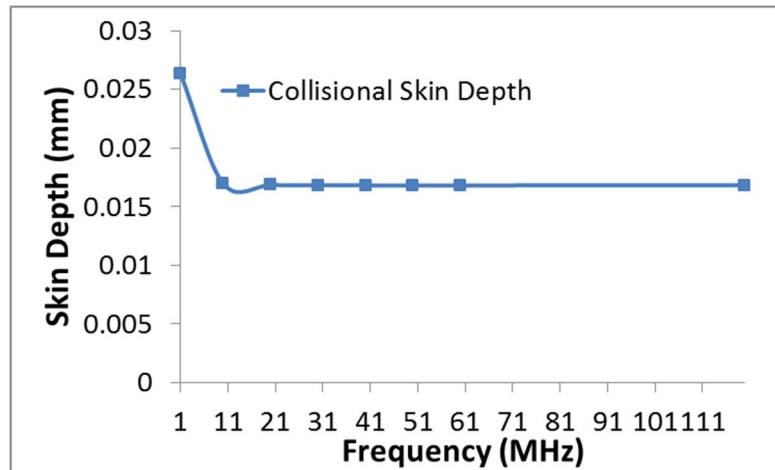


**Fig. 3.13** Expression for collisional skin depth. Skin depth is almost constant over about 11 MHz

The magnetic field induced by the RF coil depends on the coil size and amount of power from RF generator and matching network. For the simplest case, assume that the RF coil forms a solenoid and that the magnetic field inside a solenoid is.

$$B[G] = 10^4 \mu_0 NI \quad (3.28)$$

Where  $\mu_0$  is the permeability of free space  $\mu_0 = 4\pi \times 10^{-7}$  H/m. N is the number of turns per meter, and I is the coil current in Amperes. The figure 3.14 shows the effect of chamber configuration on the magnetic field. A copper coil AWG 12, 30 mm in length of coil, the number of turns is 15 was applied to the model. From the figure 3.14, the conical chamber has stronger field than cylindrical chamber. The field has well-shape in the conical chamber.

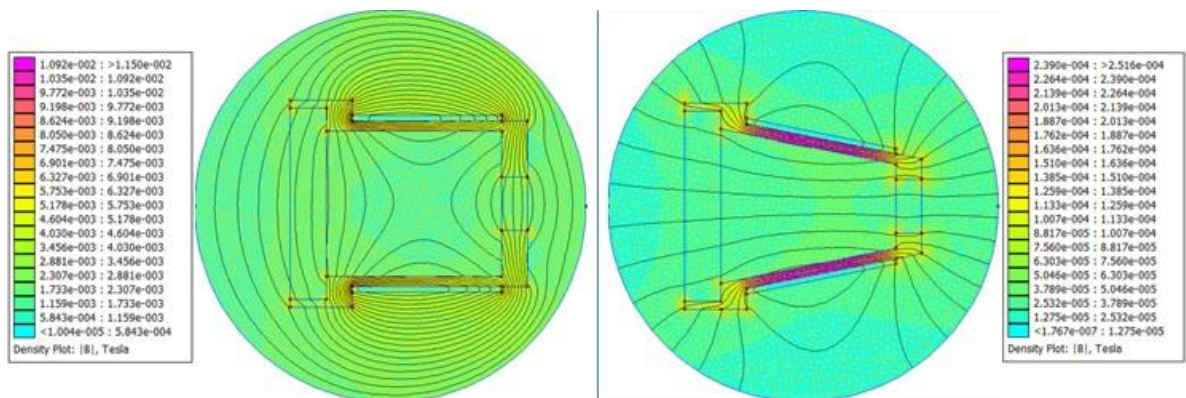


**Fig. 3.14** *Effect of the discharge chamber configuration on the magnetic field (FEMM)*

The electron Lamor radius in this field for a 4 eV temperature is  $\sim 5$  mm, so the electrons are magnetized in the radial direction. This field strength is then sufficient to affect the radial electron motion, which in turn reduces the ion loss to the discharge chamber wall. The flow of ions and electrons across this axial magnetic field is ambipolar. To evaluate the ion loss across the magnetic field to the wall, compared to the flow of those ions along the field to the grids, the ion velocities in the radial direction are evaluated. The steady-state transverse electron equation of motion, including electron-neutral and electron-ion collisions, is given by

$$\begin{aligned} & mn \left( \frac{dv_e}{dt} + (v_e \otimes \nabla) v_e \right) \\ & = -en(E + v_e \times B) - kT\nabla n - mnv_{en}(v_e - v_0) - mn(v_e - v_i) = 0 \end{aligned} \quad (3.29)$$

Where  $v_0$  is the neutral velocity. This equation must be separated into the two transverse velocity components

$$v_x + \mu_e E + \frac{e}{mv_e} v_y B + \frac{kT}{mv_e} \frac{\nabla n}{n} - \frac{v_{ei}}{v_e} v_i = 0 \quad (3.30)$$

$$v_y + \mu_e E - \frac{e}{mv_e} v_x B + \frac{kT}{mv_e} \frac{\nabla n}{n} - \frac{v_{ei}}{v_e} v_i = 0 \quad (3.31)$$

Where  $v_e = v_{en} + v_{ei}$  and  $\mu_e = e/mv_e$  and  $v_0 \ll v_e$ . Solving for  $v_y$  and eliminating the  $E \otimes B$  and diamagnetic drift terms in the  $v_x$  direction, the transverse electron velocity is given by

$$v_e(1 + \mu_e^2 B^2) = \mu_e \left( E + \frac{kT}{e} \frac{\nabla n}{n} \right) + \frac{v_{ei}}{v_e} v_i \quad (3.32)$$

Assuming ambipolar diffusion, we equate the electron and ion transverse velocities to give

$$v_i = \frac{\mu_e}{\left(1 + \mu_e^2 B^2 - \frac{v_{ei}}{v_e}\right)} \left( E + \frac{kT}{e} \frac{\nabla n}{n} \right) \quad (3.33)$$

In this equation, the last term with the density gradient term  $\frac{\nabla n}{n} \approx l$ , is the radial diffusion length in the magnetic field. In RF-induction thrusters, this can be taken to first order as the radius of the discharge chamber. Depending on the strength of the magnetic field, which determines the transverse electron mobility, an electric field  $E$  is set up radially in the plasma to maintain the ambipolar flow. The ions fall through the potential difference set up by this electric field, which means that the ions are accelerated to an energy given by

$$\frac{1}{2} M v_i^2 = e E l \quad (3.34)$$

The transverse magnetic field and ambipolar flow set the electric field magnitude in the presheath region to reduce the acceleration of the ions toward the wall to maintain ambipolarity. However, in the limit of no magnetic field, the electric field must accelerate the ions only to the Bohm velocity [35], which results in a net electric field in the plasma edge region limited to

$$E = -\frac{1}{el} M v_i^2 \quad (3.35)$$

Note that the electric field sign must be negative for the ion flow in this region. The minimum magnetic field from (3.33) to produce an ion velocity of  $v_i$  is

$$B = \frac{v_e m}{el} \sqrt{\frac{e}{m v_e v_i} \left( \frac{T_e}{l} - \frac{m v_i^2}{el} \right) - \left( \frac{v}{1+v} \right)} \quad (3.36)$$

Where  $v = v_{en}/v_{ei}$ , and  $\nabla p/en = \nabla(nkT_e)/en$  is approximately  $T_e/l$  for  $l$  representing the length that ions travel radially across the axial magnetic field. Alternatively, the modified electric

field given (3.35) can be inserted into (3.33) to produce an expression for the transverse ambipolar ion velocity

$$v_i^2 + \frac{el}{M\mu_e} \left(1 + \mu_e^2 B^2 - \frac{v_{ei}}{v_e}\right) v_i - \frac{eT_e}{M} = 0 \quad (3.37)$$

This quadratic equation can be easily solved to give the transverse ion velocity to the wall

$$v_i = \frac{1}{2} \sqrt{\left[ \frac{el}{M\mu_e} \left(1 + \mu_e^2 B^2 - \frac{v_{ei}}{v_e}\right) \right]^2 + \frac{4kT_e}{M} - \left[ \frac{el}{2M\mu_e} \left(1 + \mu_e^2 B^2 - \frac{v_{ei}}{v_e}\right) \right]} \quad (3.38)$$

The parameters in the term  $v_e = v_{en} + v_{ei}$  and  $v = v_{en}/v_{ei}$  are given in SI units [37] for xenon as

$$v_{en} = \sigma \sqrt{\frac{8eT_e}{\pi m}}$$

$$\sigma = 6.6 \times 10^{-19} \left( \frac{T_e}{4} - 0.1 / \left(1 + \frac{T_e}{4}\right)^{1.6} \right) \quad (3.39)$$

$$v_{ei} = 2.9 \times 10^{-12} \frac{n_e \ln \Lambda}{T_e^{1.5}}$$

$$\ln \Lambda = 23 - 0.5 \ln \left( \frac{10^{-6} n_e}{T_e^3} \right)$$

Where  $\ln \Lambda$  is the Coulomb Logarithm. The ion current to the wall is then reduced compared to the normal Bohm current evaluated for an unconfined plasma flowing from the center of the discharge chamber. This reduction in ion current to the wall will be described by an ion confinement factor  $f_c$ . It is simple matter to calculate the reduction in the expected flux of ions going to the wall due to the reduction in the radial Bohm velocity at a given magnetic field strength

B. In this case, ions that would have been lost to the walls end up going to the grids because the axial presheath potential generated by ion flow toward the grids drives the axial ion velocity in the plasma that exceeds the radial ion velocity.

As an example, the ESA XX thruster has a 360 mm grid diameter, 260 discharge chamber diameter, an 100 mm deep cylindrical ceramic discharge chamber, and a grid transparency of 85%, produces 2.7 A of beam current in xenon. Figure 3.15 shows the calculated discharge loss as a function of the mass utilization efficiency. Assuming no applied magnetic field, therefore no plasma confinement ( $f_c = 1$ ) in the discharge chamber. A discharge loss of about 500 eV/ion is predicted at 90% mass utilization efficiency. This is very high discharge loss compared to that found in the literature for RF-induction thrusters of this size. The reason for this is the energy loss which results from the ion and electron flow to the floating potential walls. On the other hand, the discharge loss is 290 eV/ions at 90% mass utilization efficiency if  $B = 12.5$  G is induced in the chamber.

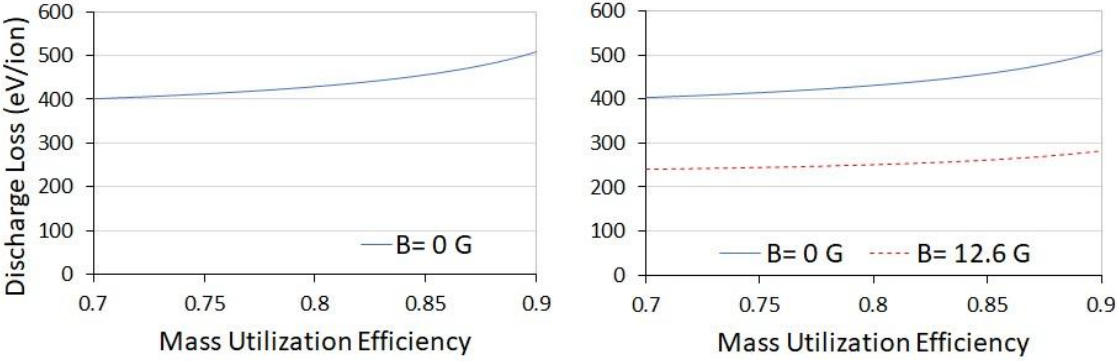


**Fig. 3.15** Discharge loss versus mass utilization efficiency for the different values of the non-induced and induced magnetic field in the discharge chamber

**3.7.3 Energy consumption by plasma discharge chamber**

Now the amount of power which is necessary for producing of desirable ion current can be calculated with easiness, or rather that, ionization cost is described by below.

$$P_{\text{ion\_cost}} = P_{\text{ion}}^+ + P_{\text{ion}}^{++} = (\langle \sigma_i^+ v_p \rangle U^+ + \langle \sigma_i^{++} v_p \rangle U^{++}) \quad (3.26)$$

And the excitation loss as follows

$$P_{\text{exc}} = \langle \sigma_* v_e \rangle U^* \quad (3.27)$$

The ion loss and electron loss result from the ion and electron flow to the floating-potential walls. The power losses were caused by ion and electron as follows

$$P_{\text{ion\_loss}} = (I_{\text{scr}} + I_w + I_b)(0.5T_e + \phi) \quad (3.28)$$

$$P_{\text{electron\_loss}} = I_a(2T_e + \phi) \quad (3.29)$$

Substituted equation (3.26 - 3.29) into equation (3.17), and then simplifying the equation (3.14) the discharge loss is

$$\begin{aligned} \eta_{\text{d\_loss}} = & \frac{2n_0V}{\sqrt{\frac{kT_e}{M}} A_{\text{scr}} T_s} (\langle \sigma_i^+ v_p \rangle U^+ + \langle \sigma_i^{++} v_p \rangle U^{++}) \\ & + \left[ \frac{(1 - T_{\text{eff}})}{2} + \frac{A_w f_c}{A_{\text{scr}} T_s} + 1 \right] (2.5T_e + 2\phi) \end{aligned} \quad (3.30)$$

### 3.8 Results and comparison with experiments

Figure 3.16 shows the solution curves with various physical models for ESA XX RF ion thruster with the beam currents of 1.45 A and compares with reference experimental result (diamond, [34]) and recent analytical modeling result (dashed curve, [33]). The size of ESA XX thruster is 26 cm in diameter and its power is 6.2 kW producing thrust of 200mN. The most significant effect is produced by the calculation of confinement factor obtained from induced B-field which can be observed from the shift from double dot-dashed curve to dot-dashed curve. When the Clausing factor is changed from a fixed value (dot-dashed curve) to variable values (dotted curve), the result became closer to the experiment especially at lower flow rates. When the secondary electron emission is added (solid curve), the result mostly lies on the experiment values except at lower flow rates. It is clear that the result from our analytical model which additionally considers various physical phenomena produces a better prediction of the thruster performance. It

is presumed that the reason for the errors at lower flow rate is due to a poor prediction of discharge losses.

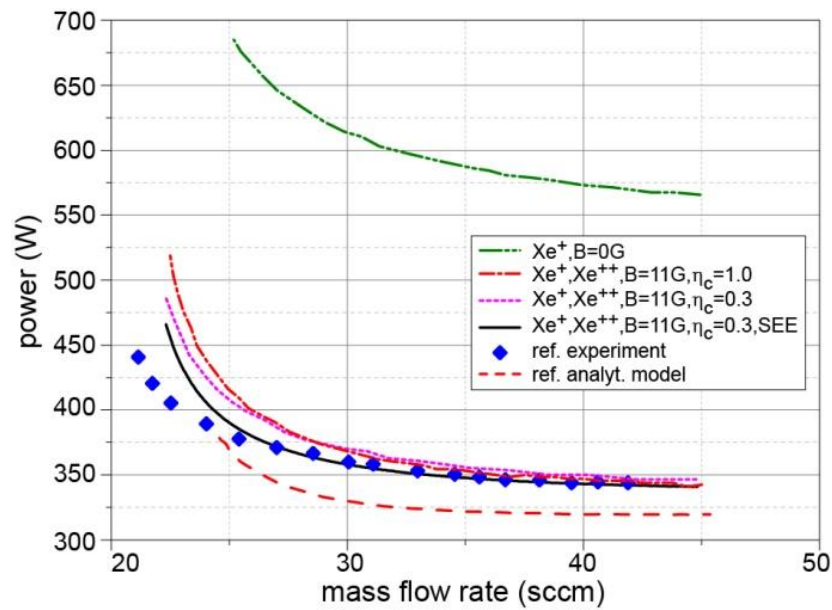


**Fig. 3.16** Comparison of the calculations obtained from the models with various effects.

Figure 3.17 provides various loss components in the discharge over various mass flow rates.

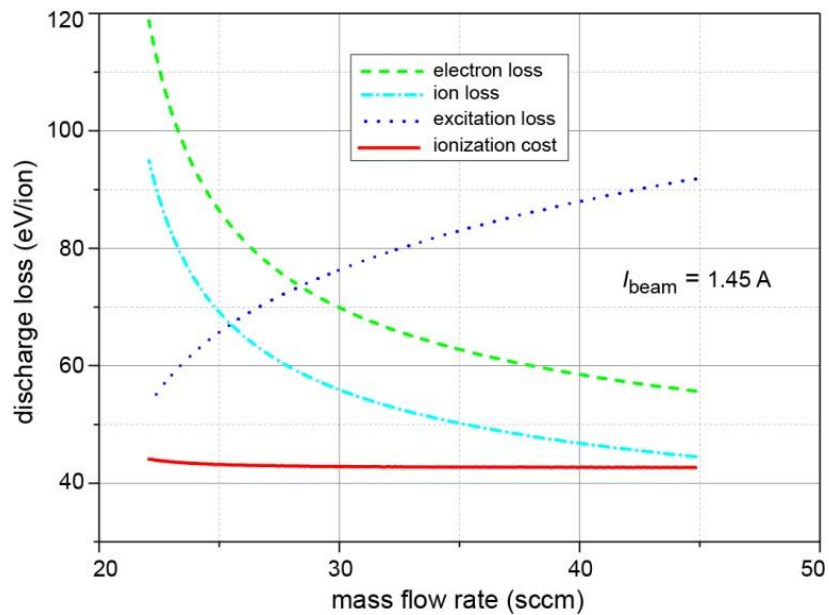
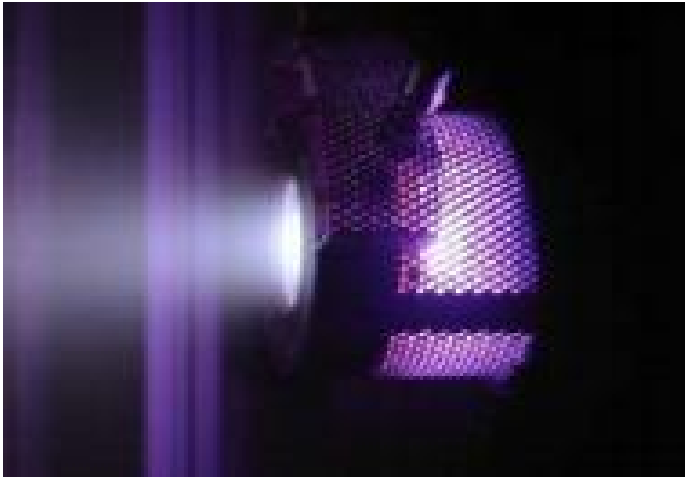


**Fig. 3.17** The ion production cost channels map of the ESA-XX RF ion thruster obtained by our analytical model at  $I_b=1.45 A$

The calculation was conducted for the same case as in Fig. 3.16. In the RF Ion Thruster with dielectric walls, when the plasma is sustained by a combination of volume ionization and surface loss, the power loss due to electron and ion currents flowing along the radial magnetic field through the RF sheath to the wall and the screen grid shows the most significant power loss. On the other hand, the density structure of the plasma shows barely any temporal modulation. The electron loss is much more than ion loss, excitation loss and ionization cost. This is because the density profile of the ions in the sheath remain steady and the electrons are much more mobile. They are able to respond virtually instantaneously, thereby changing the spatial extent of sheaths and quasi-neutral plasmas. For the uniform plasma inside the discharge chamber, the total ion loss area is  $A_t = A_g + f_c * A_w + A_{bw}$ , where  $A_g$ ,  $A_w$  and  $A_{bw}$  are the opening area of the grid system, side wall area and back wall area, respectively.  $f_c$  is the Bohm current reduction factor to the wall due to an AC magnetic field generated by the RF current flowing in the coil with a frequency at the RF oscillator frequency. Then, the power loss to the wall can be estimated from the sheath potentials in the plasma edge. As shown in the figure, the charge losses exponentially drop and the excitation loss increases as the flow rate increases. As flow rate increases, large portion of energy goes into the excitation of neutral gas. However at lower flow rates, charge losses become significant because of increased sheath potential and electron temperature. This results in higher ionization cost which demands significantly higher discharge power as shown in Fig. 3.16. In scaled-down RF ion thrusters, the losses will increase because of a higher area-to-volume ratio and reduced confinement factor. However the excitation loss becomes significantly smaller than other losses as the size of the RF ion engine becomes smaller.

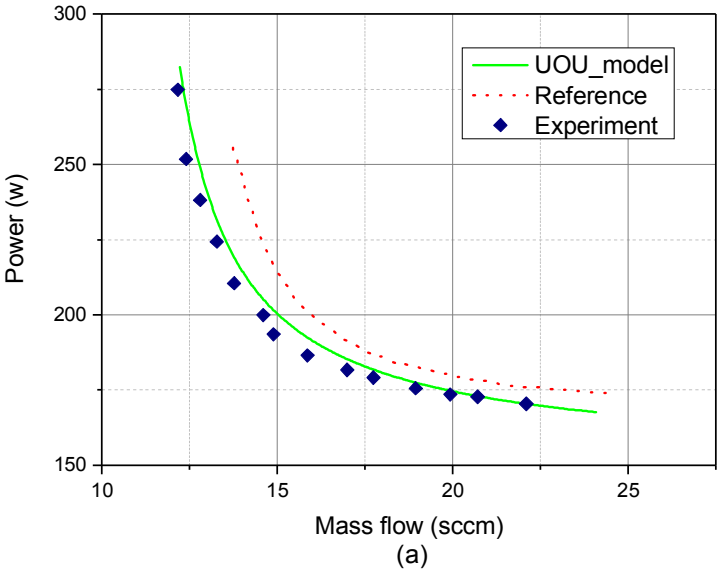
Figure 3.19 shows the discharge power curves for ESA XX RF ion thruster with the beam currents of 780 mA , 2700 mA. Diamond curve corresponds to the experiment data [34], and solid and dotted curves correspond to the calculation of our analytical model and the calculation result from the Ref. [33], respectively. Overall trend is the same as shown in Fig. 2 which is for high

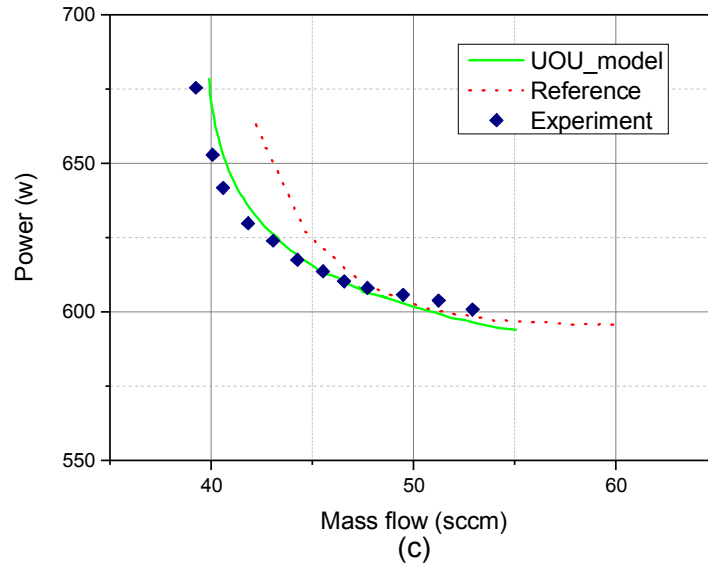
beam current case. However our calculation provides a better agreement with experiment than high beam current case even at lower flow rates. The calculation result presented in Fig. 3.17 and 3.19 confirms that our analytical model is reasonable to use for predicting the performance of large size RF ion thrusters over various power ranges.



**Fig. 3.18** Miniaturized RIT-4 ion engine from Giessen University

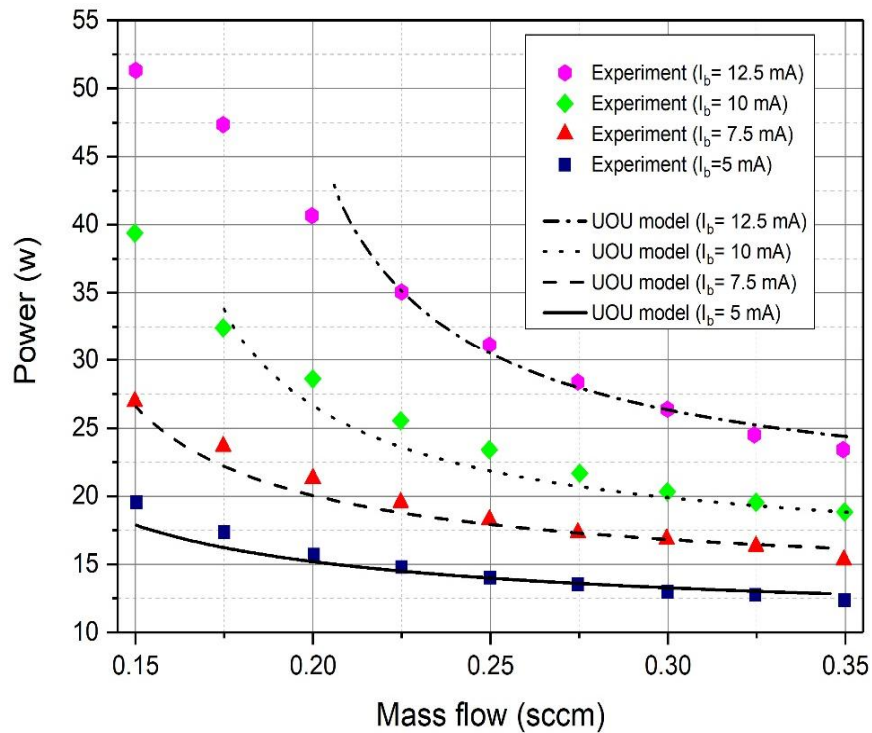
It is likely that any analytical modeling result obtained for a large scale thrusters may not simply be applicable for a small scale thrusters. Our analytical model was also validated for small scale RF ion thrusters and compared with experiment result.





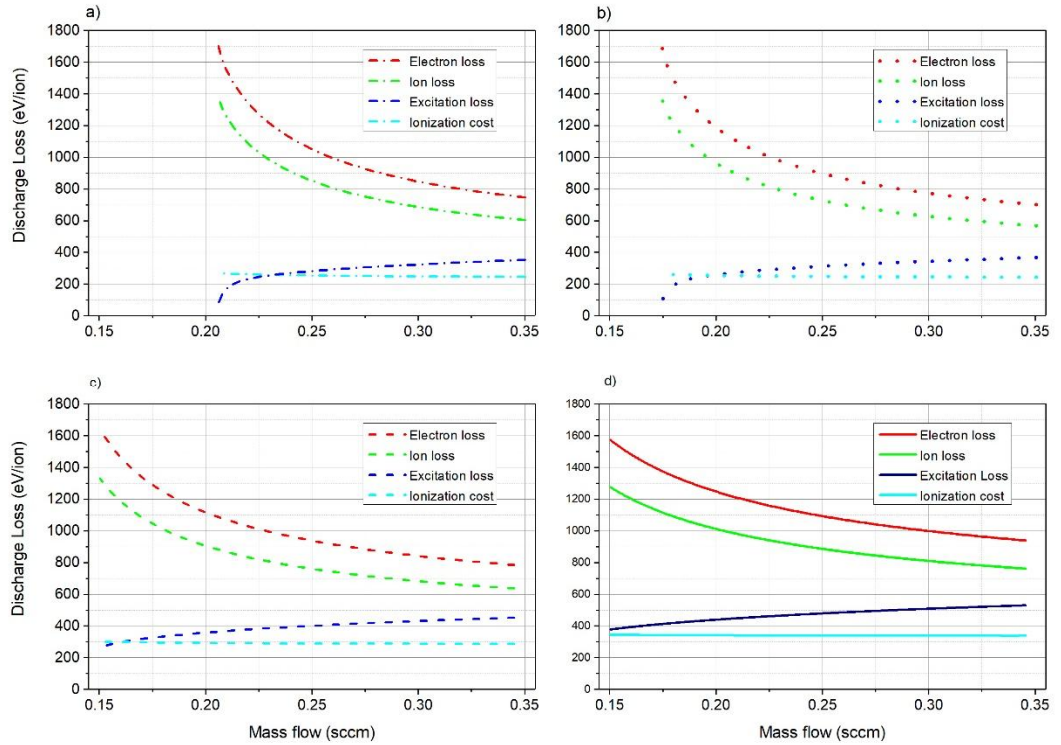
**Fig. 3.19** Experimentally and analytical obtained discharge power of the ESA-XX ion thruster in operation with ion beam currents are 780 mA (a) and 2700 mA (c).

Figure 3.20 shows the power requirement for various beam currents over ranges of mass flow rates. Our calculation result was compared with experiment data of small scale RIM-4 ion thruster whose diameter is 4 cm with spherical discharge chamber which is shown in figure 3.20. The comparison result in Fig. 3.18 shows that our analytical model also produces a good agreement with experiment [38] even in small scale micro thrusters. At low flow rates, however, the deviation from experiment becomes larger for each beam current. This is mainly because the error in loss terms especially the excitation loss calculated from the cross-section data becomes significant. In addition, the eddy current that causes the RF power loss on the screen grid is not considered in our model and the non-uniform neutral density distribution causes incorrect estimation of wall-directed flux.



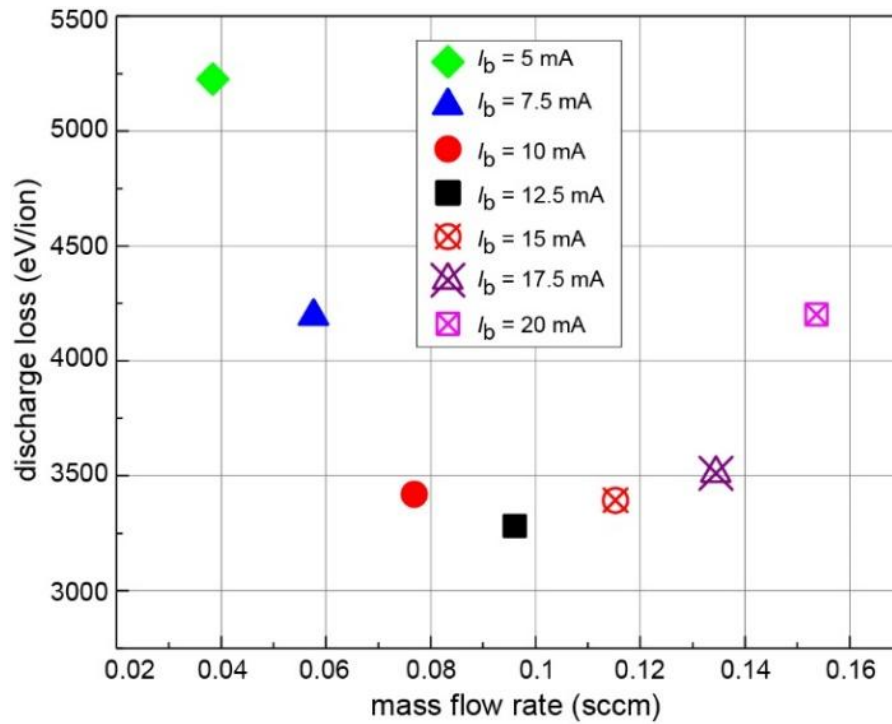
**Fig. 3.20** Comparisons of the our simulation and experimental data at  $V_{scr} = 1250 V$  and  $V_{dec} = 150 V$  for the performance of the RIM-4 ion thruster. With 2.5 MHz RF source losses at different ion beam current values. Our model shows a good agreement to the experimental data for RIM-4 ion thruster tested at Physikalisches Institut in Justus-Liebig-Universität Gießen.).

At the higher ion beam current, the power loss increases significantly. The reason for this loss increment is shown in Figure 3.21, which plots the four energy loss channels for this small scale RF thruster at different in ion beam currents. The electron and ion energy loss fractions each dropped by about 60 eV/ion due to the went up ion and electron losses to the wall that increased the required electron temperature and wall-sheath voltage.



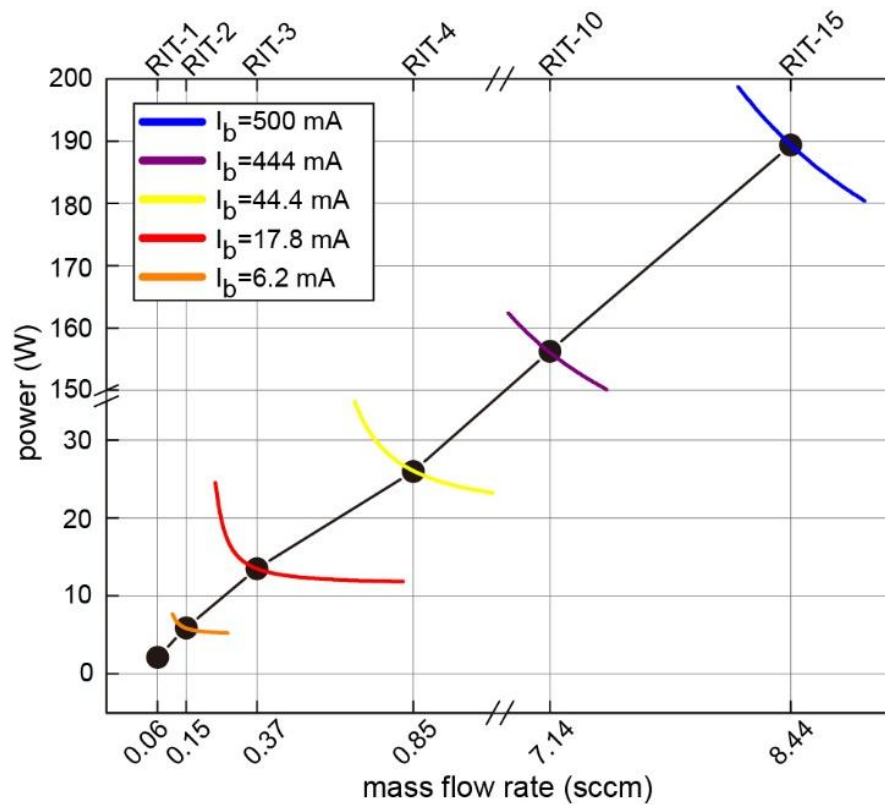
**Fig. 3.21** Comparisons of our simulation and experimental data at  $V_{scr} = 1250\text{ V}$  and  $V_{dec} = 150\text{ V}$  for the performance of the RIM-4 ion thruster. With 2.5 MHz RF source losses at different ion beam current values. Our model shows a good agreement to the experimental data for RIM-4 ion thruster tested at Physikalisches Institut in Justus-Liebig-Universität Gießen.).

Figure 3.22 shows the discharge loss calculated for RIM-4 RF ion thruster at fixed mass utilization efficiency of 90% for various ion beam currents while other factors are kept constant. For a given beam current, a mass flow rate that produces a specific mass utilization efficiency can be determined. Unlike the previous curves where the discharge loss decreases as mass flow increases, when the mass utilization efficiency is considered, there exists an optimal mass flow rate which produces a minimum discharge loss. For RIM-4 RF ion thruster, the minimum loss occurs at beam current of 12.5 mA for 90 % mass utilization efficiency. Similar behavior was also observed for larger scale RF ion thruster.



**Fig. 3.22** Discharge loss calculated for RIM-4 RF ion thruster at a fixed mass utilization efficiency of 90 % for various ion beam currents.

Figure 3.23 shows performance map calculated for a family of micro-scale RF ion thrusters of RIT-1, RIT-2, RIT-3, RIT-4, RIT-10 and RIT-15 and compared with the measurement points (dot points) which were obtained from Ref.[39] and [40]. The number given in each thruster's name denotes an approximate beam diameter. The beam currents for each thruster was chosen from the references. It is noted that the performance curves obtained from the calculation intersect with the measurement point. From this results, it can be inferred that our analytical model provides a robust prediction for a wide range of micro RF ion thrusters.



**Fig. 3.23** Performance map of a RIT ion thruster family obtained by the our model and experimental data at various of the ionizer diameter and rf-frequency with different xenon propellant flow rate.

### 3.9 Chapter summary

This chapter has further improved the previously reported analytical models for RF gridded-ion thruster in order to provide a better prediction of performance which can be useful in design phase. Additional features we considered were secondary electrons emission, doubly-charged xenon ions, variable Clausing factor obtained by Monte Carlo calculation, and ion confinement factor generated by the induced electromagnetic field in the discharge chamber. The ion confinement factor had most significant effect on the calculation. The calculation results obtained from our improved analytical model were in a good agreement with the experimental results for both large and small-scale RF ion thruster for various beam currents.

## Chapter 4. iU-50 Ion Thruster Design

Among the various types of plasma thrusters developed over the last few decades for in-space propulsion applications of satellites and spacecraft, Hall effect thrusters and ion engines are the most studied ones. Attitude control and station keeping require ion engine thrust levels of about 1mN. For this reason, the work at Applied Aerospace Research Lab in the University of Ulsan was concentrated on small scale radio frequency ion thrusters in 2017. In this thesis, the design and manufacturing methods of the iU-50 (Radio Frequency ion engine of Ulsan with 50W class) are explained. The iU-50 is an experimental ion thruster and will be tested in the vacuum chamber at AARL lab. The Ion Thruster has a conical discharge chamber having an inner diameter and outer of diameter of 45 mm and 50 mm respectively, with a length of 50mm. A double grid system with 211 holes is implemented. Preliminary calculations suggest that the thruster will generate thrust in the range of 1 - 3 mN. A discussion on material selection and manufacturing methods is presented for the production of the prototype.

### 4.1 Introduction

Since about two decades, electric propulsion (EP) has reached the stage of flight readiness, and several EP-missions demonstrated already its potential. Thus, Ion Thrusters and Hall effect Thrusters were popularly used. These thrusters ionize the propellant gas then eject these ions after accelerating them by the electrostatic force to generate thrust. The advantage of plasma thrusters is that the average exhaust velocity of the particles being thrown out of these thrusters is much greater than chemical thrusters, meaning that their specific impulse (Isp), ~1750 seconds for Hall Thrusters and >3000 seconds for ion thrusters, is much higher compared to the Isp of chemical thrusters, <450 seconds [13].

There are three main types of ion engine, differentiated by the main mechanism for ionization of the propellant gas. The first type is called the electron-bombardment ion engine (or Kaufman type ion engine). In this type of ion engines, an internal cathode provides the electrons for the ionization of the propellant. In the second kind, called Radio-Frequency (RF) ion thrusters, the propellant gas is ionized by the rf energy generated by a low frequency rf voltage supplied to an antenna. This can be achieved by wrapping a chamber containing the propellant gas, with a rf coil. In the third kind, called microwave ion engine, a microwave antenna is used to deliver microwaves into the discharge chamber that are used for the ionization of the propellant gas. Three facts forced the development of ion thrusters:

1. The transportation of communication satellites into a synchronous orbit
2. The exploration of the sun and the planets by scientific probes
3. The attitude control, station keeping, and drag compensation of spacecrafts.

## **4.2 Radio frequency technology thruster design**

The new AARL effort will benefit from the fact that among the class of gas-discharge small scale ion thruster, the rf-type seems to be most favorable because the RF ionization has some inherent properties which make the technology attractive for ion thruster application:

1. The discharge is self-sustaining and electrodeless. Therefore, an RF ion thruster does not need a main cathode like Kaufman or Hall effect Thrusters. So one omits the lifetime limitation of this part as well as the limitation of the thruster discharge power caused by a maximum cathode. Moreover, the electric design of an RF thruster is easier and safer, because the discharge power supply is not coupled to the high voltage plasma potential. The RF generator remains completely on satellite ground potential.

2. The beam current is easy and quick to control by variation of RF power. Only this parameter must be controlled. A linear relation between RF power and beam over a wide range of current allows an effective and simple beam current control mechanism.
3. Compared to HET engines gridded ion engines offer very low beam current divergence angle.

Another advantage of the RF discharge with inductive coupling is the high electron temperature  $T_e$  near the discharge vessel walls being the consequence of the induction law. From figure 4.1, the induced electrical field strength  $E_{ind}(r)$ . Together with the plasma density  $n$ , which decreases towards the walls due to the ambipolar diffusion, the extractable ion current profile  $j_i(r) \sim n\sqrt{T_e}$  is rather flat. This enable to drill the beamlet holes in the grid system close to the ionizer walls.

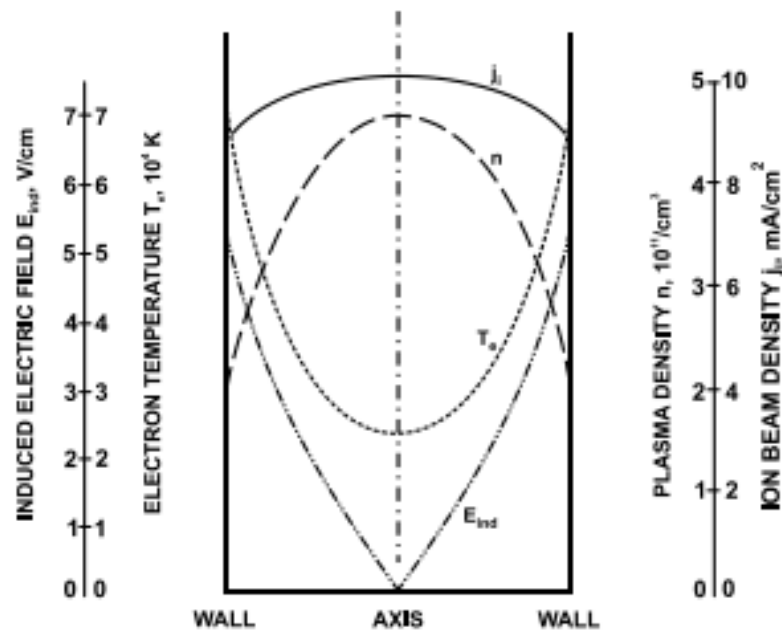


**Fig. 4.1** Experimental discharge parameters of a 10-cm rf-ion source in their radial variation. The  $n$  and  $T_e$  data have been obtained by double Langmuir probes averaged over many test runs [41].

### 4.3 iU-50 Thruster design and components

In the preliminary designs of the iU-50 thruster, the proposed thruster has a 50 mm diameter discharge chamber, and double grid design consisting of 211 apertures. The 3D CAD models are generated in SOLID and CATIA. The very first generated design of the iU-50 thruster is shown in figure 4.2. The optimized design of the iU-50 is shown in figure 4.3.

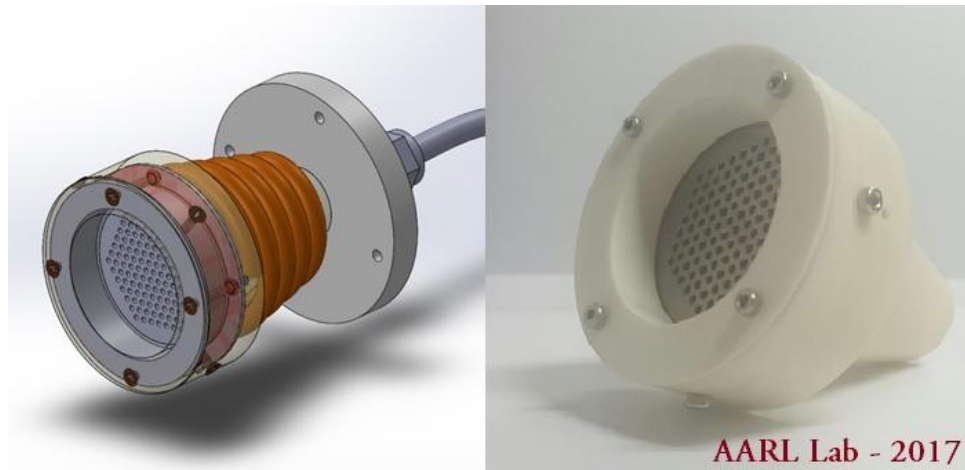


**Fig. 4.2** *The first version iU-50 Ion Thruster (Ulsan – 2017)*

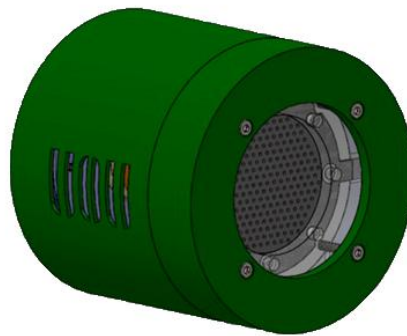


**Fig. 4.3** *The optimized version iU-50 Ion Thruster (Ulsan – 2017)*

In the course of development, the following parameters had to be investigated:

1. The length of the discharge vessel and the induction coil.
2. The discharge pressure.
3. The RF transmitter frequency.

4. The discharge chamber material.
5. The grids system
6. The covering of iU-50 ion thruster
7. The gas injector and gas controller system

### 4.3.1 Main ionization chamber

The discharge chamber of an RF Ion Thruster is where the plasma is generated. The chamber is axisymmetric; it can be cylindrical, conical or even hemispherical. In this thesis, iU-50 ion thruster uses conical shape discharge chamber because the conical shape decreases the wall area and reduces the ion loss area for a given thruster length. Figure 4.4 shows the 260 mm thruster discharge loss versus mass utilization efficiency predicted by the 0-D analytical discharge model for same lengths of the conical and cylindrical discharge chamber. We see that the discharge loss is significantly larger than predicted for conical chamber for cylindrical chamber.

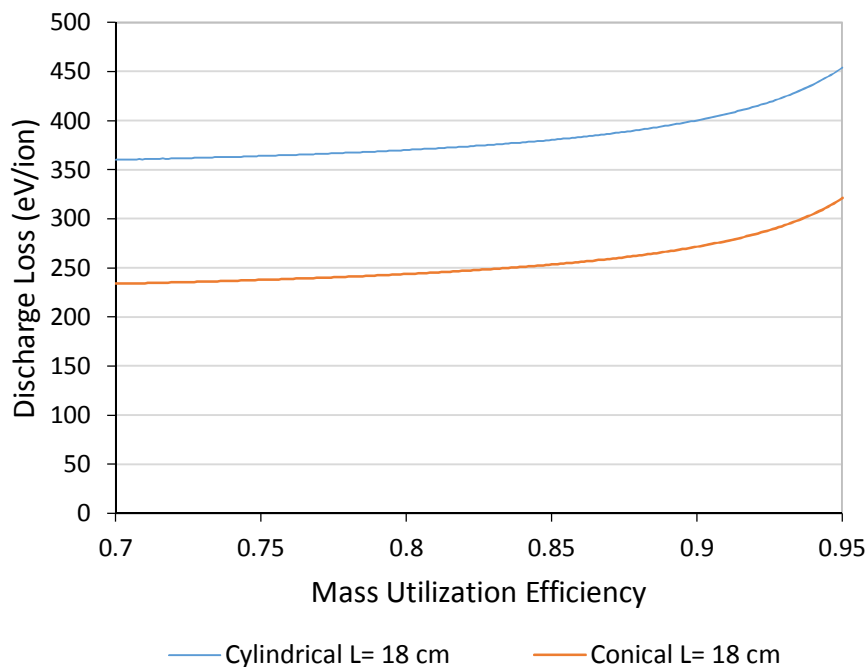


**Fig. 4.4** Discharge loss for the reference RF ion thruster with conical and cylindrical vessel

This is indicative of the increased plasma loss area associated with both the cylindrical wall and the axial end plate compared to the conical design. The induced electric field  $E_{ind}$ , as shown in figure 4.1, is not strong enough to accelerate the discharge electrons during a single half RF period up to energies which enable them to ionize. However, if electrons suffer elastic collisions with 180 degree turns just when the electric field direction reverses, an energy accumulation takes place. The related statistics can be affected in a favorable manner if the discharge vessel radius  $R$ , the discharge pressure or the mean free flight-time  $\tau \sim 1/p$ , and the frequency  $\nu$  are coupled to each other by the relation:

$$p \sim \nu \sim 1/R \quad (4.1)$$

This scaling law has the consequence that both the pressure and the frequency should be increased when scaling-down the ionizer in order to keep optimum plasma condition [41]. Concerning the optimum radio frequency  $\nu_{optimum}$ , however, additional aspects play a role like matching conditions of the power of the RF generator, eddy currents in the structural parts of the thruster, and RF radiation losses.

Another parameter to be optimized is the discharge vessel length. Extended experiments with different sized RF ionizers and different working gases yield for Xenon the empirical relation [42]:

$$l_{optimum} \sim (2R)^{0.66} + d \quad (4.2)$$

Where  $d$  is the thickness of the gas distributor and grid, the system which intrude into the ionizer cylinder. This means that  $l_{optimum} - d$  is the effective length of the plasma column. From equation 4.2, we have to consider more whether, the discharge chamber should be made as long as possible to keep the neutral propellant long enough in the plasma volume to be ionized. This assumption is supported by the fact that the exponent of equation 4.2,  $l_{optimum}$  increases with

decreasing atomic weight of the propellant. In contrast, the discharge chamber length should be as short as possible to minimize the plasma losses toward the chamber wall. In addition, a longer conical discharge chamber increases the number of turns of the antenna relative to a shorter cylindrical thruster, which increases both the electric field interaction region in the discharge chamber and the net induced magnetic field from RF-induction coil. This provides advantageous performance for iU-50 ion thruster.

Furthermore, the RF field must penetrate the walls, an isolating material is mandatory for the discharge chamber. Thank for material technology studies, Alumina has been used for this reason because of its good mechanical properties and allow more flexible ionizer design. The geometrical discharge chamber is in table 4.1

**Table 4.1** *Geometrical discharge chamber*

<b>Component</b>	<b>Value</b>
Beam diameter	45 mm
Chamber diameter at grid	50 mm
Length	50 mm
Thickness	3.5 mm
Back diameter	16 mm

### **4.3.2 Gas inlet**

The gas inlet works on the right-hand side of the Paschen curves. It is made by an isolating material to avoid thermal load by currents from the plasma side. It can be easily adapted to different mass flows. The gas will be fed through a 1/8" stainless steel pipe, connected to the isolator through a Swagelok fitting. The flow injector will be manufactured from MACOR, due to MACOR has excellent machinability compared to others ceramics.

### **4.3.3 RF coil**

The copper wire selected for the iU-50 has many different sizes. For the demo version, AWG 12 is used firstly. It is wound directly on the alumina chamber. It has 12 turns over 36 mm. A MACOR apparatus will be fit between the alumina chamber and the aluminum strut to stabilize the RF coil. An RF frequency of 13.56 MHz is proposed due to the availability of the equipment.

### **4.3.4 Grids system**

A previously RIT thruster pointed out that the comparable poorer performance in terms of ion production costs and power to thrust ratio is mostly caused by the thrusters old fashioned extraction grid system. The first of these problems were the occurrence of inter-grid arcs at the rim of the grid system which led to the formation of molten beads of the material, reducing the gap between the screen and the acceleration grids. The reduction in screen/ accelerator grid gap prevented the thruster operating at higher thrusts. This problem was addressed by increasing the grid separation and making the individual grids of different diameter, thus substantially increasing the breakdown path. This results in appear the arcing phenomenon. The gap of the screen/accelerator grid is optimized by Perveance factor as explained in the previous chapter. The other problem is grid erosion by direction impingement. Normally, the erosion usually appears at the accelerator grid, that increased moving out from the center to the edge of the perforated area. In addition, the operating time of the thruster had been short so that charge exchange erosion would have been negligible and the erosion was, therefore, the result of direct impingement. The other serious problem was primarily caused by the flat-grid-type design. Therefore, using low expansion materials, flat grids were often used for small scale ion thruster.

To reach high performance, grids system requires a screen grid thickness of less than 0.5 mm. To do that the carbon – carbon was used as well as the negative thermal expansion coefficient

some this material, a grid made of this material promises an excellent thermal behavior. Besides, carbon-carbon are offering more interesting more interesting properties: high thermal conductivity, high E-modulus, low sputtering rate, low density.

A double grid system is implemented in order not to complicate the designs with the addition of the triple grid. Ion optics have been studied in previous work [43-45]. The grids are planar molybdenum sheet metal because the cc-composite material is very expensive. They are not dished even though dishing is preferred in order to keep the apertures aligned after thermal expansion occurs in the grids and to preset the direction of possible buckling under thermal expansion [12]. The apertures are circular in shape and are packed in a hexagonal pattern. There is the total of 211 holes. The grids are shown in figure 4.5 and figure 4.6.



**Fig. 4.5** *The grids system for the first version iU-50 thruster*

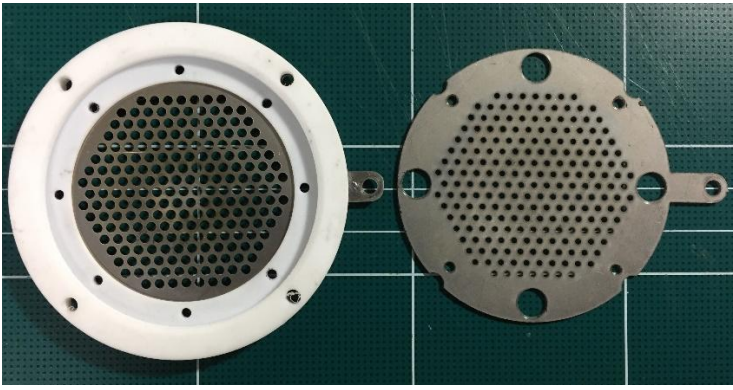


**Fig. 4.6** *The grids system for the second version iU-50 thruster*

The holes in the screen grid are 2 mm in diameter and the grid is 0.5 mm thick. The accelerator grid, on the other hand, is 1 mm thick, with aperture having a diameter of 1.25 mm. The screen/accelerator spacing can change in 0.7 mm, 1 mm and 1.5 mm. The geometrical parameter ion optics is shown in table 4.2.

**Table 4.2** *Geometrical ion optic system*

<b>Component</b>	<b>Value</b>
Number of apertures	211
Screen grid voltage [V]	1500
Accelerator grid voltage [V]	-150
Screen grid hole diameter [mm]	2
Screen grid thickness [mm]	0.5
Accelerator grid hole diameter [mm]	1.25
Accelerator grid thickness [mm]	1
Screen/Accelerator grid gap [mm]	0.7 – 1 – 1.5

The resulting limiting ion beam current density is  $19.25 \text{ mA/cm}^2$  from the Child-Langmuir equation which was explained in the previous chapter. This results in an ion beam current of  $\sim 0.1 \text{ A}$  for the thruster. The screen grid contains arms extending in the horizontal axis and the accel grid has arms extending in the vertical axis. These arms are where alligator clips will be attached to supply the voltage to the grids. The arms are placed on perpendicular axes in order to provide sufficient space to attach the clips. The grids contain 4 large holes. These holes are where the bolts will pass through in order to hold the grids firmly to the alumina chamber. Since the bolts are made of steel, hence conductive, the bolts will pass through Teflon rings in order to prevent contact with the molybdenum grids. Also, larger Teflon rings will be used in between grids in order to provide the spacing between the grids. The results of the 2-Demensional model for ion optics simulation

by coding is shown in the figure 4.7. As we can see from the figure the ion beam is well-focused with parallel trajectory.

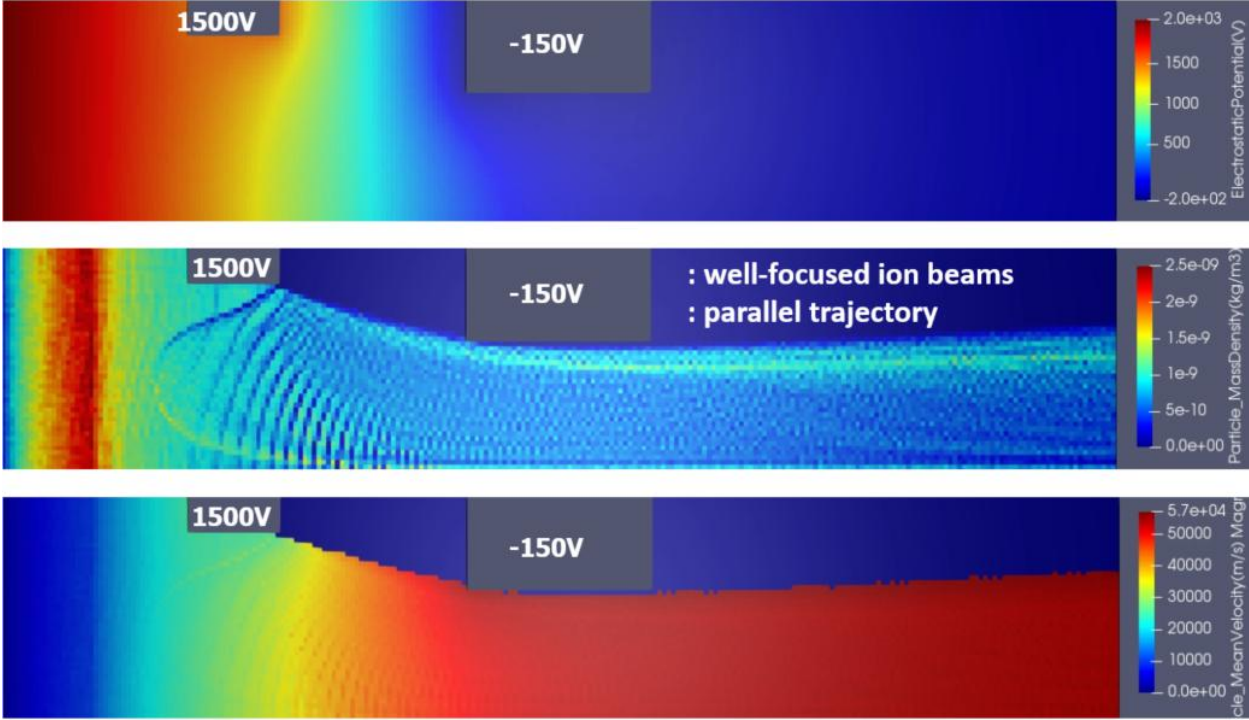
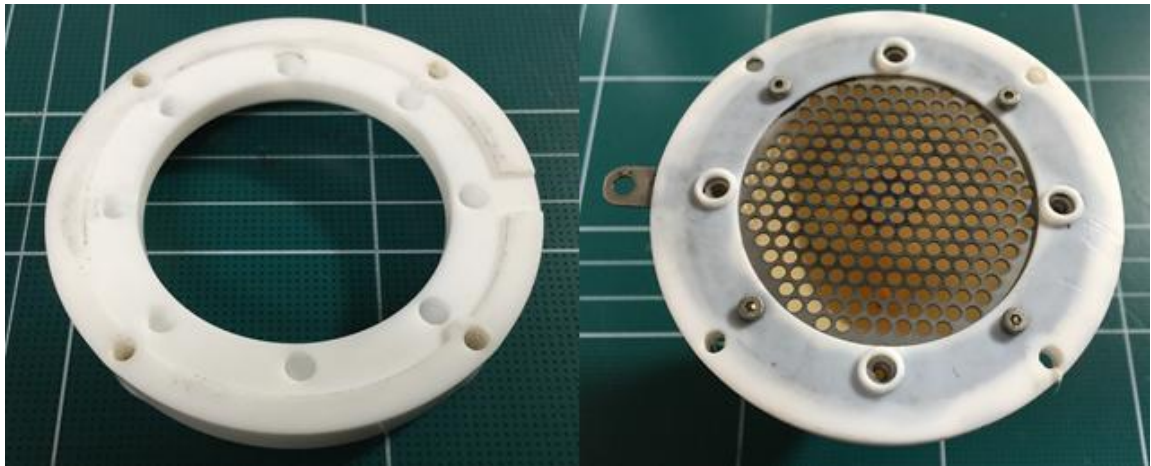


Fig. 4.7 The grids system for the second version iU-50 thruster

### 4.3.5 Grid mounting ring

This is a special feature of the AARL lab prototype: the grid is mounted on a separate ring made of Teflon. This allows a quick and easy change of different grid sets and the distance between screen grid and accelerator grid. In the same way, it is possible to test one mounted grid set on different discharge vessels. Figure 4.8 shows the AARL grid mounting ring which made by Teflon.



**Fig. 4.8** *The grids system for the second version iU-50 thruster*

#### **4.3.6 iU-50 Ion Thruster case**

The thruster case shields the RF field from radiation into the environment and provides the mounting interface inside the vacuum chamber at AARL lab. The advantage of this design is that the plasma is kept inside the electrically isolated discharge vessel and has no contact with the mounting structure. Therefore, the thruster case can be on ground potential without any isolator. The iU-50 thruster, which is made by aluminum, is shown in the figure 4.9.

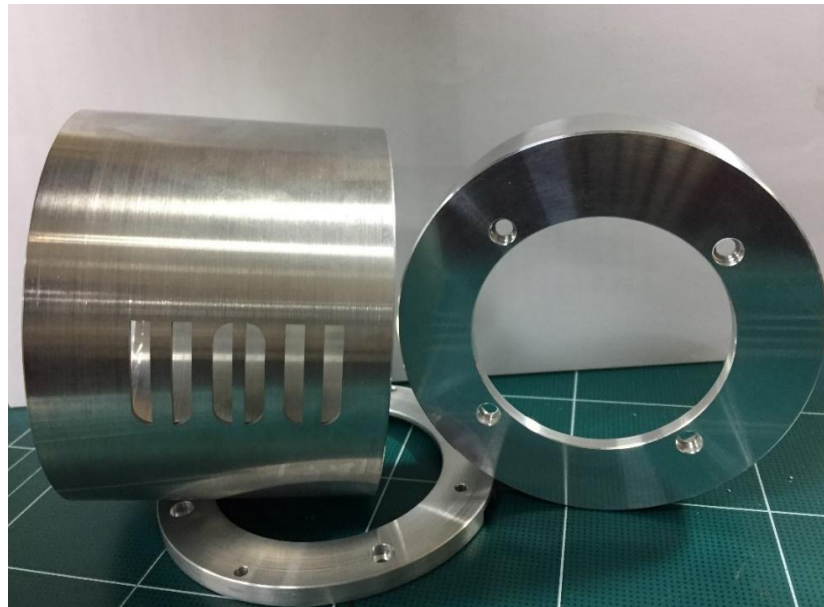


**Fig. 4.9** *The grids system for the second version iU-50 thruster*

### 4.3.7 NU-50 Neutralizer

The Hollow cathode is an indispensable device for iU-50 ion thruster. Hollow cathodes, which are composed of three main components as insert, orifice and keeper, and which work according to a physical process known as thermionic emission, provide the necessary electron current for ionization of neutral propellant atoms and neutralization of the ion beam at the exit for iU-50 ion thruster (Figure 4.10). In addition, hollow cathodes are promising candidates for use in microsattellites and nanosatellites as stand-alone propulsion devices due to their small physical size. In its simplest form, thermionic emission is the release of electrons from an emissive material. It is necessary to heat the emissive material up to a temperature in order to start electron emission. In this study, summary of a comprehensive literature survey about kinds and properties of insert materials and the things considered while using them are shared. The need that the insert material should be heated up to a temperature, keeps hollow cathode from operating quickly. Therefore, the heater used in a hollow cathode and its heating performance is of extreme importance. Moreover, the design process of the hollow cathode that is designed at the University of Ulsan according to the experiences that are obtained from this literature survey and analysis are shared with the research community.

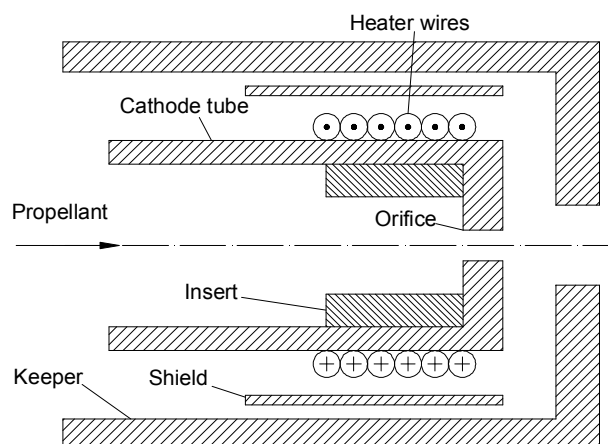


**Fig. 4.10** Schematic of hollow cathode

It is of extreme importance for hollow cathode operation parameters and power consumption whether it is easy to emit electrons from thermionic emitter. Therefore, the insert material should be selected with great care. Work function, evaporation rate and resistance against impurities are important parameters for emitter material selection. The most frequently used emitter materials in the literature are barium oxide impregnated tungsten (BaO – W), lanthanum hexaboride (LaB<sub>6</sub>) or cerium hexaboride (CeB<sub>6</sub>) [Warner, 2008].

After experiences gained by this comprehensive literature survey on emission materials and the analysis of different heater designs, we decided to manufacture a prototype hollow cathode. Electrical connections, thermocouple placements are determined and design mistakes are eliminated with this first prototype made out of brass and design and manufacturing process of the real cathode is started (Figure 4.11).



**Fig. 4.11** *Prototype hollow cathode*

Generally, a hollow cathode is composed of the insert, cathode tube, heater, keeper tube, spring, base parts and other parts (screw, wire etc.). Hollow cathode design starts from the inner part and goes towards the external parts. It is really important for material to be compatible with each other since hollow cathode works at high temperatures. Especially, having a similar thermal

expansion coefficient, high melting point and not reacting with each other are important points that one should keep in mind while selecting the materials used in the hollow cathode design. Insert is located at the center of cathode design. LaB6 is selected as emitter for NU-50 hollow cathode, since it has low evaporation rate and it is not affected by impurities. For a next stage, the power supply for NU-50 neutralizer was built. The hollow cathode circuit is shown in figure 4.12.

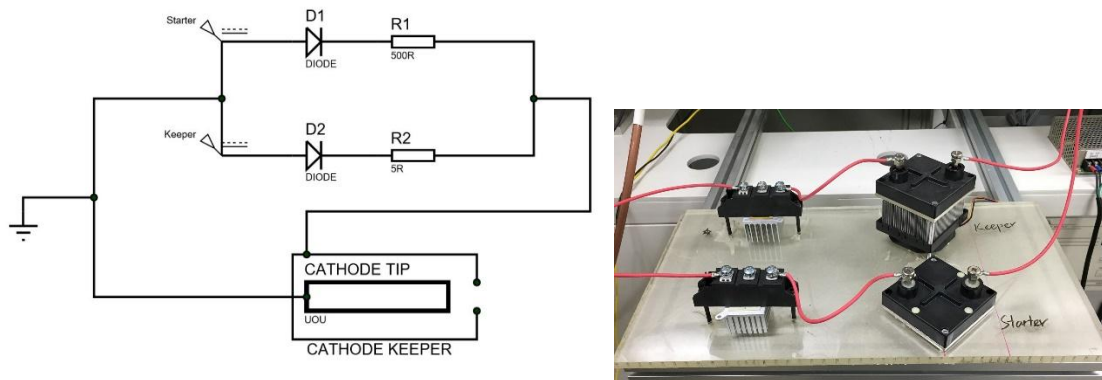


**Fig. 4.12** *Hollow cathode circuit at AARL lab*

## 4.4 Performance prediction of iU-50 ion thruster

### 4.4.1 Power absorbed

The power absorbed increase when scaling down the thruster is based on the increasing ionizer wall surfaces, where the plasma losses occur, relative to the discharge volume  $V$ , where the ions are generated as shows in the figure 4.13.

We use a conventional drain current percentage of 2% of the beam current and an extraction voltage of 1 kV, a negative high voltage of 150 V. The quotient of the beam power over the thruster power input gives the power efficiency  $\eta_e = J(U + V_p)/P$ . The power to thrust  $P/F$  is usually called specific power  $P_{sp}$ .  $\eta_e$  decreases and  $P_{sp}$  increases by scaling down the radio frequency ion thruster, following the increasing ion production costs.

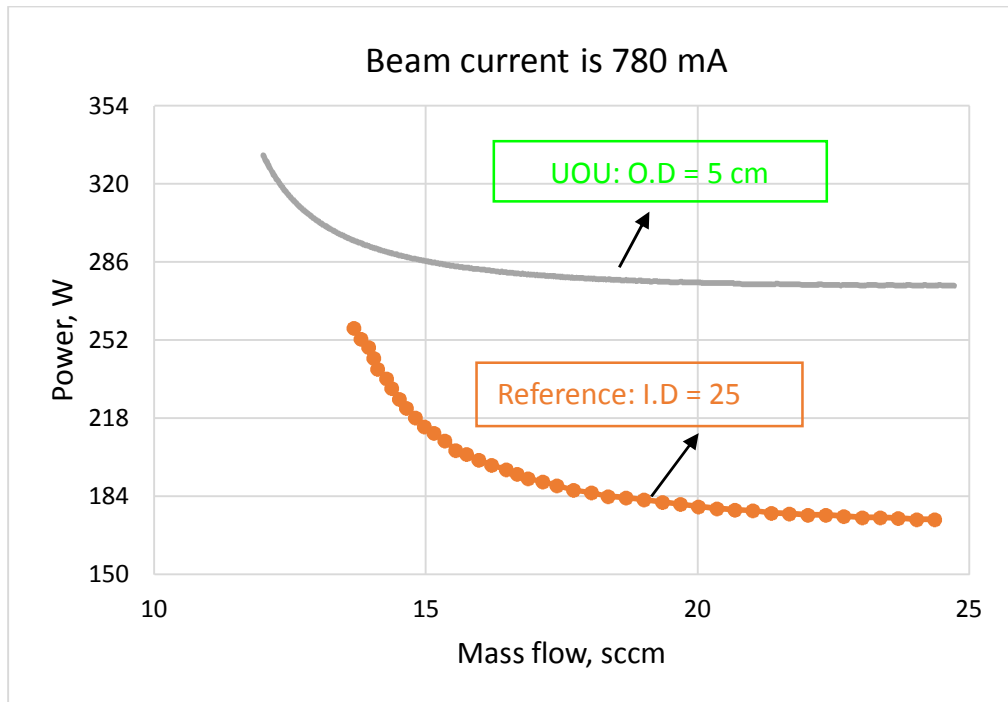


**Fig. 4.13** Size effect in power consumption

The iU-50 thruster is a 5 cm diameter RF-induction ion thruster developed at AARL lab, University of Ulsan, South Korea. Its performance has been well calculated by 0-D analytical discharge model. Preliminary results of the relation between the discharge losses versus the mass utilization efficiency were generated and are shown in Figure 4.14. For the given parameters, of 50 mm chamber diameter, 50 mm chamber length, the coil impedance of 50 Ohm with 12 turn copper RF-induction coil placed around alumina wall, the ion beam current of 10 mA, 90 mA, 100 mA, 115 mA, 125 mA, 150 mA.

The beam current is directly related to the thrust to be generated, and therefore it is held constant.

$$T = \gamma I_b \sqrt{\frac{2MV_b}{e}} \quad (4.3)$$

where  $I_b$  is the beam current,  $M$  is the ion mass which Xenon,  $V_b$  is the beam voltage, and  $\gamma = \alpha \cos\theta$  is a correction factor for the double ion content  $\alpha$  and the angular divergence of the

beam  $\theta$  which is the half angle beam divergence. Since the double ion content is low in RF thrusters and beam half angle for ion thruster us typically  $10^0$ ,  $\gamma$  is estimated to be 0.97. The beam current desired to be generated with this geometry is relatively low, so a smaller ion current is supplied to the RF coils which results in weaker ion confinement and high wall recombination loss.

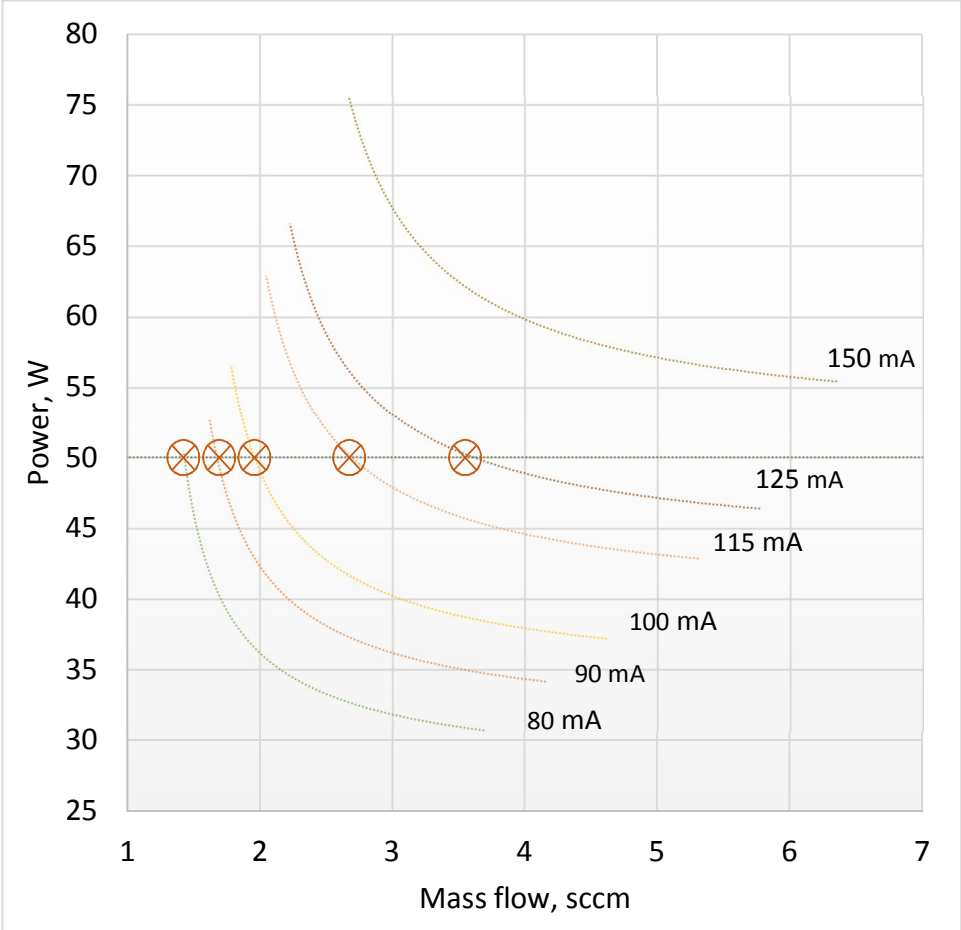


**Fig. 4.14** Power absorbed for iU-50 thruster for different ion beam current

Specific impulse, termed  $I_{sp}$ , is a measure of thrust efficiency and is defined as the ratio of the thrust to the rate of propellant consumption. Specific impulse for constant thrust and propellant flow rate is

$$I_{sp} = \frac{T}{\dot{m}_p g} \tag{4.2}$$

The thrust and Isp of iU-50 are shown in the figure 4.15. As we can see in the figure, the target power level is 50 W that could have reached several mN. This is a reasonable thrust level compared to that found in the literature for RF thrusters with similar size.

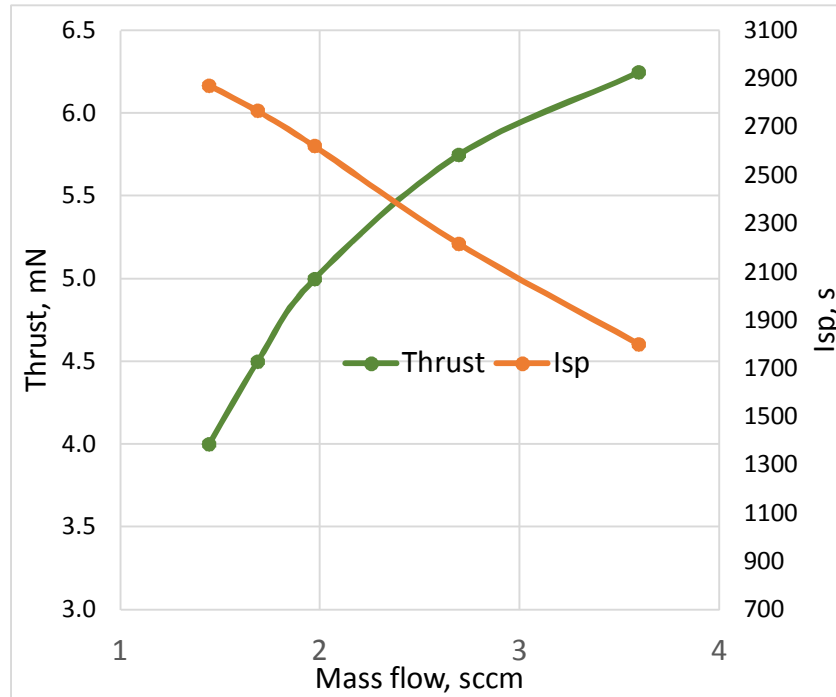


**Fig. 4.15** Thrust and Isp of iU-50 thruster with ion beam current

$$i_b = 80 \text{ mA}, 90 \text{ mA}, 100 \text{ mA}, 115 \text{ mA}$$

#### 4.5 Preliminary iU-50 thruster operation

All tests were performed at the AARL lab vacuum facility. The AARL vacuum chamber has an overall length of 1200 mm and a diameter of 800 mm. Oil rotary pump ( $\sim 2.0 \times 10^{-2}$  torr), turbo molecular pump ( $\sim 5.0 \times 10^{-7}$  torr). Figure 4.16 shows the thruster mounted inside the AARL vacuum and iU-50 thruster operation. Unfortunately, the AARL lacks much equipment for iU-50 thruster measurement. Therefore, the comprehensive experiment on iU-50 can not present in this thesis. However, they will be presented in my Ph. D thesis in the near future at AARL lab. The preliminary performance data of the iU-50 ion thruster is shown in Table 4.3. The data is calculated on basis of scaling law with reference and our 0-D analytical discharge model.

**Table 4.3** Scheduled data of iU-50 thruster

Discharge pressure, $10^{-3}$ torr	2
Transmitter frequency, MHz	13.56
Rf-transmitter power, w	50
Extraction voltage, kV	1
Bean voltage, kV	1-3
Specific impulse, $10^3$ sec	~ 2.6
Thrust, mN	5
Neutral gas, sccm	~ 1-2
Beam diameter, cm	4.5
Beam current, mA	780
Discharge loss, eV/ion	370 - 430
Power efficiency, %	64 - 78
Total thruster efficiency, %	52 - 63

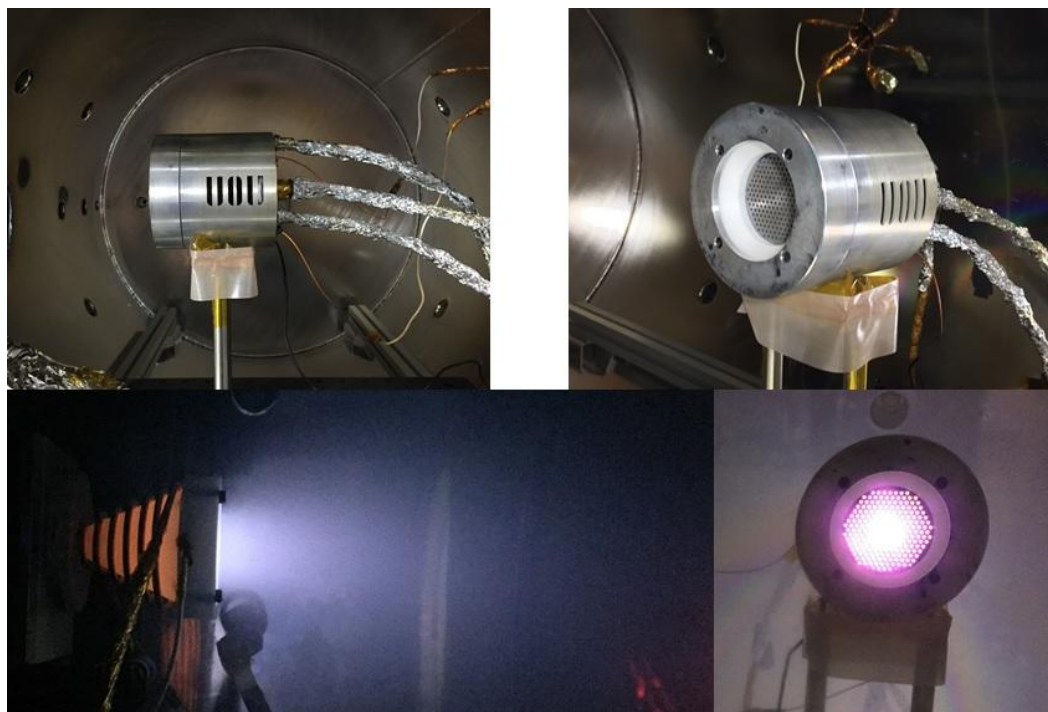


**Fig. 4.16** iU-50 ion thruster was mounted inside AARL vacuum chamber

## **4.6 Chapter summary**

The proposed prototype design and the manufacturing methods of the iU-50 ion thruster were discussed. The iU-50 thruster is proposed to have a conical discharge chamber made of alumina with an inner diameter of 45 mm and length of 50 mm, and consist of a double grid system with 211 holes. Preliminary calculations suggest a thrust in the range of 3-5 mN, and a limiting ion beam current of 0.1 A. Using the 0D Analytical Model on the geometry of the discharge chamber, an average discharge loss of 450 eV/ion was calculated. A key feature of the RF coil configuration design and RF matching network will be presented in the next chapter. The matching network is necessary for the best possible energy transfer from stage to stage.

# Chapter 5. RF matching network and coil configuration

## 5.1 Introduction

It is known that inductive discharges have two discharge models, an H-mode and an E-mode. In the H-mode inductive coupling is dominant over capacitive coupling, leading to high density plasma (ICP), while in the E-mode capacitive coupling is dominant, producing low density plasma (CCP). Figure 5.1 shows the thruster plasma system main parameter representation, and thruster with plasma circuits coupled as in a transformer.

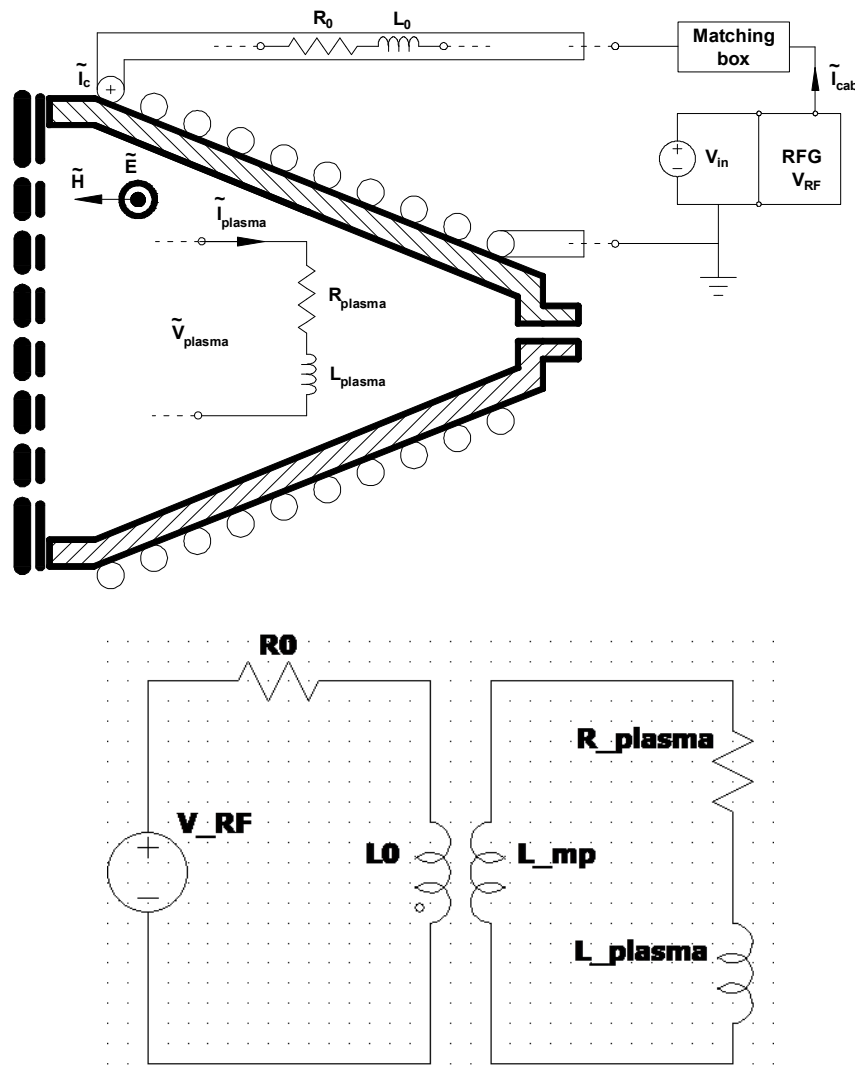


Fig. 5.1 Thruster-plasma system main parameter which coupled as in a transformer circuit

We assume that the coil and thruster of structure are represented using a resistance  $R_0$  and an inductance  $L_0$ . Similarly, the plasma can be thought of as a combination of an inductance  $L_{\text{plasma}}$  and a resistance  $R_{\text{plasma}}$ . This plasma inductance  $L_{\text{plasma}}$  comes from the complex nature of plasma conductivity. This complex part introduces a phase lag between the voltage and current. The complex thruster impedance is obtained as

$$Z = R + jX \quad (5.1)$$

The real part  $R$  of the complex impedance represents the thruster of resistance and is associated with the actual power loss, whereas the complex part represents the reactive component or the phase lag as a result of inductive and capacitive couplings.

The voltage drops over the coil  $\tilde{V}_{\text{RF}}$  is obtained from the thruster impedance  $Z$  as  $\tilde{V}_{\text{RF}} = Z\tilde{I}_{\text{coil}}$ , where  $\tilde{I}_{\text{coil}}$  is the peak coil current given as an input to the electromagnetic model. Furthermore, if the plasma conductivity is set to zero, the plasma contribution from figure 5.1 disappears, and the thruster impedance  $Z$  directly gives the thruster resistance  $R_0$  and inductance  $L_0$  values.

## 5.2 Inductively circuit model (ICP)

A very beginning of the transformer model of an inductive discharge has been proposed by Piejak et al. [46] as shown in figure 5.1. The coil and the plasma form a transformer – the plasma is regarded as the one-turn secondary coil of an air-core transformer. The primary has an inductance  $L_{\text{coil}}$  and the resistance  $R_{\text{coil}}$ . These two quantities define the Q-factor of the coil,  $Q \equiv \omega L_{\text{coil}}/R_{\text{coil}}$ . The coil resistance and the coil inductance, and therefore the Q-factor may be measured experimentally. Or, It can also be evaluated theoretically. The mutual induction between the primary and secondary coil is represented by the mutual inductance  $M$ . It is difficult to calculate

the whole impedance of inductive coupling directly, but using equivalent transformed circuit, we can easily calculate the impedance  $Z_{ind}$  like as below

$$Z_{ind} = Z_p + R_{coil} + j\omega L_{coil} \quad (5.2)$$

Where  $Z_p$  is obtained from the following equation:

$$\frac{1}{Z_p} = \frac{1}{j\omega M} + \frac{1}{j\omega(L_1 - M + L_{e1}) + R_{p1}} \quad (5.3)$$

The RF coil resistance  $R_{coil}$  and inductance  $L_{coil}$  can be described as below:

$$R_{coil} = \rho \frac{2\pi r_{coil} N}{S_{coil}} \quad (5.4)$$

$$L_{coil} = k_N \mu_0 \frac{\pi r_{coil}^2 N^2}{h_{coil}} \quad (5.5)$$

Where  $\rho$  is the resistivity of a copper wire,  $r_{coil}$  is the radius of the RF coil,  $S_{coil}$  is the effective cross section area of the wire which is  $2\pi r_{coil} d_{sk}$ ,  $k_N$  is Nagaoka coefficient,  $\mu_0$  is the permeability in vacuum,  $h_{coil}$  is the height of the RF coil. The absorbed complex power in the ICP is defined as

$$P_{ind} = (Z_{ind} I_{ind}) \tilde{I}_{ind} \quad (5.6)$$

Where  $I_{ind}$  is the current through the primary coil, and  $\tilde{I}_{ind}$  is the conjugate complex number of  $I_{ind}$ .

L-type impedance matching network for a RF antenna (The LT-spice simulation model of RF source, impedance matching L-type LCL network and RF antenna is shown in figure 5.2. The RF thruster voltage ( $\sim 50$  V peak) and current ( $\sim 3$  A) flowing through it is shown in figure 5.3. The voltage ( $\sim 320$  V peak) generated across the parallel inductor (LP) and current ( $\sim 3$  A) flows through

it is shown in figure 5.4. The RF source peak is 340 V and its supplied peak current is 10 A, is show in figure 5.5. Note that, the bandwidth of LCL L-type matching network is greater than CCL L-type matching network.

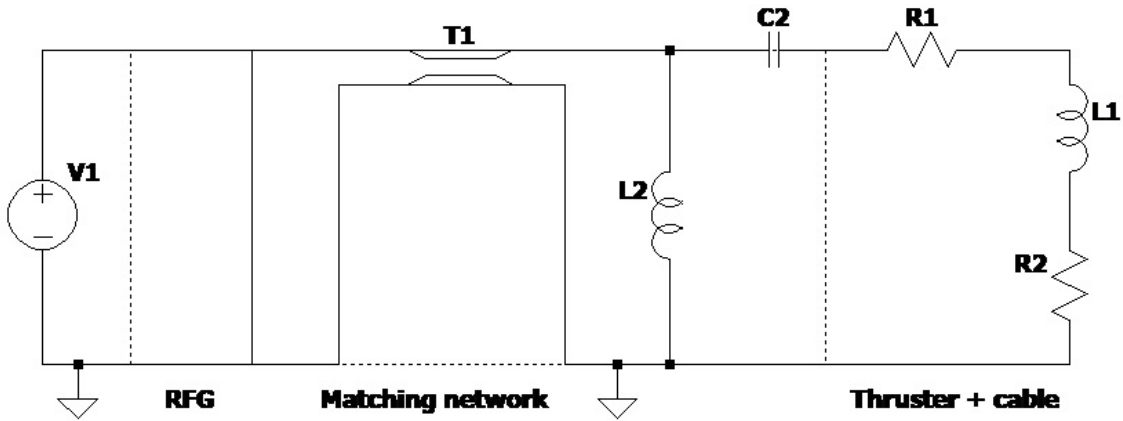


**Fig. 5.2** Simulation circuit model at 13.56 MHz RF source with impedance matching network with LCL network ( $50\Omega$ ) for RF antenna in LT-spice.

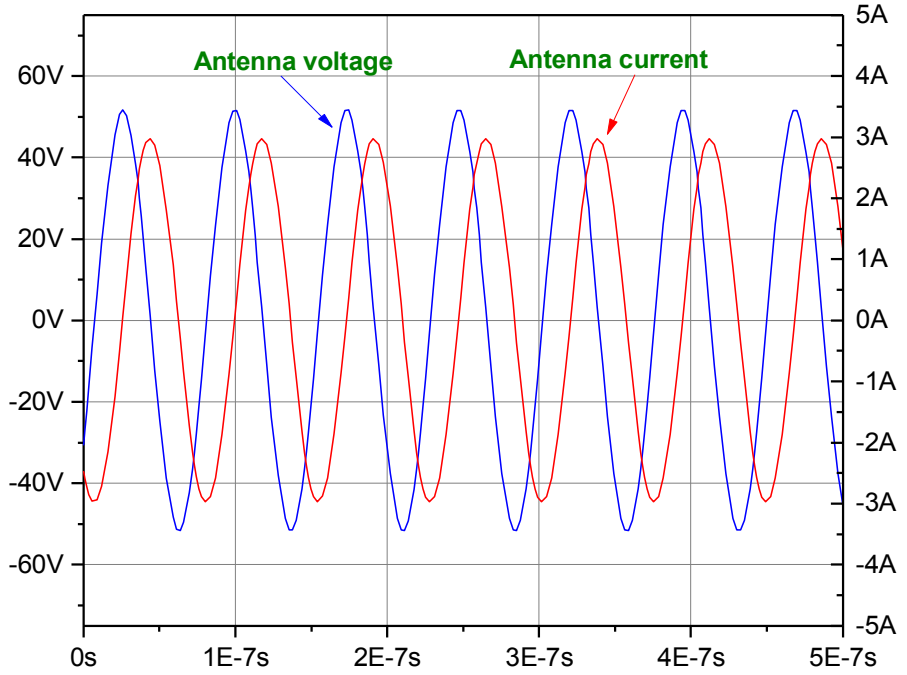


**Fig. 5.3** Simulated result in LT-spice for RF antenna voltage and current, for LCL impedance matching network

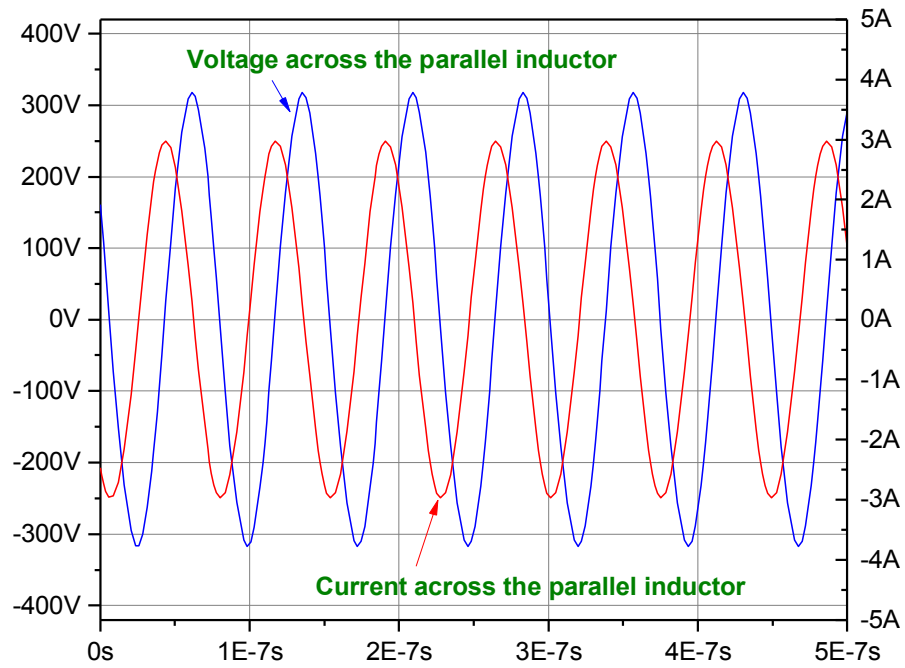


**Fig. 5.4** Simulated result in LT-spice for voltage and current across the parallel inductor  $L_2$ , for LCL impedance matching network.

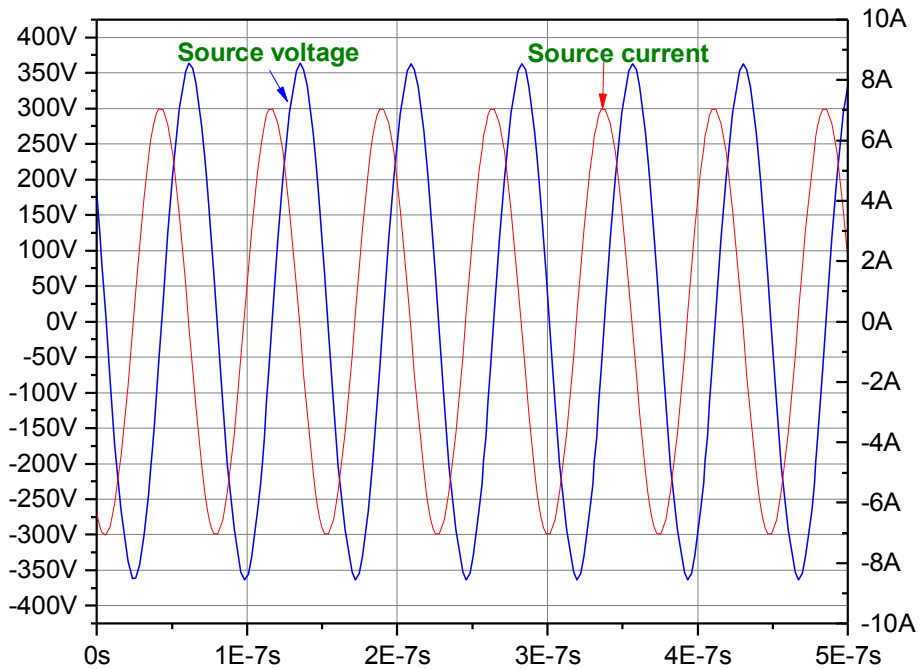


**Fig. 5.5** Simulated result in LT-spice for source voltage and current, for LCL impedance matching network.

### 5.3 Impedance matching

A matching network is introduced between the RF power supply and the ICP allowing maximum power transfer and a safe operating region for the power supply. In operation the match components may be fixed or variable and tuned either manually or automatically. Modern plasma thruster may be powered by multiple power supplies at different operating frequencies. This note shows how a match can be designed using dimensions of the chamber, properties of the feed gas and the specification of the power supply.

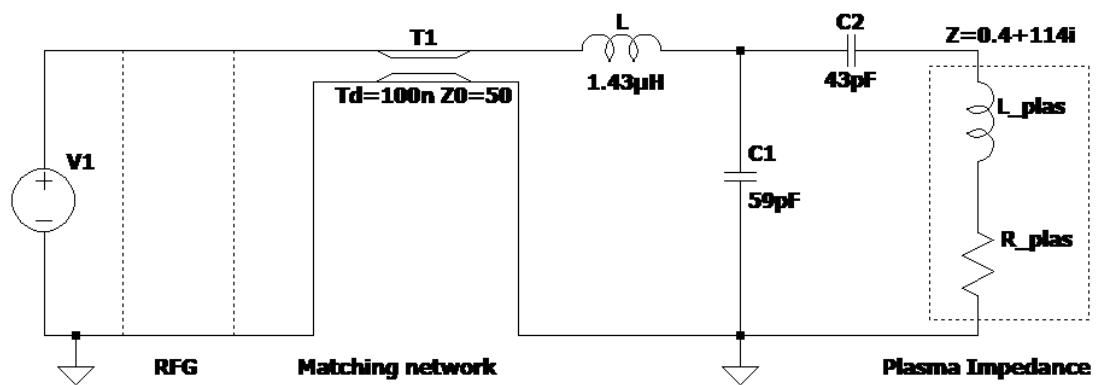


**Fig. 5.6** *L-match including blocking and inductance of plasma.*

Figure 5.6 is a schematic of a RF power supply ( $V_s$ ,  $R_s$ ) connected to a L-type match network ( $L_m$ ,  $C_p$ ) with an additional DC blocking capacitor ( $C_b$ ). The match network is connected to a plasma load with a parallel stray capacitance ( $L_s$ ). The plasma voltage and current are  $V$  and  $I$ . In order to compute the optimum values for the parallel capacitor  $C_p$  and the inductor  $L_m$ , the plasma impedance is required,  $Z_p$ . Using  $Z_p = R_p + jX_p$  and the generator source resistance,  $R_s$ , the following can be used to compute  $C_p$  and  $L_m$ . Defining:

$$X_m = \sqrt{R_p R_s - R_p^2} - X_p \quad (5.7)$$

And

$$X_m = \sqrt{R_p R_s - R_p^2} - X_p \quad (5.8)$$

Then the match inductance is given by:

$$L_m = \frac{X_m}{2\pi f} \quad (5.9)$$

And the parallel capacitance is given by:

$$C_p = \frac{B_m}{2\pi f} \quad (5.9)$$

In order to evaluate the result, two meaningful measures are used, the maximum power transfer coefficient and the efficiency. The maximum power transfer is given by:

$$P_{\max} = \frac{V_s^2}{8R_s} \quad (5.10)$$

Where  $V_s$  is the generator voltage, and the maximum power transfer coefficient is then given by:

$$\alpha = \frac{P_{\text{plasma}}}{P_{\max}} \quad (5.11)$$

The efficiency is then simply:

$$\eta = \frac{P_{\text{plasma}}}{P_{\text{plasma}} + P_s} \quad (5.12)$$

Where  $P_s$  is the power lost in the generator. Figure 5.7 shows that the impedance matching on smith chart. This is expected because the values of  $C_p$  and  $L_m$  used to calculate the match component were determined at 50 W plasma power. Figure 5.8 show a plot of simulated frequency response in ADS software for RF antenna current. Matching occurs at 13.56 MHz and  $10^{-2}$  torr corresponding to the conditions used to determine  $C_p$  and  $L_m$ . At low pressure the plasma is more resistive and a significant mismatch occurs. The effect is less pronounced at higher pressures.

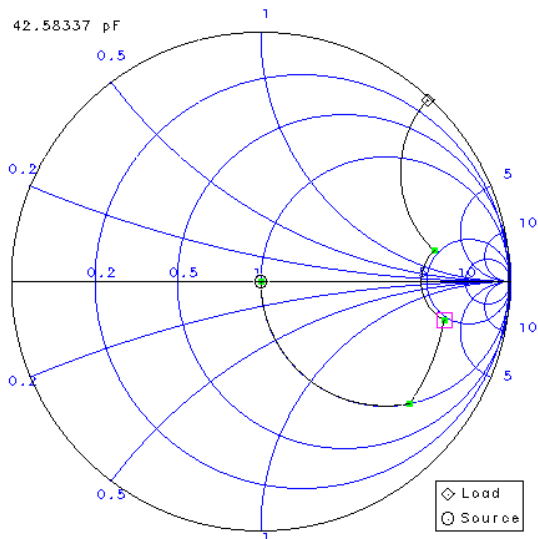


**Fig. 5.7** Plot of the impedance matching on smith chart

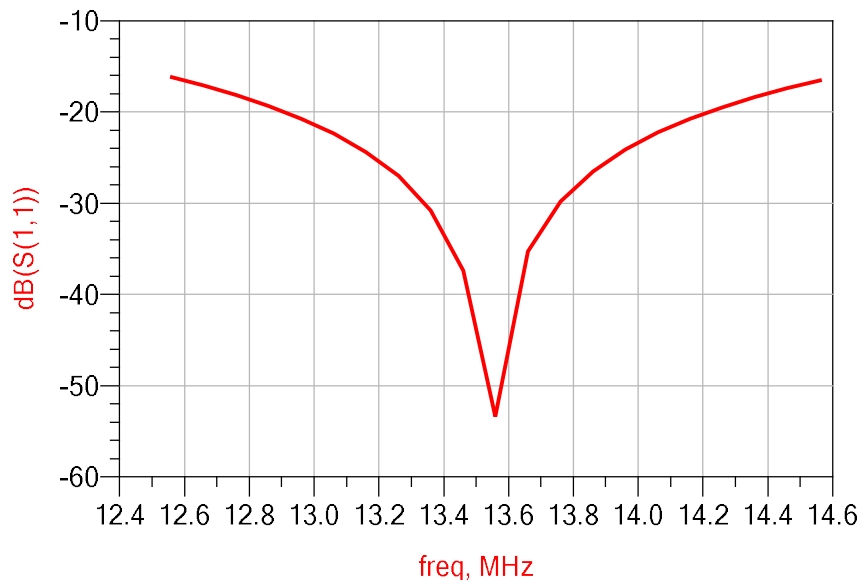


**Fig. 5.8** Plot of the simulated frequency response in L-match circuit

These results show how a matching network for iU-50 thruster can be designed using the dimensions of the thruster, the properties of the feed gas and the characteristics of the generator. Estimates of the power transfer coefficient as a function of power frequency can be made.

### 5.4 Extended-field electromagnetic model

A model based on the iU-50 ion thruster geometry has been designed in order to find the discharge chamber temperature distribution. Thermal plasmas are assumed to be under partial to complete local thermodynamic equilibrium (LTE) conditions. Under LTE, the plasma can be

considered a conductive fluid mixture and therefore, be modeled using the magnetohydrodynamics (MHD) equations. This model shows how to use the Equilibrium Inductively Coupled Discharge interface to simulate the plasma generated in the discharge chamber of iU-50 ion thruster. The ideal for this model was referenced to [47] and uses the following assumptions:

1. The RF discharge chamber is modeled by a fully axisymmetric configuration.
2. The coil consists of parallel current carrying rings with a circle cross section, 2.9 mm in diameter. This implies neglecting the axial component of the coil current.
3. Steady state, laminar pure argon plasma flow at vacuum pressure
4. Optically thin plasma under local thermodynamic equilibrium (LTE) conditions.
5. Viscous dissipation and pressure work in the energy equation are neglected.

Figure 5.9 shows the geometry of the model

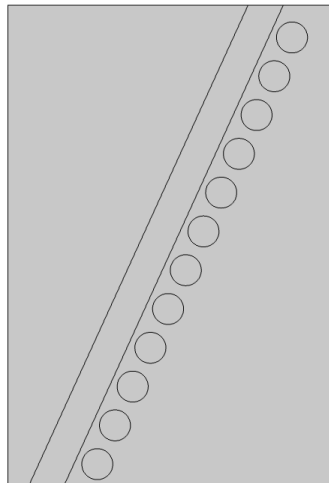
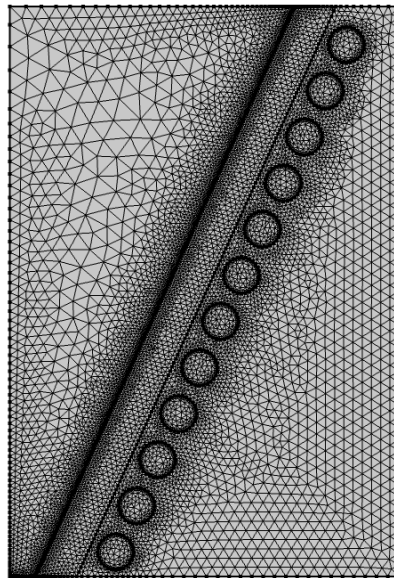


**Fig. 5.9** Schematic of the iU-50 thruster discharge chamber

In this model excitation is provided to a 12 turns coil at 13.56 MHz. The gas flowing in the sheath tube (plasma confinement tube) is then ionized by Joule heating. The model is solved using a frequency-transient study in combination with a single turn coil feature which set a fixed power

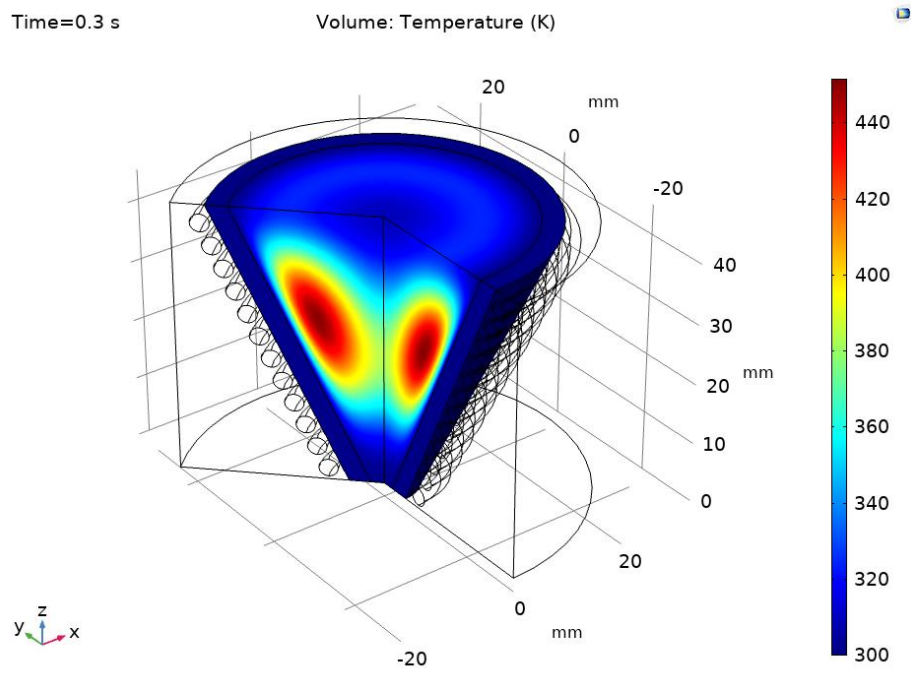
to the system (50 W). By fixing the power, the current and electric potential can vary in the coil as the plasma electrical conductivity builds up. Steady-state is reached when the coil current stabilized to it's nominal value. The temperature dependent argon's physical properties are loaded from the material library under Equilibrium Discharge. Note also that a minimum electrical conductivity has been used to initiate the plasma. The latter has been set to 1 S/m.

Figure 5.10 represents the model mesh generated for iU-50 thruster discharge chamber without grids



**Fig. 5.10** Mesh generated of the iU-50 thruster discharge chamber

Figure 5.11, and figure 5.12 respectively shows the plasma temperature distribution, and velocity magnitude of the argon plasma after 0.3 s. Figure 5.13 shows the electrical conductivity of the plasma at the same time (0.3 s). Note that, for this figure, the electrical conductivity of the other constituents of the model has been set to 0 for sake of visualization. Figure 5.14 displays the magnetic flux norm at steady state (0.3 s). Note that the electrical conductivity of the plasma screens the magnetic flux as a consequence of the skin effect.



**Fig. 5.11** Surface plot of the LTE plasma temperature inside the discharge chamber

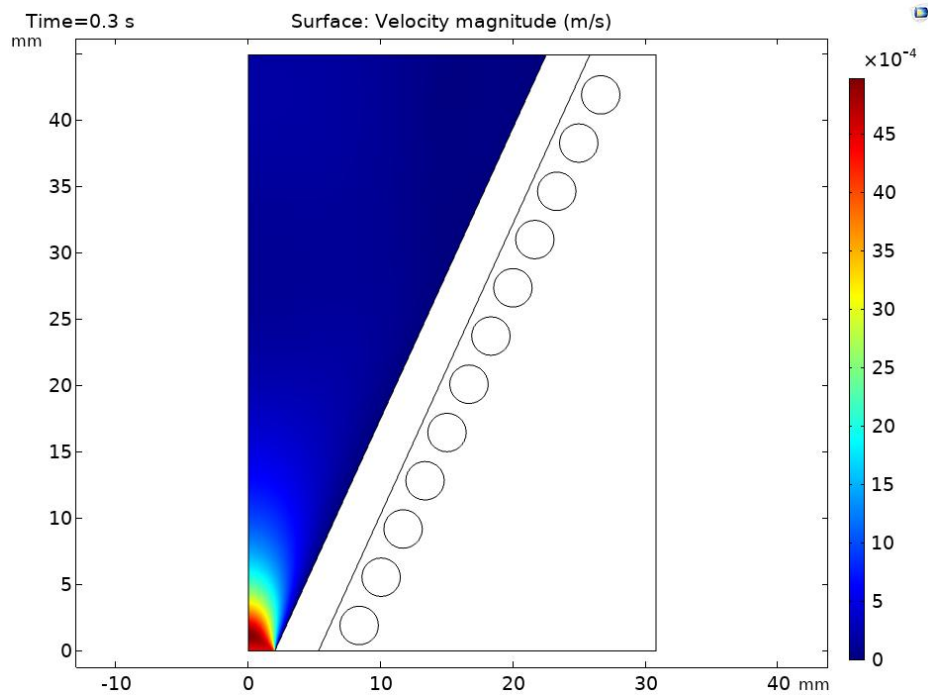


**Fig. 5.12** Plot of the velocity magnitude

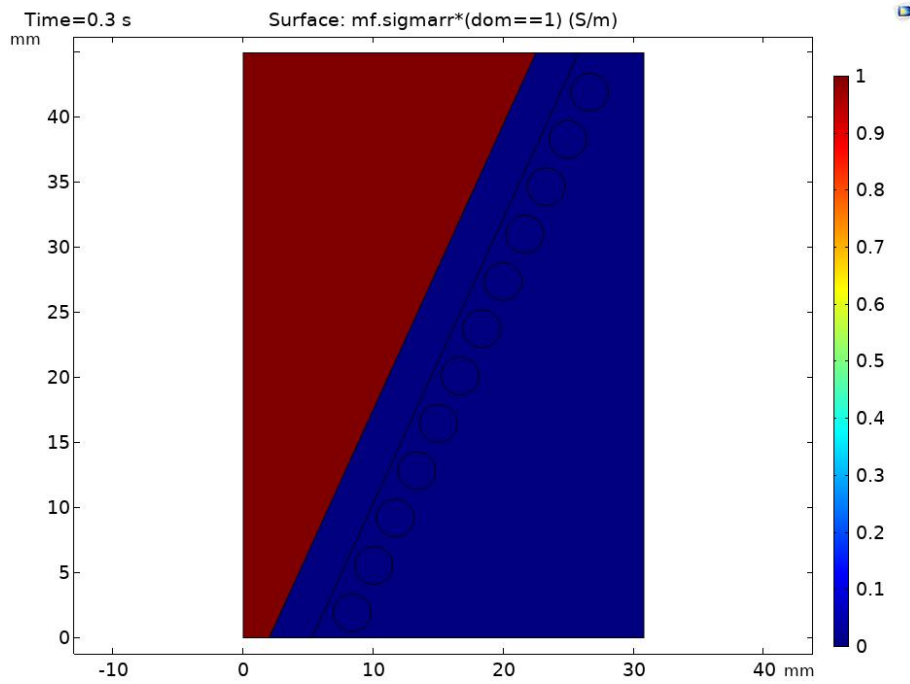


**Fig. 5.13** *Plot of the plasma electrical conductivity*

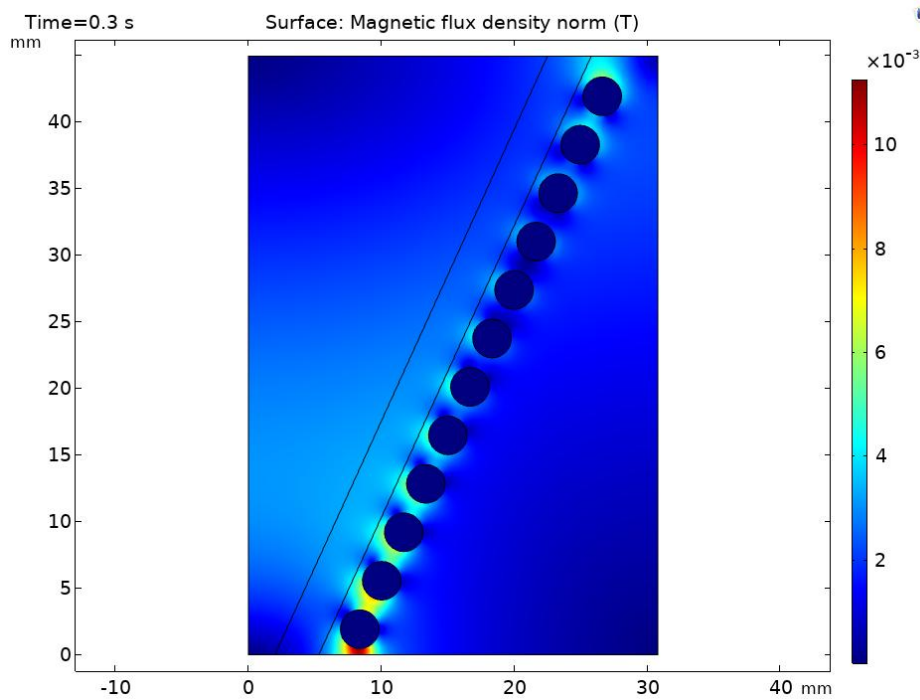


**Fig. 5.14** *Norm of the magnetic flux. Note the effect of the resistivity on the penetration of the field (skin effect).*

Figure 5.15 shows the coil current as a function of the simulation time. The steady state is reached when the current stabilizes, i.e. around  $t=0.3$  s.

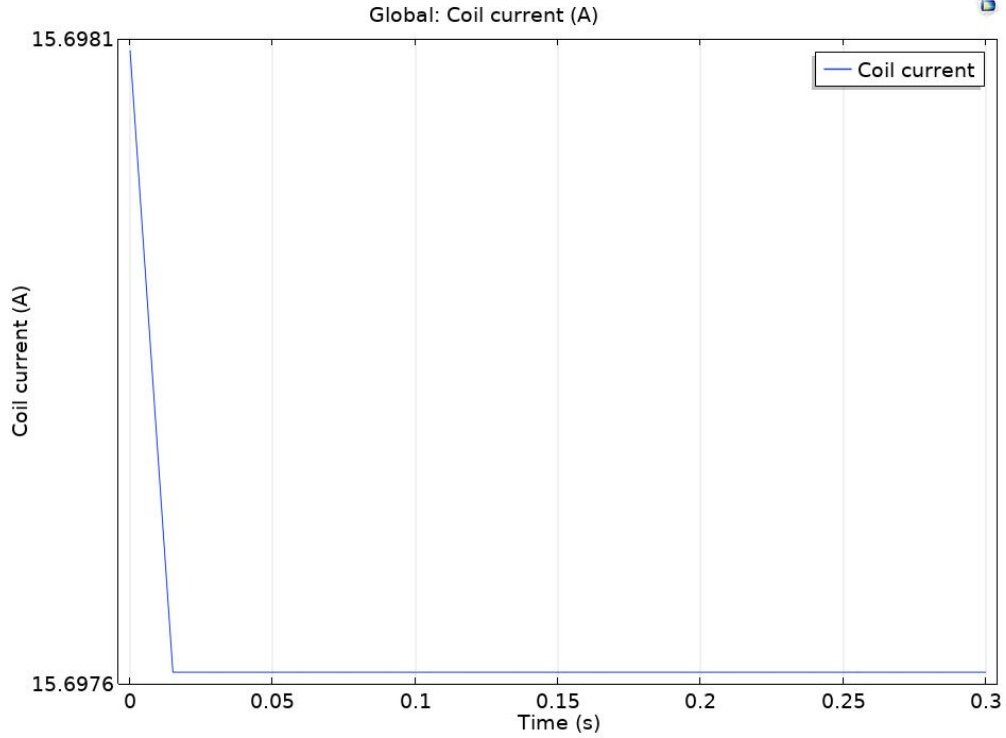


**Fig. 5.15** Coil current as a function of time for a fixed excitation power. Note the stabilization of the current density as the system reach the steady state

## 5.5 Thermal plasma model

Low pressure discharges are characterized by the fact that the electron temperature is much higher than the neutral gas temperature. As the gas pressure increases, the number of collisions between the electrons and neutrals increases. At high enough pressures the electron temperature becomes equal to the gas temperature. At this point the plasma is in local thermodynamic equilibrium and a much simpler MHD model can be used to model the plasma. This model simulates a plasma at medium pressure (1 torr), where the gas temperature cannot be assumed to be constant but the plasma is still not in local thermodynamic equilibrium.

$$\frac{\partial}{\partial t} (n_e) + \Delta \cdot [-n_e (\mu_e \cdot E) - D_e \cdot \Delta n_e] = R_e \quad (5.13)$$

$$\frac{\partial}{\partial t} (n_\epsilon) + \Delta \cdot [-n_\epsilon (\mu_\epsilon \cdot E) - D_\epsilon \cdot \Delta n_\epsilon] + E \cdot \Gamma_e = R_\epsilon \quad (5.14)$$

The electron source  $R_e$  and the energy loss due to inelastic collisions  $R_\epsilon$  are defined later. The electron diffusivity, energy mobility, and energy diffusivity are computed from the electron mobility using:

$$D_e = \mu_e T_e \quad (5.15)$$

$$\mu_\epsilon = \frac{5}{3} \mu_e \quad (5.16)$$

$$D_\epsilon = \mu_\epsilon T_\epsilon \quad (5.17)$$

The source coefficients in the above equations are determined by the plasma chemistry using rate coefficients. Suppose that there are  $M$  reactions that contribute to the growth or decay of electron density and  $P$  inelastic electron-neutral collisions. In general,  $P \gg M$ . In the case of rate coefficients, the electron source term is given by:

$$R_e = \sum_{j=1}^M x_j k_j N_n n_e \quad (5.18)$$

Where  $x_j$  is the mole fraction of the target species for reaction  $j$ ,  $k_j$  is the rate coefficient for reaction  $j$  (SI unit:  $\text{m}^3/\text{s}$ ), and  $N_n$  is the total neutral number density (SI unit:  $1/\text{m}^3$ ). The electron energy loss is obtained by summing the collisional energy loss over all reactions:

$$R_\epsilon = \sum_{j=1}^P x_j k_j N_n n_e \Delta \epsilon_j \quad (5.19)$$

Where  $\Delta \epsilon_j$  is the energy loss from reaction  $j$  (SI unit: V). The rate coefficients can be computed from cross section data by the following integral:

$$k_k = \gamma \int_0^\infty \epsilon \sigma_k(\epsilon) f(\epsilon) d\epsilon \quad (5.20)$$

Where  $\gamma = (2q/m_e)^{1/2}$  (SI unit:  $\text{C}^{1/2}/\text{kg}^{1/2}$ ),  $m_e$  is the electron mass (SI unit: kg),  $\epsilon$  is energy (SI unit: V),  $\sigma_k$  is the collision cross section (SI unit:  $\text{m}^2$ ), and  $f$  is the electron energy distribution function. In this case, a Maxwellian EEDF is assumed. For non-electron species, the following equation is solved for the mass fraction of each species:

$$\rho \frac{\partial}{\partial t} (w_k) + \rho (u \cdot \nabla) w_k = \nabla \cdot j_k + R_k \quad (5.21)$$

The electrostatic field is computed using the following equation:

$$-\nabla \cdot \epsilon_0 \epsilon_r \nabla V = \rho \quad (5.22)$$

The space charge density  $\rho$  is automatically computed based on the plasma chemistry specified in the model using the formula:

$$\rho = q \left( \sum_{k=1}^N Z_k n_k - n_e \right) \quad (5.23)$$

The iU-50 discharge chamber geometry is simply a conical Alumina vessel with a 12 turns coil around it. Gas flow in from the bottom and exits out of the top where these ions will be accelerated and formed by ion optic system. The gas is heated through elastic and inelastic collisions. The inelastic collisions are responsible for the bulk of the gas heating. A fixed power of 50 W is applied to the coil. Figure 5.15 shows the model mesh generated using triangular and various elements size for iU-50 thruster discharge chamber.

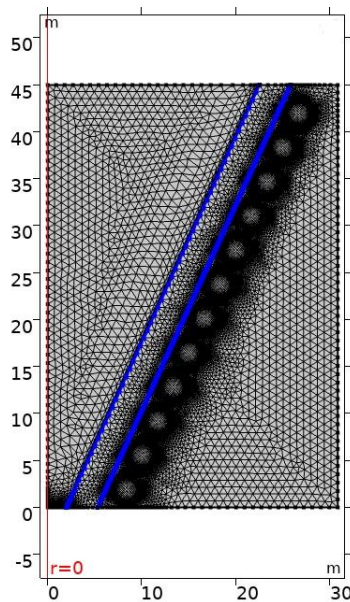


**Fig. 5.16** Mesh generated for plasma thermal model

Figure 5.17 shows the electron density distribution, electron temperature and plasma potential of the argon plasma after 0.01 s. Figure 5.18 shows the magnetic flux density norm (T) at steady state and velocity magnitude.

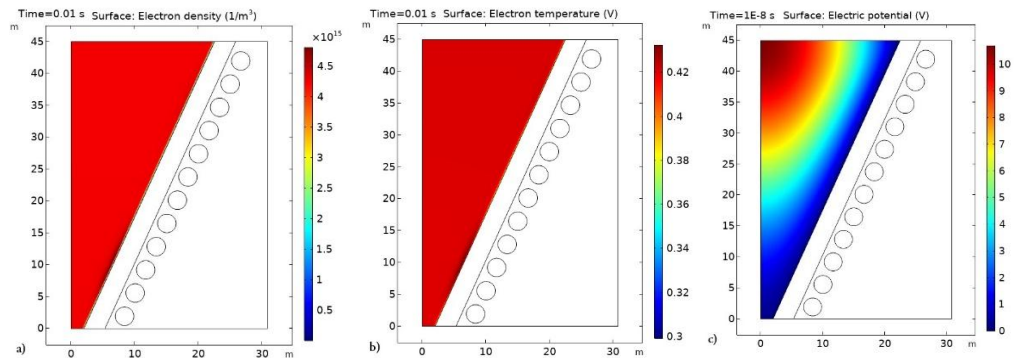


**Fig. 5.17** a) Plot of the electron density distribution; b) Plot of the electron temperature of Argon plasma after 0.01s; and, c) Plot of the plasma potential inside the chamber after 1E-8s

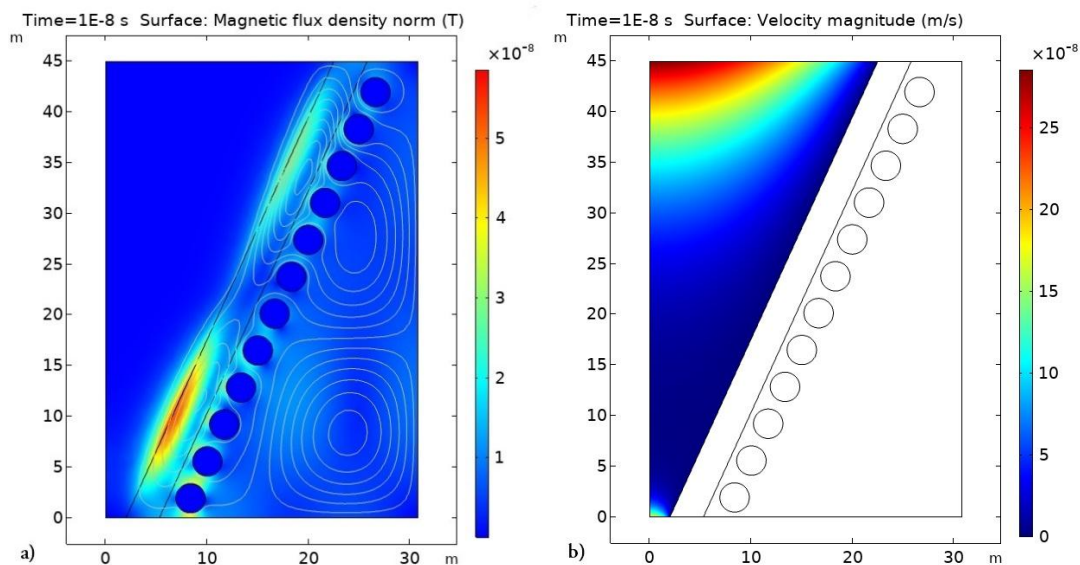


**Fig. 5.18** Plot of the magnetic flux density norm (T) at steady state

## **5.6 Chapter summary**

This chapter presents a high efficiency and high performance radio-frequency (RF) power supply and rf coil that around the discharge chamber is the crucial part in the iU-50 thruster development. For this purpose, the supply needs to guarantee highly efficient RF signal generation and transfer to the thruster coil and furthermore an optimal power coupling between coil and plasma. To optimize the iU-50 thruster performance, the maximum power transfer has to be transported inside the discharge chamber with minimized power loss through coaxial cable, RF coil and discharge chamber walls. To do so, we need to develop an automatic matching network and select a suitable coil around the discharge chamber.

## Chapter 6. Measurement System Development

This chapter describes the design, novel calibration technique, and characterization of a thrust stand capable of micro-Newton resolution. In particular, a permanent magnet structure was designed to produce a uniform magnetic field, and a multiturn coil was made to produce a calibration force less than  $\sim 5$  mN. The electromagnetic calibration force for iU-50 thrust measurements was linear to the coil current and changed less than 2.5% when the distance between the coil and magnet changed  $\sim 6$  mm. Furthermore, this thesis proposed two novel systems that are a novel method for electrostatic comb implementation and convenient power supply for a retarding potential analyser (RPA).

### 6.1 Micro-Newton resolution thrust stand development

#### 6.1.1 Torsion balance dynamics

The micro-Newton AARL thrust stand is essentially a torsion balance and was conceived as part of a larger experiment for iU-50 ion thruster capable of delivering sub-micronewton level thrust for nanosatellites. The thrust stand aims to resolve forces smaller than 1 micronewton, preferably down to several nano-Newtons ( $\sim 10$  nN). Since the torsion balance is a proportional balance, it needs a priori calibration before forces can be measured reliably and with known certainty. Figure 6.1 schematic shows a 3D rendering of the AARL thrust stand.

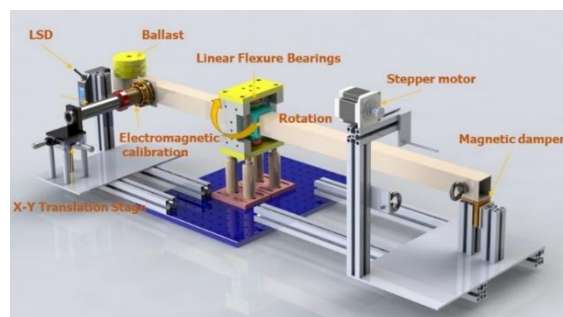


**Fig. 6.1** Details of the AARL thrust stand

The two flexure pivots at the vertical ends of the crossbeam from the torsion spring providing the restoring torque. The cross-beam is laterally unsymmetrical to optimize the sensitivity within the space constraints (the entire system must fit inside a vacuum chamber sized  $L = 1200$  mm and  $R = 500$  mm with enough clearance). The ballast, located at the short end of the cross-beam, acts as a counterweight and balances the unsymmetrical beam. A special electromagnet provides a known force or controlled displacement for calibration. An optical linear displacement sensor measures the displacement of the balance arm at a distance to calculate the angular deflection.

The statics and dynamics of an undamped torsion balance can be completely characterized by two parameters: the torsion spring constant  $k_\theta$  and the moment of inertia (MI) of the system  $I_\theta$ , which govern the natural frequency of the system as

$$\omega_n = \sqrt{\frac{k_\theta}{I_\theta}} \quad (6.1)$$

However, for practical reasons, damping is desired to bring the system to a steady state, facilitating quick readings. For such a damped system, the equation of motion is

$$\ddot{\theta} + 2\zeta\omega_n\dot{\theta} + \omega_n^2\theta = \frac{f(t)l_T}{I_\theta} \quad (6.2)$$

Where  $\theta(t)$  is the instantaneous deflection angle,  $\zeta$  is the damping coefficient,  $f(t)$  is the time dependent force, and  $l_T$  is the distance from the pivot at which the force forms a torque (moment arm). For a constant force  $f(t) = F$ , Ziemer [48] gives the solution as

$$\theta(t) = \frac{Fl_T}{I_\theta\omega_n^2} \left[ 1 - \exp(-\zeta\omega_n t) \times \left( \frac{\zeta}{\sqrt{1-\zeta^2}} \sin(\sqrt{1-\zeta^2}\omega_n t) + \sin(\sqrt{1-\zeta^2}\omega_n t) \right) \right] \quad (6.3)$$

The steady state solution to which can be written (using small angular displacement  $\theta = \frac{x}{l_T} \frac{180}{\pi}$ ) as

$$\theta(t \rightarrow \infty) = \frac{Fl_T}{k_\theta} \Rightarrow F = \frac{\theta(\infty)k_\theta}{l_T} \Rightarrow F = \frac{k_\theta x}{l_T l_s} \frac{180}{\pi} \quad (6.4)$$

Hence, knowing the steady state linear displacement  $x$ , the spring constant  $k_\theta$ , the moment arm length  $l_T$ , and the sensor distance  $l_s$ , the unknown force  $F$  can be readily calculated. For a given resolution of linear displacement  $x$ , the force resolution can be maximized either by increasing the moment length and the sensor distance, or by using torsion springs with a lower spring constant. The moment length and the sensor distance are constrained by the operating envelop of the stand, whilst there is a tradeoff between lower spring constants and the axial and radial load bearing capacity of the springs. As a conservative measure, the current springs are chosen to have a load bearing capacity of  $\sim 15$  Kg, more than what the thrust stand would be required to withstand.

For the current design, both the sensor and the calibration electromagnet are located at a distance of 300 mm from the pivot axis ( $l_s = l_T = l$ ). The torsion springs, procured from Riverhawk Company, have a rated spring constant of 5.4232 N-mm/Degree each, with an accuracy of  $\pm 10\%$ . In the given configuration, the two torsion springs act in parallel (due to identical displacements), hence the total spring constant is just a numerical sum giving a mean total spring constant for the system of around 10.8464 N-mm/Degree. Having these two parameters fixed by design, the resolution of the stand is limited only by the resolution with which the linear displacement  $x$  can be measured, and the accuracy with which the system can be calibrated.

## 6.1.2 Calibration

The simple method using standard weight for calibration. The weight is added at the end of the bar where iU-50 ion thrust is going to be mounted for the future experiment. The weight value from 1 mg to 900 mg, the results of calibration are shown in table 6.1.

**Table 6.1** Details of the results measurement

mg	kg	F (N)	k	IT (mm)	$\delta 1$ (mm)	$\delta 2$ (mm)	$\delta$ calibration
1	0.000001	9.81E-6	10.8464	700	0.0033	0.0031	- 0.00019
5	0.000005	49.05E-6	10.8464	700	0.0166	0.0160	- 0.00054
10	0.00001	98.10E-6	10.8464	700	0.0331	0.0329	- 0.00019
20	0.00002	196.20E-6	10.8464	700	0.0663	0.0617	- 0.00463
50	0.00005	490.50E-6	10.8464	700	0.1657	0.1578	- 0.00786
100	0.0001	981.00E-6	10.8464	700	0.3313	0.3402	0.00890
200	0.0002	1962.00E-6	10.8464	700	0.6627	0.6950	0.03227
300	0.0003	2943.00E-6	10.8464	700	0.9940	1.0479	0.05392
400	0.0004	3924.00E-6	10.8464	700	1.3253	1.3987	0.07337
500	0.0005	4905.00E-6	10.8464	700	1.6566	1.7501	0.09354
600	0.0006	5886.00E-6	10.8464	700	1.9880	2.1130	0.12499
700	0.0007	6867.00E-6	10.8464	700	2.3193	2.4832	0.16385
800	0.0008	7848.00E-6	10.8464	700	2.6506	2.8420	0.19135
900	0.0009	8829.00E-6	10.8464	700	2.9820	> 3	#####

And then, effective of the pivot spring as well as AARL thrust stand design is shown in figure 6.2

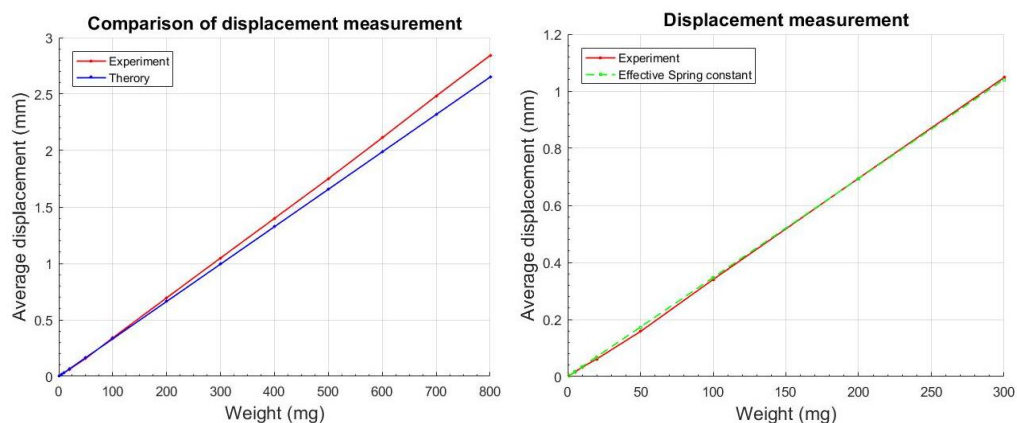


**Fig. 6.2** Comparisom between weight and theroiry

A linear increase in the displacement for both experiment and analytic solution with a slightly bigger slope in experiment. The effective spring constant decreased from 10.8646 to 10.5636. For a comprehensive evaluation, the calibration test with a complete system including gas feed line and electrical connections need to be done many times.

## **6.2 Development of AARL electrostatic comb system for AARL thrust stand**

### **6.2.1 Fundamental of the electrostatic comb**

An electrostatic calibration technique is highly flexible in producing a wide range of force and it is widely applied for nano-newton to micro-newton thrust stand calibration. Based on the printed circuit board and commercial fins, the comb can be realized flexibly with the output force conveniently extended. The force generated by this kind of comb is theoretically analyzed. Different from the traditional comb structure, the conductive area of the comb fixed plate is minimized to improve the force consistency over engagement.

The geometry of the PCB comb is shown in figure 6.3 Similar to the structure of traditional electrostatic combs, it consists of two identical printed circuit boards as the fin fixed plate. A set of commercial insert connectors are used as fins welded on the PCBs. The combs engaged for a particular distance and an attractive force is produced when a potential difference is applied on the combs. The fingers have width  $W_s$ , height  $H$ , thickness  $W_f$ , and the clearance between the two comb fingers is  $D$ . The engagement of the movable fingers and fixed fingers is  $X$ . The number of the comb fingers is denoted as  $N \times M$ , where  $N$  represents the number of the fingers in the column and  $M$  is the row number. On the PCB, extra holes have been reserved so that the number of the fingers can be easily adjusted. In the experiments, the clearance  $D$  between the adjacent fins from the front view is 4.5 mm and the distance between the two fins in the row  $W$  is 9 mm. Meanwhile, the width of the fin  $2d$  is 8 mm, while the height of the fin  $H$  is 18 mm. According to Johnson, the electrostatic forces can be divided into local force and global force [48].

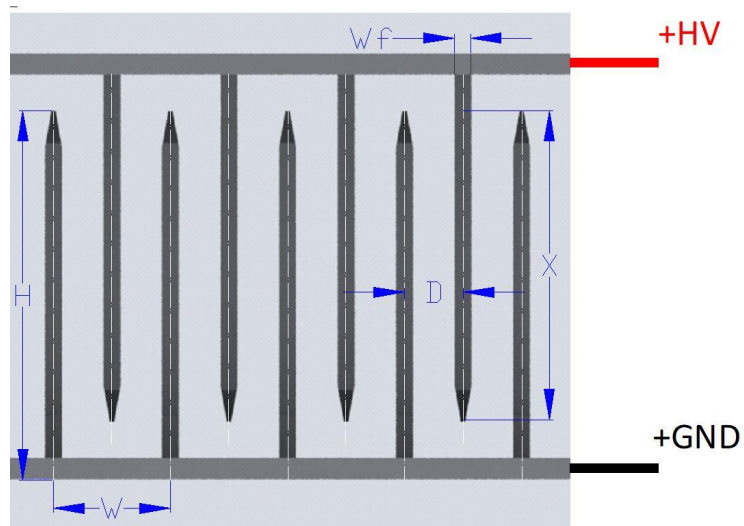


**Fig. 6.3** Geometry of side view of the PCB electrostatic comb

Figure 6.4 represents the AARL PCB design by using Altium software, which is different from the traditional comb structure. The electrostatic force between the parallel plate is inversely proportional to the square of the distance among the plates. Moreover, when the distance between the plate decreases, the force produced by the fin and plate will cause an abrupt increase in the output force.

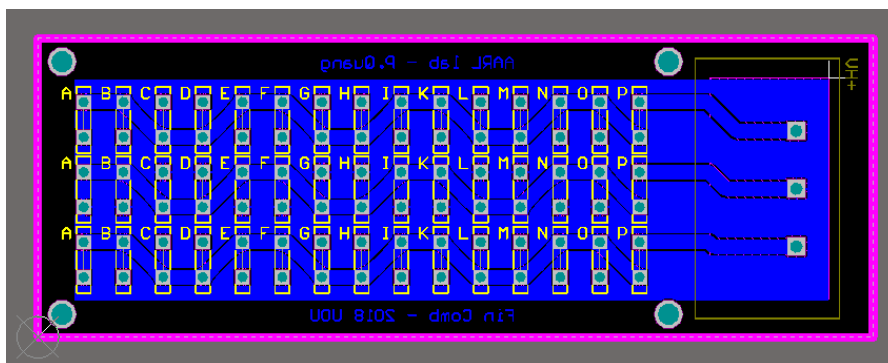


**Fig. 6.4** Geometry of side view of the PCB electrostatic comb

The calculation of the electrostatic comb force can be divided into local field force and global force calculation. In the local field, the electric lines are confined between the two engaged fingers and most of the electric potential energy is concentrated in the area, so it is the main part of the total electrostatic force. The global region contains both the capacitance between fixed fingers and

the capacitance between the conductive plate and fins. The local and global field energy can be obtained based on the virtual work principle illustrated in [49] and [50]. The energy contained in the local field and global field can be expressed as follows.

$$U_{\text{filed}}^{\text{Local}} = \frac{\epsilon_0}{2} \iiint v |\bar{E}|^2 dV \approx x_0 QV \quad (6.5)$$

$$U_{\text{filed}}^{\text{Global}} = 4(c + g)\epsilon_0 \iint S |\bar{E}|^2 dS = -\frac{4(c+g)}{\pi} \epsilon_0 V^2 \ln \left[ \frac{-x_0}{2(2l-x_0)} \right] \quad (6.6)$$

And the quantity of the electric charge

$$Q \approx 2\epsilon_0 \frac{V}{\pi} \ln \left[ \left( \frac{c}{g} + 1 \right)^2 - 1 \right] \left( 1 + 2 \frac{g}{c} \right)^{\frac{c}{g}+1} + \frac{\pi d}{g} \quad (6.7)$$

where  $\epsilon_0$  is the permittivity of free space,  $\bar{E}$  is the average electric field strength,  $x_0$  is the engagement,  $Q$  is the total charge on the comb fin,  $V$  is the applied voltage,  $S$  is the surface excluding the interior of the conductive fingers. The electric potential and electric field are shown in Figure 6.5

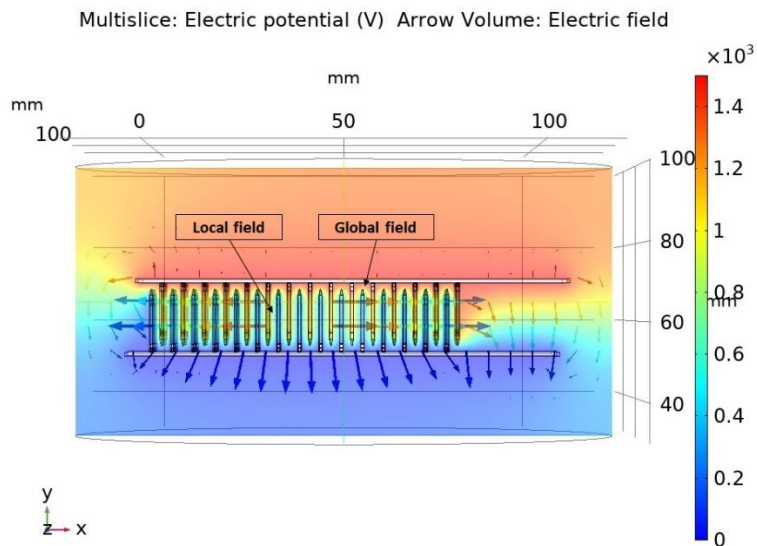


**Fig. 6.5** Plot of the electric field and electric potential distribution

In the most engaged area, the field is confined to a finger cross section, while the local force is generated by the electric field lines that initiate from movable fingers and end on the fixed fingers. The overall electrostatic force is the sum of local force and global force. The total forces of the electrostatic comb can be described as

$$F_{Total} = F_x^{Global} + F_x^{Local} \quad (6.8)$$

where the local and global field energy formula, the local and global force can be defined as

$$F_x^{Local} \approx -\frac{\partial U_{filed}^{Local}}{\partial(2x_0)} = \frac{VQ}{2} \quad (6.9)$$

$$F_x^{Global} \approx -\frac{\partial U_{filed}^{Global}}{\partial(2x_0)} = 4(c + g) \frac{\epsilon_0 V^2}{2\pi(-x_0)} \left[ 1 - \frac{x_0}{2l-x_0} \right] \cong 4(c + g) \frac{\epsilon_0 V^2}{2\pi(-x_0)} \quad (6.10)$$

The above these equations are developed for the electrostatic forces operating in a micromechanical comb actuator, it is also a fit model for the calculation of force produced by the electrostatic comb. Based on this, the revised equation for the electrostatic comb is derived as follows

$$F_{AARL\_comb\_fin} = 2N\epsilon V^2 \left[ 2.2464 - \frac{c+g}{\pi x_0} \right] \quad (6.11)$$

where N is the number of comb pairs and V is the applied voltage. When the engagement distance  $x_0$  is far greater than  $(c + g)$ , the force between the comb could be treated as a function of the comb fin pair numbers and the applied voltage. This characteristic makes it appropriate for the balance calibration in which the position of the fins only changes in a small range. Therefore, the equations derived from equation 6.11 have been widely applied to the electrostatic comb. The global force can be considered as the edge effect of the parallel plate capacitor. In a comb structure, the clearance between the adjacent fins is constant while the equivalent area of the fin changes

with the engagement changing. Therefore, the force is inversely proportional to the engagement. However, when the engagement increases, the distance between the fin and plate decreases and the edge effect contributes a lot to the overall output force. As a result, the output force changes abruptly and the empirical equation is not fit any more. In general, equation 6.11 could not be used directly for the force calculation of the electrostatic comb. In addition, the force can be determined by modeling in Comsol. Therefore, to determine the specific relations among the dimension of the comb, the applied voltage, engagement distance, and the output force, the pre-calibration of the AARL fins comb needs to be further conducted.

**6.2.2 Experiment setup**

The PCB electrostatic comb calibration system consists of a PCB electrostatic comb, a function generator, a high voltage power supply, a high voltage measurement probe and an oscilloscope. The high voltage pulse generator is presented in the figure 6.6

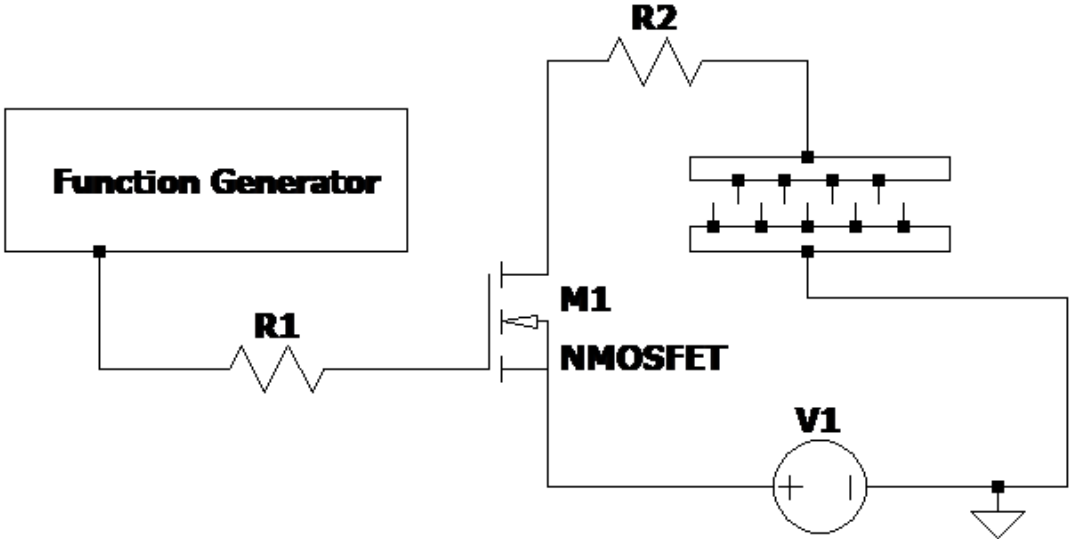


**Fig. 6.6** Simple AARL fin comb circuit

With the drive signals produced by the function generator, the NMOSFET are triggered. The width of the square pulse can be changed by adjusting the interval of the signal. The amplitude of the output voltage could be adjusted from 0 V to 2000 V, and the pulse width of the square

waveform could be from hundreds of nano-second to second. The comb can generate a steady state force when supplied with a DC voltage and an impulse output with the high voltage square waveform. A damping resistor ( $500\Omega$ , 5 W) is connected in series between the comb and voltage power source to reduce the voltage overshoot. The voltage probe is used to measure the output voltage of the power source and the pulse width of the square waveform in high voltage. To ensure the accuracy of the measurement, the probe and the oscilloscope is calibrated. Figure 6.7 represent the fins comb fabrication with different between two fins in row  $W$  at AARL lab.

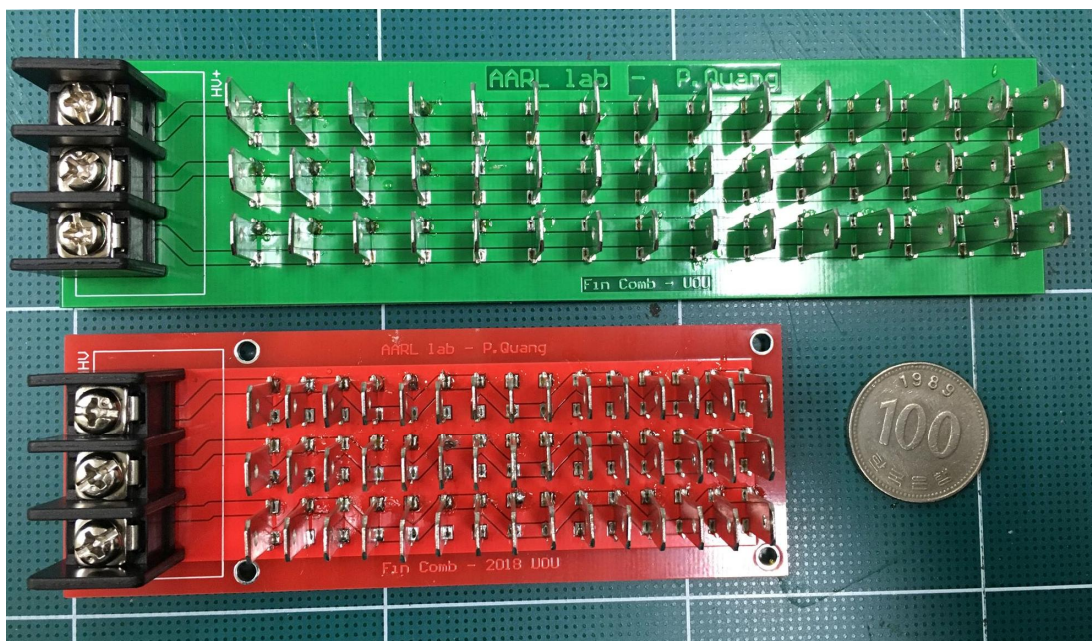


**Fig. 6.7** Fins comb fabrication with different  $W$  at AARL lab

The AARL fins comb system should be pre-calibrated using a weighing balance prior to the application presented in the previous section. The calibration process for the comb system is illustrated in Fig. 3. The movable plate was placed on the precision weighing balance (AND Co., Ltd., 0.1 mg), and the other plate was held by using an insulation support bar which was fixed on a displacement platform. The resolution of the balance is up to 0.1 mg which is equal to  $0.977 \mu\text{N}$  (the local gravitational acceleration is  $9.774 \text{ m/s}^2$ ). The micro-balance has been pre-calibrated with the calibration weight sets to ensure the accuracy. The displacement platform could move in the  $y$

direction which ensures the engagement distance adjustment with an accuracy of 0.01 mm. The applied voltage was provided by the high voltage power source with a range from 0 to 1500 V.

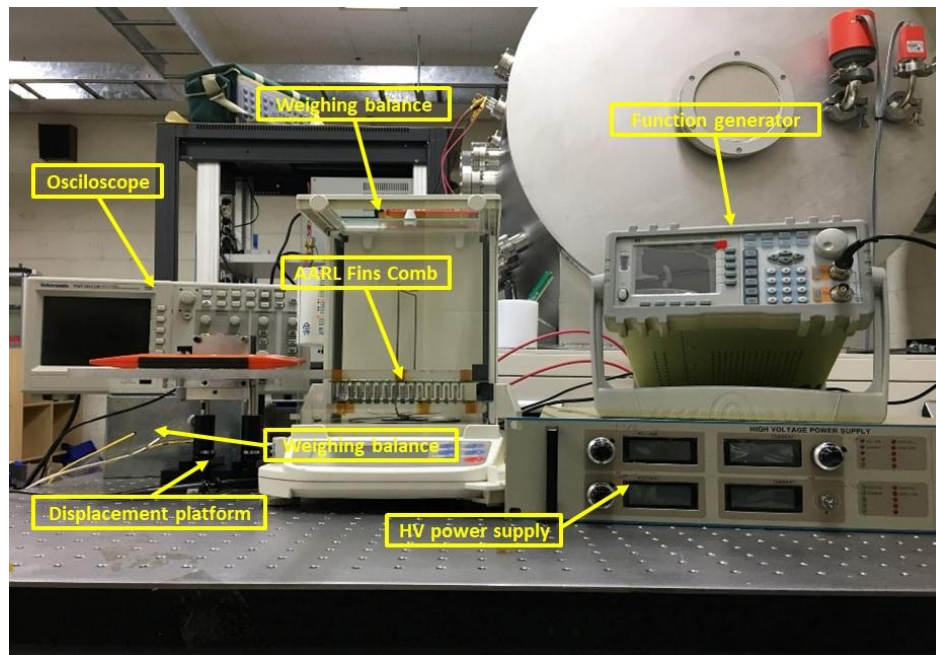


**Fig. 6.8** Experiment PCB comb calibration setting up at AARL lab

During the ESC calibration process, each point was repeated three times to minimize the random error. Before each measurement, the weighing balance needed to be reset to avoid the zero shift of the equipment. It took around 20 s for the balance to reach the final result, and the display should not change before the data are recorded. In addition, the calibration platform should be kept away from any vibration and air flow which would have influence on the measurement. The stray capacitance between the fins and any metal support could have an influence on the force measurement.

The force of the PCB comb at different voltages was measured with a weighing balance, as is shown in Figure 6.9. The high voltage plate of the PCB comb contains fifteen columns of fins and three rows and total  $15 * 3 = 45$  fins. The applied voltage was ranged from 200 V to 1300 V. The engagement distance of the comb was 10 mm. Force measurement for each engagement distance was repeated five times.

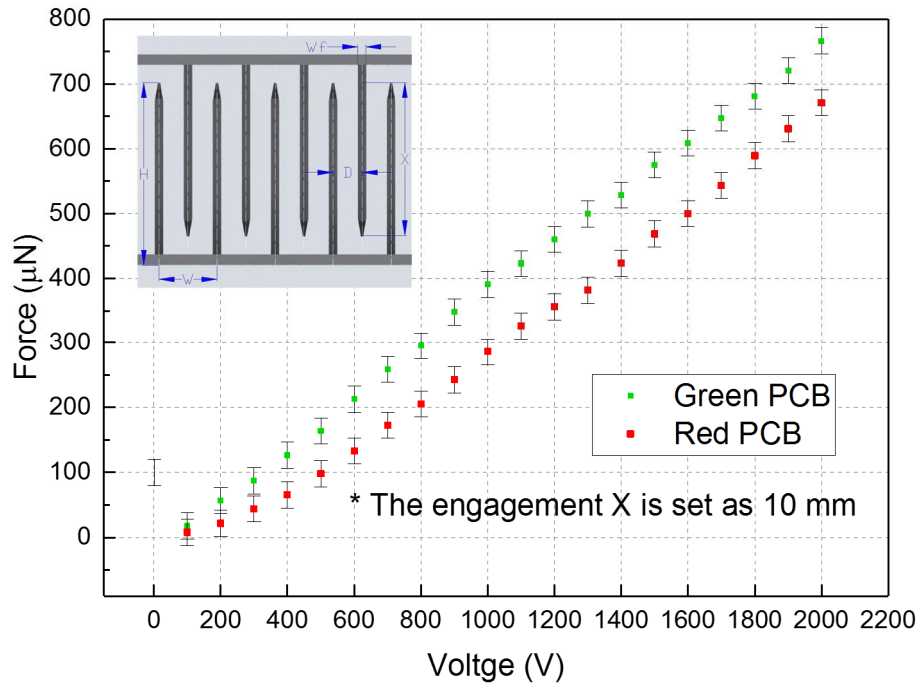


**Fig. 6.9** *Electrostatic force of the fins comb at different voltages*

### 6.3 Development of AARL electromagnetic system for AARL thrust stand

A new calibration technique based on an electromagnetic force will be introduced in this work. An electromagnetic force has been used as a part of feedback or a damper in several thrust stands that have been reported [51, 52] that measure steady force in the mN range. This technique was selected because of its linearity to coil current, noncontact between magnet and coil, and also its suitable force range. A permanent magnet structure with a uniform magnetic field was developed which is appropriate for the calibration of pulsed thrust measurements. The calibration force will stay the same in spite of the changing distance between coil and magnet during calibration. Magnet structure and coil are the two main parts of the AARL electromagnetic calibration. The force they produce is given by

$$F = BN\pi r I \quad (6.12)$$

where  $F$  is electromagnetic force,  $B$  is magnetic flux density at the coil location,  $N$  is the number of coil turns,  $r$  is the average radius, and  $I$  is coil current. For a coil design,  $N$  and  $r$  are constant. The magnet is installed on the thrust stand while the coil is fixed. Thus,  $B$  is required to

be uniform since the distance between magnet and coil will change during the operation of the EMCS. A magnet structure was designed to meet the main requirements of AARL thrust stand. The desired calibration force can be obtained by controlling the coil current. The coil can produce an electromagnetic force between 1–10 mN when the coil current is below 50 mA. The distance between the coil and magnet structure can be controlled by the X-Y translation stage. Figure 6.7 shows the magnet structure scale by the size of a Korean coin. Both left magnets and right magnets are divided into twelve groups distributed equally. Each group has three  $10 \times 6 \times 2$  mm NdFeB magnets with their magnetic field direction along the 2 mm side.

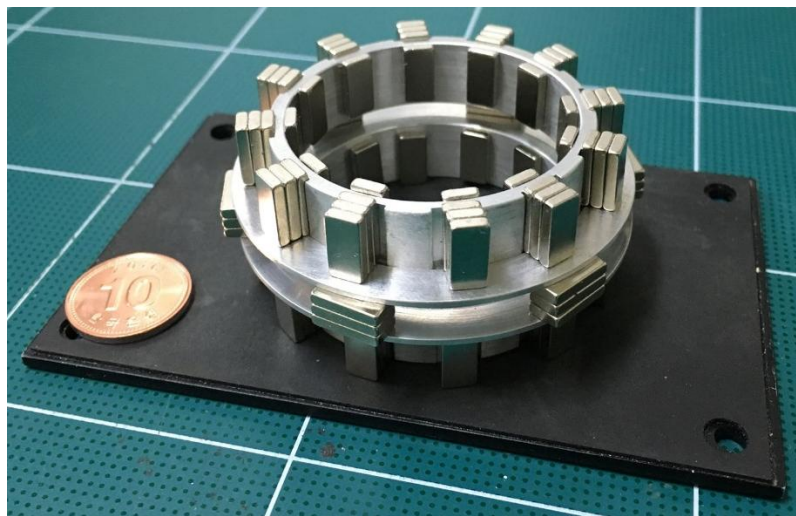


**Fig. 6.10** *The magnetic structure at AARL lab*

The magnetic field was examined using a digital mass balance whose resolution was 0.01 g. The relationship between  $F$  and  $I$  was determined as well. The magnet was placed on the digital mass balance, and Aluminium plate was placed between the magnet and the digital mass balance to avoid the magnet affecting the measurement. The coil was installed on a bracket on the magnet. The distance between coil and magnet could be changed by 1 mm as the screw went one circle, as shown in Fig. 6.10.

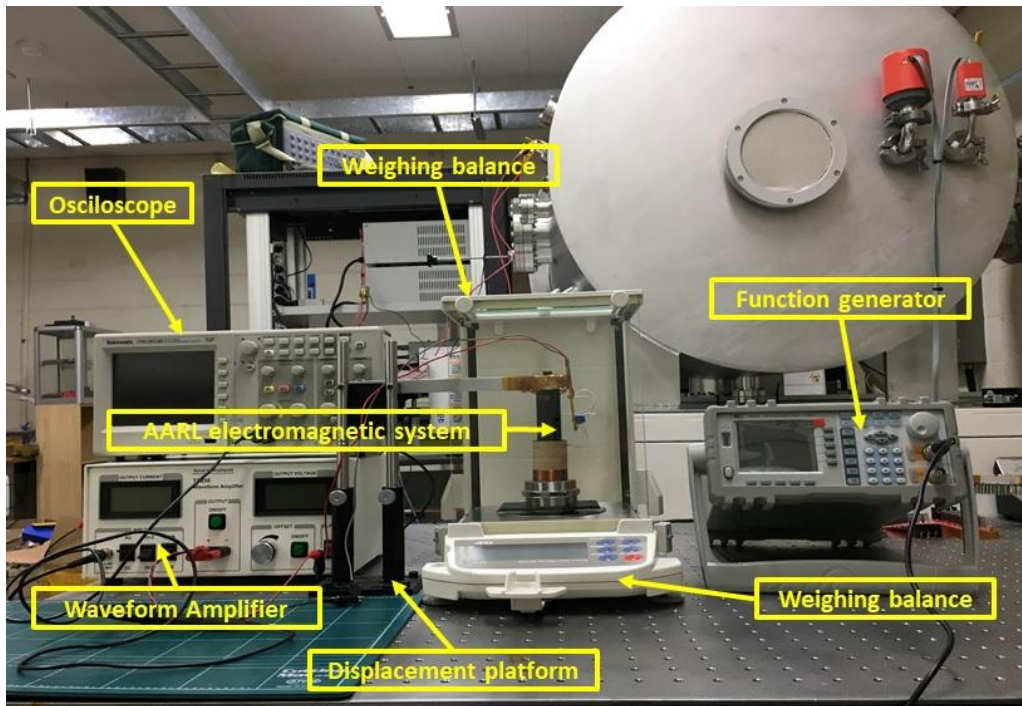


**Fig. 6.11** Experiment set up for electromagnetic calibration system at AARL lab

Tests were conducted with the distance between coil and magnet varied from 1 mm to 10 mm with an interval of 1 mm. The initial placement was defined where the coil's lower surface and magnet's upper surface were in the same plane. When the coil was moved down 2 mm, the distance between coil and magnet was 2 mm. By changing coil current, different electromagnetic forces were generated. The electromagnetic force was calculated by multiplying the effective mass reading by  $g=9.83\text{m/s}^2$ , the relationship between electromagnetic force and coil current for different distances is shown in figure 6.11.

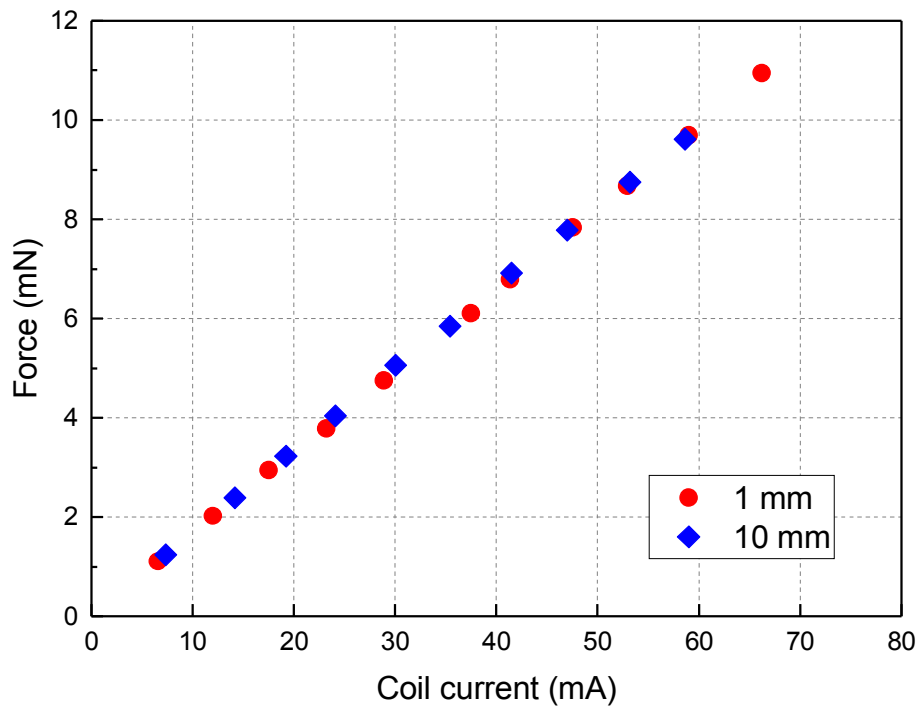


**Fig. 6.12** Force as a function of coil current for engaged distance from 1 to 10 mm

#### **6.4 A power supply of the retarding potential analyzer (RPA) probe design for iU-50 ion thruster**

The retarding potential analyzer (RPA), also known as retarding field energy analyzer (RFEA), is used to measure the ion energy distribution function (IEDF) in a plasma. A Langmuir probe can not easily provide information about the ion distribution function. At a positive potential, when repelling ions, the Langmuir probe is drawing a high electron current which hides the variations in the ion current. The RPA avoids this problem by blocking the electrons with a negatively biased grid at the entrance of the probe. A grid inside the probe is biased from a slightly negative value to a positive value where no more ions arrive at the collector. By measuring the collector current as a function of the grid bias and calculating the derivative of this function the IEDF can be obtained. A schematic of the popular RPA is shown in figure 6.12.

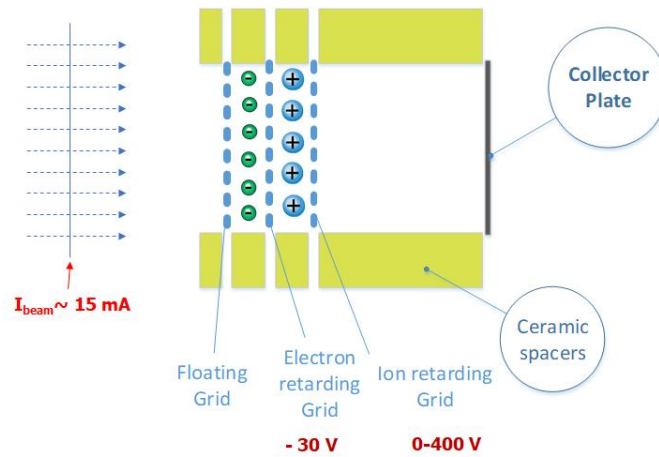


**Fig. 6.13** A schematic of the popular RPA

The ion entering the RPA will pass through the 3 grids inside the RPA. Between the 2<sup>nd</sup> grid which biased at -30V and the 3<sup>rd</sup> grid which ranges from 0V to 400V scanning voltage, there is an electric field that decreases the ions. The velocity of the ions will decrease to the diffusion velocity when the potential on the 3<sup>rd</sup> grid reaches 400V and the ions reach the grid surface. The plasma diffusion velocity is usually smaller than 0.05 eV ~ 270 m/s. To do that, the power supply for 3<sup>rd</sup> grid was developed at AARL. The most advantage of AARL power supply is cheap and convenience in use. The simple schematic of the 3<sup>rd</sup> grid power supply is presented in the figure 6.13.

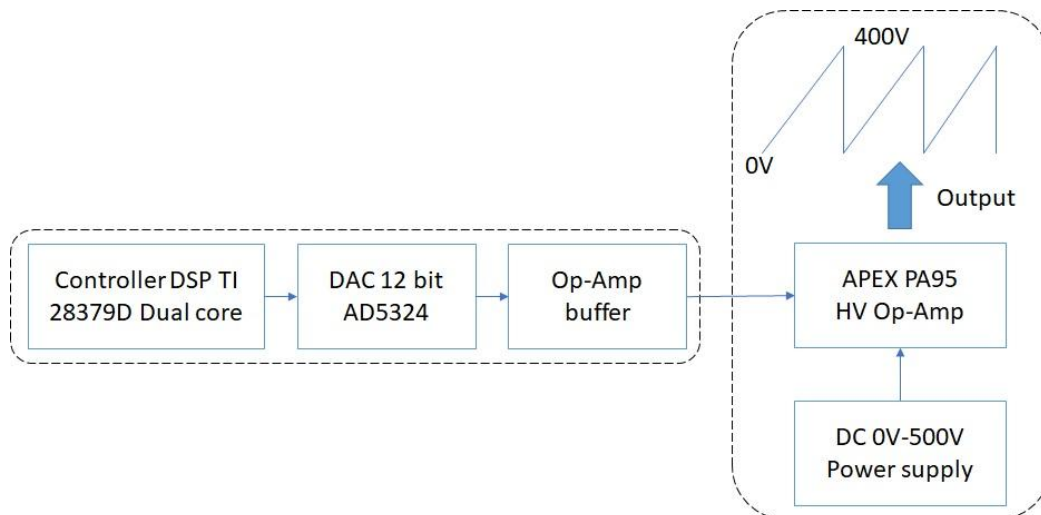


**Fig. 6.14** A schematic of 3<sup>rd</sup> grid power supply

The target is sawtooth waveform from 0V to 400V. Therefore, the APEX PA95 is suitable for this purpose. After determining all electric component specification, we proceeded to design the PCB circuit using Altium software. The figure 6.14 shows the PCB design for 3<sup>rd</sup> grid power supply.

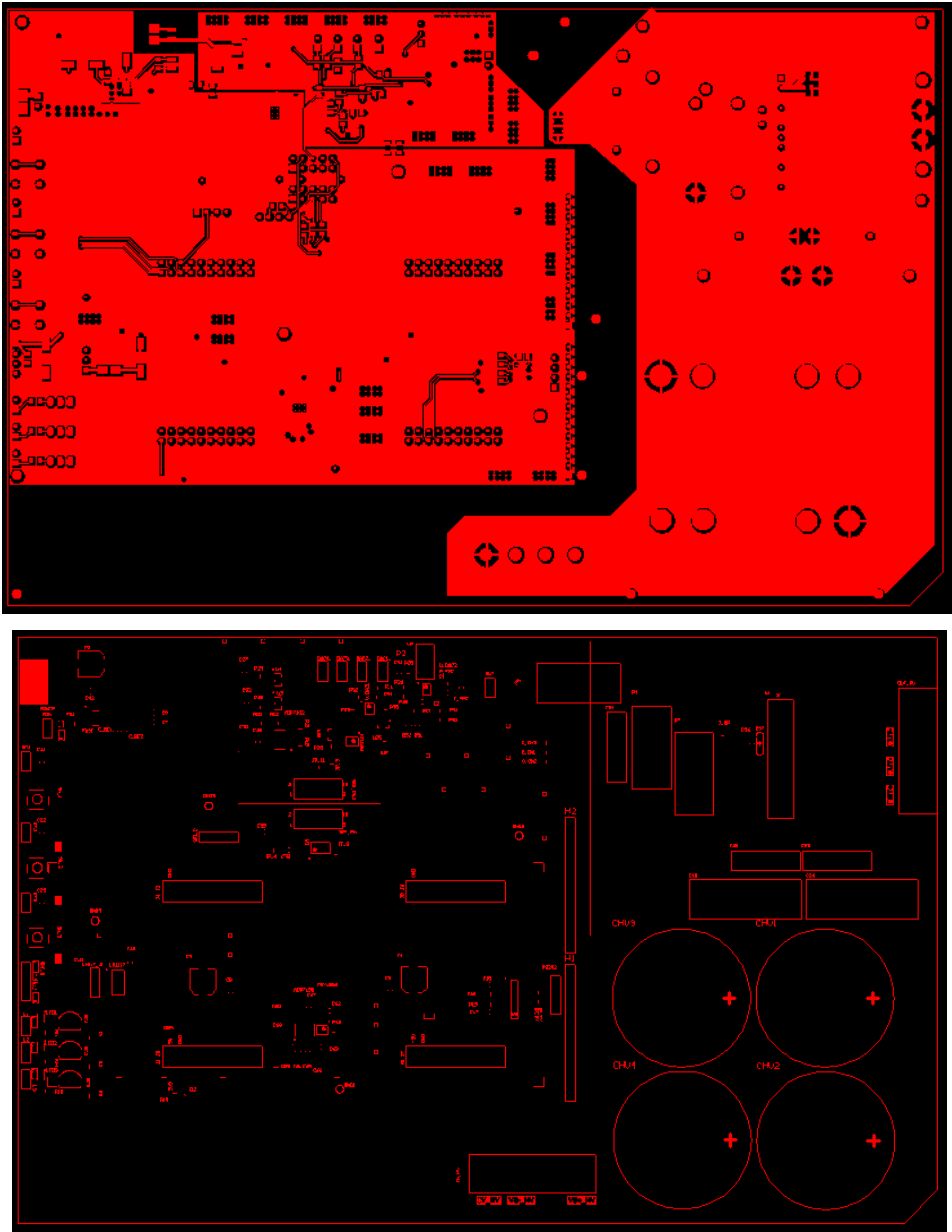


**Fig. 6.15** *The schematic of the PCB*

The 3D of the 3<sup>rd</sup> grid power supply is shown in the figure 6.15

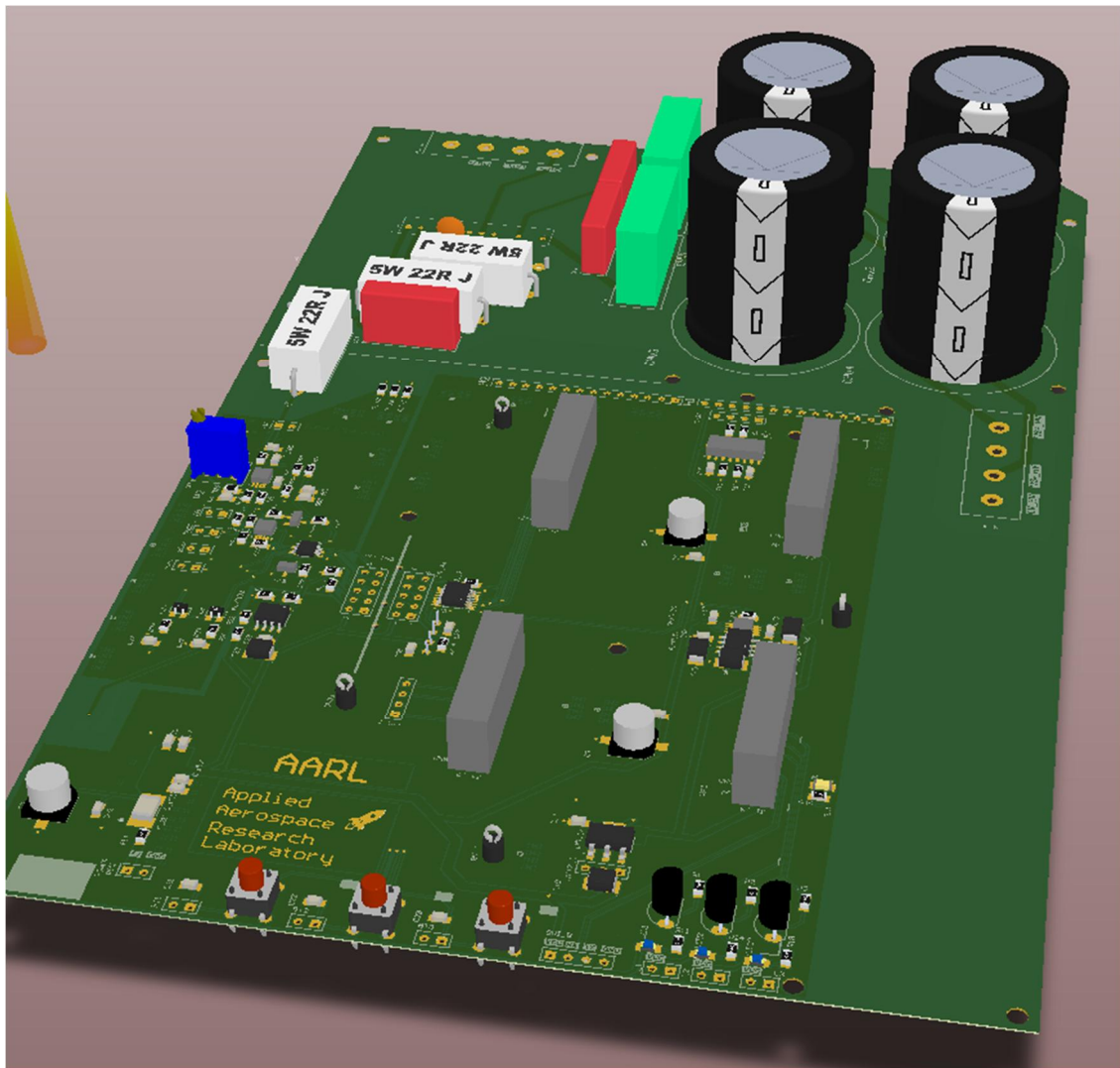


**Fig. 6.16** *3<sup>rd</sup> grid power supply PCB at AARL lab*

Before using 3<sup>rd</sup> grid power supply for iU-50 ion thruster measurement. A test is conducted on the power supply without applying to RPA probe. The experiment set up is shown in Figure 6.16.

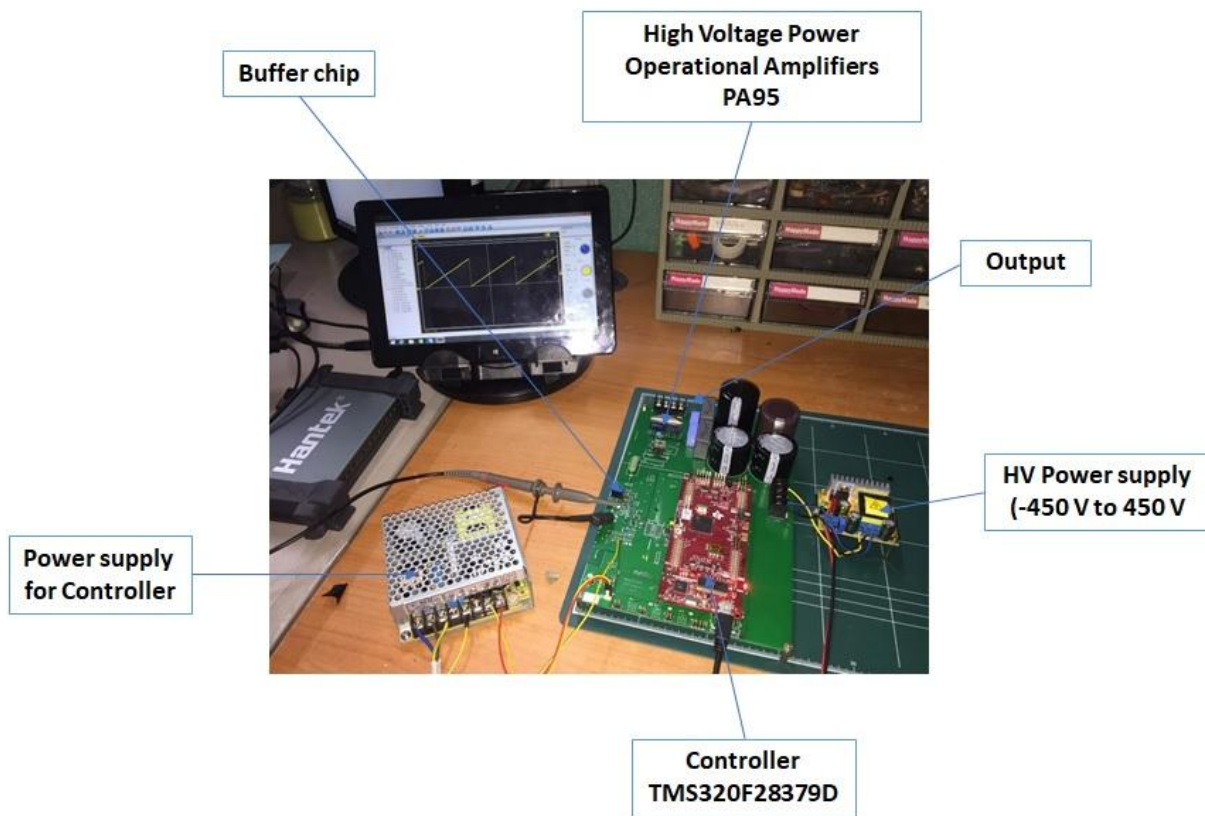


**Fig. 6.17** *The experiment set up for 3<sup>rd</sup> grid power supply inhouse*

Figure 6.17 presents the result of the sawtooth waveform measuring from output of the 3<sup>rd</sup> grid power supply at different frequencies and voltage amplifier.

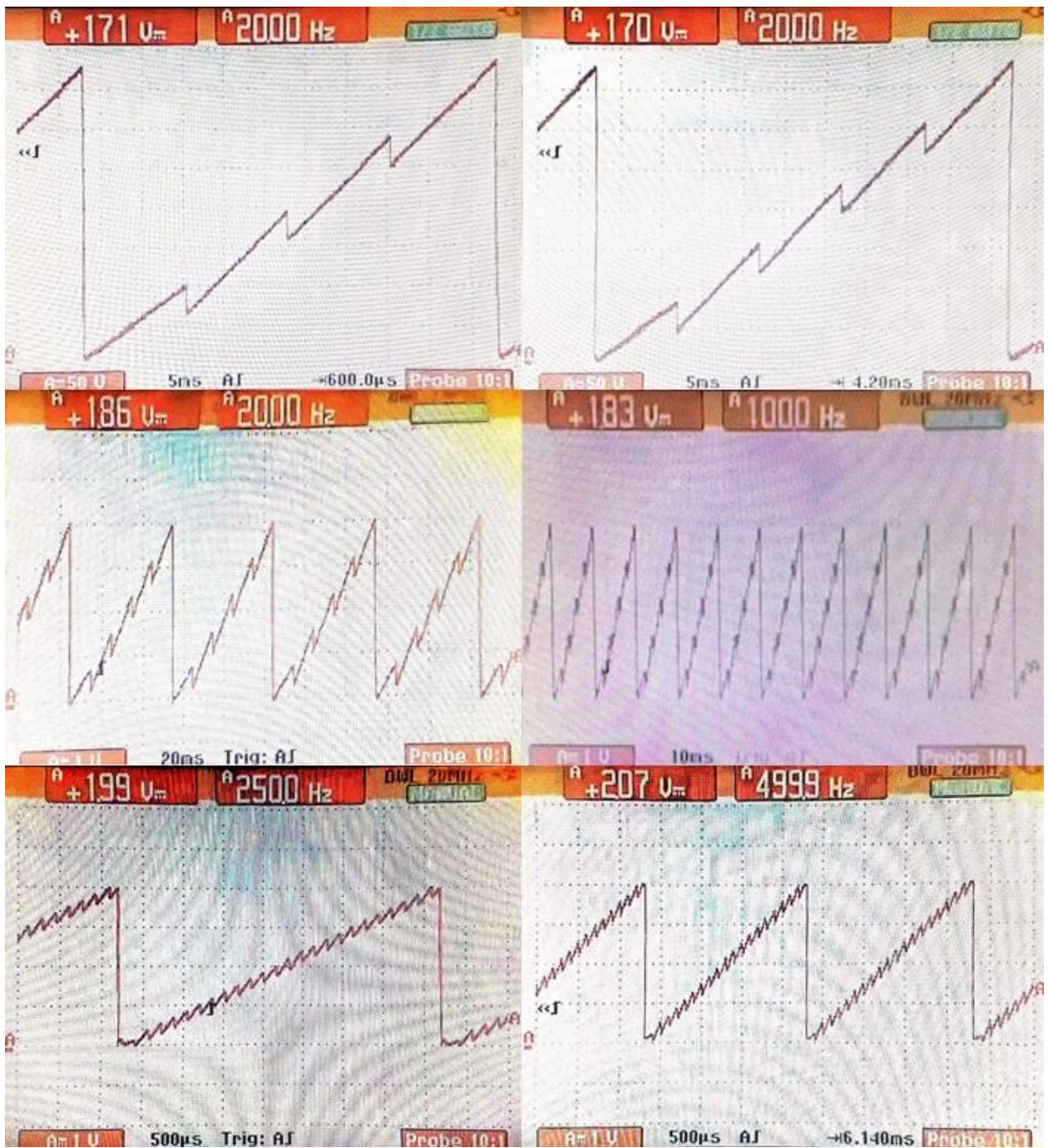


Fig. 6.18 Experiment result from Oscilloscope (Fluke 196C 100MHz)

## 6.5 Chapter summary

In this chapter, the plume diagnostic instruments were developed in order to understand the mechanism of generating thrust. The instruments include a retarding potential analyzer (RPA) design that is capable of measuring high level energy and high-density plasma beams. To overcome the limitations of existing RPAs measurement systems, the high voltage power supply with scan voltage from 0 V to 400 V was developed at our AARL lab. The RPA design parameters were determined by analyzing the electron density and temperature, the sheath thickness, and the ion density in beam based on the Faraday probe and Langmuir probe measurements. We propose the novel calibration technique, and characterization of a thrust stand capable of micro Newton resolution. In particular, a permanent magnet structure was designed to produce a uniform magnetic field, and a multiturn coil was made to produce a calibration force less than  $\sim 5$  mN. The electromagnetic calibration force for iU-50 thrust measurements was linear to the coil current and changed less than 2.5% when the distance between the coil and magnet changed  $\sim 6$  mm.

## Chapter 7. Conclusion and Future Work

This chapter draws main conclusions based on the work presented in this thesis. In particular, a summary of the thesis is provided together with a discussion on the key findings, the significance of the work, the future work and outlook.

### 7.1 Conclusions

The design and implementation of a radio frequency discharge ion thruster were reported in this thesis. A discussion was provided on the fundamental theory of electric thrusters in order to determine the feasibility of electromagnetic thrusters. The different methods of ionizing the propellant was presented, whereafter the method of RF ionization was implemented. The electromagnetic fields used for the ionization of the propellant eliminated the lifespan issues associated with electrode-based electric thrusters. It's suggested to use 0-D analytical discharge chamber for iU-50 ion thruster to optimize the chamber design as well as output critical information for more complicated model like 2-D or 3-D.

This study has further improved the analytical models previously reported for RF gridded-ion thruster to provide better predictions of performance that might be useful in the design phase. Additional features we considered were the secondary electrons emission, the doubly-charged xenon ions, the variable Clausing factor obtained by the Monte Carlo calculation, and the ion confinement factor generated by the electromagnetic field in the discharge chamber. The ion confinement factor had the greatest effect on the calculation. The calculation results obtained from our improved analytical model were in good agreement with the experimental results for both large and small RF ion thrusters for various beam currents.

The design and characterization of the torsional balance capable of nano-Newton level resolution were presented. This work focused on the development of a noncontact electromagnetic

calibration technique which can be used in iU-50 thrust measurements. A permanent magnet structure was built to produce a relatively uniform magnetic field. Tests on a digital mass balance showed that electromagnetic force changed less than 2.5% while the distance between coil and magnet changing from 1 to 10 mm. Experimental data showed that there exists good linearity between the electromagnetic force and coil current. By increasing number of turns and enlarging the diameter of the wire, the slope of the F–I relationship will become larger. Hence, it would be possible to measure steady forces less than 150 mN, using an electromagnetic force as a counteracting force. Thus, calibration can be taken using a digital mass balance, which is an improvement over the standard method.

The novel electrostatic comb has been presented. It is able to produce repeatable and precise force for the torsional balance calibration. With the printed circuit board technique, it is convenient to obtain a calibrator with great performance. By comparing the influence of the conductive plate and fin length, the PCB base plate without the copper layer and the longer fin was adopted to acquire a better consistency over the engagement. The PCB comb is capable of generating steady force and equivalent impulse with a high voltage square wave generator. The force ranges from  $\mu\text{N}$  with the applying voltage 1500 V.

The Scanning power supply of the RPA probe was developed at AARL lab. The result shows that it can meet a requirement for ion energy measurement.

## **7.2 Future works**

The further works may need to include the following two aspects:

- Developing hybrid model of RF gridded ion thruster.
- Testing iU-50 thruster comprehensively in the vacuum chamber at AARL lab.

*This work was supported by the 2017 Research fund of University of Ulsan.*

## REFERENCES

- [1] Choueiri, E. Y., A Critical History of Electric Propulsion: The First 50 Years (1906-1956), *Journal of Propulsion and Power*, Vol. 20, No. 2, 2004, pp. 193-203..
- [2] Mazouffre, S., Electric propulsion for satellites and spacecraft: established technologies and novel approaches. *Plasma Sources Science and Technology*, 25(3), 2016, p.033002.
- [3] Goebel, D. M. and Katz, I., *Fundamentals of electric propulsion ion and Hall thrusters*, Wiley, Hoboken, NJ, 2008.
- [4] Daniłko, Dariusz. Overview of electric propulsion. *Photonics Applications in Astronomy, Communications, Industry, and High-Energy Physics Experiments 2014* (2014).
- [5] Nickolay N. Antropov, Garry A. Popov and Michael N. Kazeev. Ablative Pulsed Plasma Thrusters R&D in Russia since the Beginning of the 90s, *Proceedings of the 33rd International Electric Propulsion Conference (IEPC)*, Washington D.C., USA, 2013, IEPC-2013-68.
- [6] R. G. Jahn and E.Y. Choueiri, *Electric Propulsion*, *Encyclopedia of Physical Science and Technology*, 3rd Ed., Vol. 5, New York, Academic Press, 2002.
- [7] Roger M. Myers, *Electromagnetic Propulsion for Spacecraft*. Presented in the 1993 Aerospace Design Conference, Irvine, CA, USA, 1993, AIAA-93-1086.
- [8] Roger M. Myers, Steven R. Oelson, Melissa McGuire, Nicole J. Meckel and Joseph R. Cassady, *Pulsed Plasma Thruster Technology for Small Satellite Missions*. Presented at the 9th AIAA/Utah State University Conference on Small Satellites, 1995.
- [9] Michael, J. Mitrich. *Resistojet Propulsion for Large Spacecraft Systems*, Presented in the 16th International Electric Propulsion Conference (IEPC), New Orleans, LA, Russia, 1982.
- [10] Martinez-Sanchez, M. and Pollard, J. E., "Spacecraft Electric Propulsion-An Overview", *Journal of Propulsion and Power*, Vol. 14, No. 5, 1998, pp. 688-699.

- [11] R. Rhoads Stephenson. Electric Propulsion Development and Application in the United States, Proceedings of the 24th International Electric Propulsion Conference (IEPC), Moscow, Russia, 1995, IEPC-95-01.
- [12] D. M. Goebel and I. Katz. Fundamentals of Electric Propulsion. John Wiley & Sons, Hoboken, Nj, 2008.
- [13] J. R. Wertz and W. J. Larson, eds., Space Mission Analysis and Design, Torrance, California: Microcosm Press, 1999.
- [14] M. M. Turner and M. A. Lieberman. Plasma Sources Sci. Technol., 8:313, 1999.
- [15] Killinger, R., Leiter, H., and Kukies, R., RITA Ion Propulsion Systems for Commercial and Scientific Applications, 43rd AIAA/ASME/SAE/ASEE Joint Propulsion Conference & Exhibit, AIAA Paper 2007-5200, July 2007.
- [16] D. M. Goebel, Fellow, IEEE Trans. Plasma Sci. 36, 2111 (2008).
- [17] M. Dobkevicius and D. Feili, J. Propul. Power. 33, 939 (2017).
- [18] P. Chabert, J. Arancibia Monreal, J. Bredin, L. Popelier, and A. Aanesland, Phys. Plasma. 19, 073512 (2012).
- [19] S. V. Kanev, S. A. Khartov, V. V. Nigmatzyanov, Proc. Engineering. 185, 31 (2017).
- [20] T. Arzt, Numerical simulation of the RF ion source RIG10, J. Phys D: Appl. Phys. 21, p.278, 1988.
- [21] Valerie F. Mistoco, Sven G. Bilén, Numerical Modeling of a Miniature Radio-Frequency Ion Thruster, 44<sup>th</sup> Joint Propulsion Conference, AIAA 2008-5194, Hartford, CT, July 21-33, 2008.
- [22] Micheal Meng-Tsuan Tsay, Two-Dimensional Numerical Modeling of Radio-Frequency Ion Engine Discharge”, Ph. D. Thesis, Massachusetts Institue of Technology, 2010.
- [23] Seiji Samukawa et al, The 2012 Plasma Roadmap, J. Phys. D: Appl. Phys, Vol 45, No. 25, 2012.

- [24] H. J. Leiter, R. Killinger, H. Bassner, J. Miller, R. Kulies, and T. Froehlich, Evaluation of the performance of the advanced 200 mN radio frequency ion thruster RIT\_XT, presented at the 38<sup>th</sup> Joint Propulsion Conf., Indianapolis, INm Jul. 7-10, 2002, Paper No AIAA-2002-3836.
- [25] P. Clausing, *J. Vac. Sci. Technol.* 8, 636 (1971).
- [26] T. Kalvas, R. F. Welton, O. Tarvainen, B. X. Han, and M. P. Stockli, *Rev. Sci. Instrum.* 81, 02B703 (2010).
- [27] J. M. File, M. Martinez-Sanchez, and J. Szabo, *Proc. 33rd Joint Propulsion Conf.* 1997, p. 3052.
- [28] J. P. Bugeat and C. Koppel, *Proc. 24th IEPC*, 1995, p. 286.
- [29] N. Gascon, M. Dudeck, and S. Barral, *Phys. Plasma.* 10, 4123 (2003).
- [30] Child, C.: Discharge from hot cathode. *Physical Review*, vol. volume 32, p. 492, 1911.
- [31] Langmuir, I.: The effect of space charge and residual gases on thermionic currents in high vacuum. *Physical Review*, vol. volume 2, p. 450, 1913.
- [32] T. Kalvas, et. al., IBSIMU: A three-dimensional simulation software for charged particle optics, *Rev. Sci. Instrum.* 81, 02B703, (2010)
- [33] Stepan V. Kanev, Sergey A. Khartov, Vladislav V. Nigmatzyanov, Analytical model of radio frequency ion thruster, *Procedia Engineering* 185 (2017) 31-38.
- [34] Bassner, H., Bond, A. R., Thompson, K. V., & Groh, K., The ESA XX ion thruster, Second European Spacecraft Propulsion Conference, Proceedings of the conference held 27-29 May 1997 in Noordwijk, the Netherlands. Edited by Michael Perry. ESA SP-398. Paris: European Space Agency, 1997., p.251
- [35] D. Bohm, *The Characteristics of Electric Discharges in Magnetic Fields*, A. Guthrie and R. Wakerling, Eds. New York: McGraw-Hill, 1949, pp. 1-763.

- [36] Rajappa, S., Masone, C., Bulthoff, H., H., and Stegagno, P., Adaptive Super Twisting Controller for a Quadrotor UAV, 2016 IEEE International Conference on Robotics and Automation, pp. 2971-2977, 2016.
- [37] J. D. Huba, NRL Plasma Formulary. Washington, DC: Naval Res. Lab., 2007. NRL/PU/6790-07-500.
- [38] Y. Raitses, A. Smirnov, D. Staack, and N. J. Fisch, Phys. Plasma. 13, 014502 (2006).
- [39] J. M. File, M. Martinez-Sanchez, and J. Szabo, Proc. 33rd Joint Propulsion Conf. 1997, p. 3052.
- [40] J. P. Bugeat and C. Koppel, Proc. 24th IEPC, 1995, p. 286.
- [41] H.W. Loeb, J. Freisinger, K.H. Groh, and A. Scharmann, State-of-the-Art of the RIT Ion Thrusters and Their Spin-Offs, IAF-88-258, Bangalore 1988.
- [42] H. W. Loeb, K. H. Schartner, St. Weis, D. Feili, and B. K. Meyer, Development of RIT-Microthrusters, 55<sup>th</sup> International Astronautical Congress 2004, Vancouver, Canada.
- [43] Fraundorfer, H. J. Leiter, R. Killinger, H. Bassner, J. Müller, R. Kulies, T. Fröhlich, Development and Performance of the Advanced Radio Frequency Ion Thruster RIT-XT, 28th International Electric Propulsion Conference, Toulouse, France, 2003.
- [44] R. E. Wirz, Discharge Plasma Processes of Ring-Cusp Ion Thrusters, PhD Thesis, California Institute of Technology, Pasadena, California, 2005.
- [45] Mingu, H. W. Loeb, D. Feili, G. A. Popov, V. A. Obukhov, V. V. Balashov, A. I. Mogulkin, V. M. Murashko, A. N. Nesterenko, S. Khartov, Design of High-Power High-Specific Impulse RF-Ion Thruster, 32nd International Electric Propulsion Conference, Wiesbaden, Germany, 2011, IEPC2011-290
- [46] R. B. Piejak, V. A. Godyak and B. M. Alexandrovich. Plasma Sources Sci. Technol., 1:179, 1992..

- [47] S. Xue, P. Proulx, and M.I. Boulos, "Extended-field electromagnetic model for inductively coupled plasma," *J. Phys. D.* 34, 1897, 2001.
- [48] K. H. Cheah, K. Low, T. Quang-Vinh, and Z. Lau, *IEEE Trans. Instrum. Meas.* 64, 3467 (2015).
- [49] W. A. Johnson and L. K. Warne, *J. Microelectromech. Syst.* 4, 49 (1995).
- [50] W. C. Tang, M. G. Lim, and R. T. Howe, *J. Microelectromech. Syst.* 1(4), 170 (1992)
- [51] H. Koizumi, K. Komurasaki, and Y. Arakawa, *Rev. Sci. Instrum.* 75(10), 3185 (2004).
- [52] K. G. Xu and M. L. R. Walker, *Rev. Sci. Instrum.* 80(5), 055103 (2009).